UNIVERSIDADE DE SANTIAGO DE COMPOSTELA

Ab initio study of low-dimensional metallic systems

by

Jorge Botana Alcalde

A thesis submitted in partial fulfillment for the
degree of Doctor of Philosophy

in the
Facultade de Física
Departamento de Física Aplicada

19^{th} September, 2011

Declaration of the Advisor

We, DANIEL BALDOMIR FERNÁNDEZ, professor of the Applied Physics Department at the University of Santiago de Compostela, and MANUEL PEREIRO LÓPEZ, doctor of Philosophy in Physics by the University of Santiago de Compostela

DECLARE THAT:

- This thesis titled '*Ab initio study of low-dimensional metallic systems*' and the work presented in it was carried out by JORGE BOTANA ALCALDE under our advising.
- The thesis is submitted in partial fulfilment for the degree of Doctor of Philosophy in the Applied Physics Department at the University of Santiago de Compostela.

Signed:

Date: 19^{th} September, 2011

Declaration of Authorship

I, JORGE BOTANA ALCALDE, declare that this thesis titled '*Ab initio study of low-dimensional metallic systems*' and the work presented in it are my own. I confirm that:

- This work was done wholly or mainly while in candidature for a research degree at this University.
- Where any part of this thesis has previously been submitted for a degree or any other qualification at this University or any other institution, this has been clearly stated.
- Where I have consulted the published work of others, this is always clearly attributed.
- Where I have quoted from the work of others, the source is always given. With the exception of such quotations, this thesis is entirely my own work.
- I have acknowledged all main sources of help.
- Where the thesis is based on work done by myself jointly with others, I have made clear exactly what was done by others and what I have contributed myself.

Signed:

Date: 19^{th} September, 2011

"What is real? How do you define real? If you're talking about what you can feel, what you can smell, what you can taste and see, then real is simply electrical signals interpreted by your brain."

Morpheus

UNIVERSIDADE DE SANTIAGO DE COMPOSTELA

Abstract

Facultade de Física
Departamento de Física Aplicada

Doctor of Philosophy

by Jorge Botana Alcalde

We have studied several low-dimensionality systems using *ab initio* techniques, based on the DFT approximation; said techniques have become in the recent times one primary path of theoretical research in solid state physics. We have first analysed ultrathin trilayers of $Fe_n/Cr_3/Fe_n$ ($n = 1 \rightarrow 6$), searching for patterns in the properties of the trilayer as the thickness of the Fe layers grows. Such trilayers have been fundamental in the discovery of phenomena like GMR and are a key element of the spintronic technology. What we found is that the central layer of the Cr atoms absorb electrons from the Fe ones. This electron excess acts as a perturbation that spreads a Friedel-like oscillation in the excess-defect of charge of the rest of the trilayer. From the parametrization of this oscillation, extending the concept of electron effective mass to 2D systems, we can infer some transport properties of the system.

The second group of systems studied were the gold clusters. We calculated the properties of gold clusters in a spread of situations. The interest on gold clusters derived from their promise to show a large magnetic moment per atom (in comparison with bulk), which would enhance their biomedical properties, adding to their reactivity in biological medium as a catalyst. Regarding 8-atom clusters, we showed that the reason for them to remain 2D, unlike Ag and Cu, is not a lower kinetic energy due to $d-d$ band interaction; instead the exchange-correlation component unbalances the energy to favour 2D clusters, because the structure distortions that 3D clusters suffer (respect to the Ag and Cu structure counterparts) affects the electron localization. Furthermore, the 8-atom gold structures show a dependence with their magnetic state that makes them potential candidates for magnetostriction. Regarding the interaction between Au clusters and O_2 molecules, we searched the lowest energy configurations for $Au_{n,n=3\rightarrow 7}$ clusters and found that for the clusters Au_2 and Au_4, the O_2 forms an in-plane bound state, without distortion for the Au structure, whereas for the Au_3, Au_5, Au_7, the O_2 form an off-plane unbound state that slightly curves the planar cluster structure around the O_2, which is something to be considered carefully as Au clusters catalytic properties are highly dependant on their chirality.

We have also studied a transition metal alloy cluster, the Bi_4Mn, in relation to a problem of disagreement between the experimentally measured value of its magnetic moment and the *ab initio* calculated one. Through extensive exploration of all theoretical possibilities, we found no scenario where the lowest energy structure of the Bi_4Mn would have a calculated magnetic moment that would fit with the experiment. Instead we found some high-energy isomers that could fit. As these isomers are very similar in structure to the Bi_3Mn ones, we speculate that they could be the ones actually measured in the experiment.

The last part of the work consists in a non-*ab initio* calculation of the optical properties of gold nanoparticles, made up with thousands of atoms (which makes the use of ab initio techniques impractical). We used the discrete dipole approximation to calculate the spectra of said nanoparticles imbibed in aqueous medium, to help characterize an experimental sample.

Contents

Abbreviations

2D	**2 D**imension(-s/-al)
3D	**3 D**imension(-s/-al)
AE	**A**ll-**E**lectron
AF	**A**nti**F**erromagnetic
AP	**A**nti**P**arallel
bcc	**b**ody-**c**entered **c**ubic
BFGS	**B**royden-**F**letcher-**G**oldfard-**S**hanno
deMon	**de**nsity of **Mon**tréal
DDA	**D**iscrete **D**ipole **A**pproximation
DFT	**D**ensity **F**unctional **T**heory
DOS	**D**ensity **o**f **S**tates
ELF	**E**lectron **L**ocalization **F**unction
FLT	**F**erromagnetic **L**ayer **T**hickness
FM	**F**erro**M**agnetic
GGA	**G**eneralized **G**radient **A**pproximation
GS	**G**round **S**tate
GMR	**G**iant **M**agneto**R**esistance
GTO	**G**aussian-**T**ype **O**rbitals
HLg	**H**OMO-**L**UMO gaps
HOMO	**H**ighest **O**ccupied **M**olecular **O**rbital
KS	**K**ohn-**S**ham
KSDFM	**K**ohn-**S**ham-**D**ensity-**F**unctional **M**ethodology
LCGTO	**L**inear **C**ombination of **G**aussian-**T**ype **O**rbitals

LSDA	**L**ocal-**S**pin **D**ensity **A**pproximation
LUMO	**L**owest **U**noccupied **M**olecular **O**rbital
MCP	**M**odel **C**ore **P**otential
MM	**M**agnetic **M**oment
MMA	**M**agnetic **M**oment per **A**tom
MP	**M**odel **P**otential
MPA	**M**ulliken **P**opulation **A**nalysis
MR	**M**agneto**R**esistance
RKKY	**R**uderman-**K**ittel-**K**asuya-**Y**osida
SCF	**S**elf-**C**onsistent **F**ield
SDW	**S**pin **D**ensity-**W**ave
TDDFT	**T**ime-**D**ependent **D**ensity **F**unctional **T**heory
TM	**T**ransition-**M**etal
XC	e**X**change-**C**orrelation

Symbols

Roman symbols		Greek symbols	
m_σ^*	Effective electron mass	σ	Conductivity
m_e	Free electron mass	$\rho(\mathbf{r}, \omega)$	Electronic density
E_{xc}	Exchange-Correlation Energy	$\Delta\varepsilon$	HOMO-LUMO gap
E_C	Correlation Energy	χ_m	Magnetic susceptibility
E_h	hartree Energy	μ_B	Bohr Magneton
E_F	Fermi level	μ_T	Total Magnetic Moment
k_F	Fermi wave vector		
H	Magnetic field		
$\tilde{E}_{SCF}$	SCF energy		
$S(\varepsilon)$	Strength function		
$v_{xc}(\mathbf{r}, t)$	XC potential		
V_{ne}	nuclei-electron interaction		
V_{ee}	electron-electron interaction		
Z	Atomic Number		

Aos meus pais, por terme apoiado e aturado as neuras todo este tempo, aos que quero moito, anque non llelo diga coa frecuencia que debera.

A Tina, por emocionarse co meu traballo e querer que lle falase del, pola amizade e por estar sempre aí.

A Mercedes, Ana, Natalia e Miguel, pola súa amizade e por ser a millor xente coa que se pode estar.

Aos meus directores de tese, Daniel e Manuel, por ensinarme todo o que sei e por desafiarme e facerme buscar a excelencia.

A Víctor, Manuel, David, Alberto, Antía e Iván, por proveer un incrible ambiente de traballo, e pola súa amizade.

A ...

1 Introduction

> *Which brings us at last to the moment of* ***truth****, wherein the fundamental flaw is ultimately expressed, and the anomaly revealed as both* ***beginning****... and end.*
>
> *[The Architect]*

1.1 Motivation

The purpose of Physics, the purpose of Science in general, is to acquire knowledge on how the universe works, to extract the underlying principles that govern the behaviour of matter and energy. In a sense, this is not purely a human endeavour: every living species needs to know their environment. They need a model of the universe, or at least of "their universe", to improve their chances of survival; understanding a model as a simplified description of reality. Obviously these models need not to be neither conscious, nor very precise.

The only parameters that limit the complexity and depth of a certain modelization of the reality is the computing power and the memory storage at our disposal, whether it is simply a biological brain, a pen and a piece of paper, or a supercomputer.

Nowadays, our computing machines are so powerful that we can set them to calculate our most complex models: models that are not a simplified representation of reality, but the expression of the equations that describe the interactions of the fundamental particles, and build upon them to calculate the behaviour of larger systems. This is what is called calculating from first principles, or *ab initio*.

Even then, our computing resources are eventually limited. If we wish to study the nature from first principles, we need to chose carefully our battles. At the

atomic scale, matter appears to interact solely through the electromagnetic force. Consequently, to work out the physical observable in such systems we have to solve the Schrödinger equation. At this scale, the only charged particles we care about are the nuclei and the electrons. In comparison to the velocity of the electrons, the nuclei can be considered static because of their much larger mass, and they can be decoupled from the electrons within the equation (this is called the Born-Oppenheimer approximation). So the only variable that will have to meet the limit of our computational capability is the number of electrons. Systems made up of a small amount of atoms, or even periodic systems whose unit cell contains a small number of atoms, especially if said atoms are light are the best targets for *ab initio* techniques. The lightest atoms are, in fact, easy to handle, and the calculation of the systems they make up is not unknown territory at all, because light atoms forming small molecules or periodic systems is the field of biochemistry. Transition metal atoms are much harder to handle, specially the heavier ones. On the other hand, transition metals are the main constituents of any technology that relies on magnetism, so they need to be studied. This is what led us to attempt to calculate the properties of small clusters and thin films of transition metals.

After narrowing down our systems we wondered which ones were specially relevant in those days: In the late 1990s IBM commercialized the first GMR-based device, and because of that, in the very early 2000s the field of ultrathin magnetic multilayers was an increasingly popular topic to research, still with questions open. That was what lead us to start on studying the properties of Fe/Cr/Fe trilayers depending on the Fe layer thickness, which was a topic still untouched. At the same time, throughout the 1990s and the 2000s, the noble metal clusters were studied for potential usability in the medical field. On one hand, they were starting to show relatively high magnetic moments (compared to their bulk state) which could turn them into hyperthermia (cancer therapy where cancerous cells are killed by rising their temperature) agents for cancer treatment by applying a variable external magnetic field, which would cause the nanoparticles to heat up, killing the cancerous surrounding tissue. On the other hand, despite their low reactivity in bulk state, noble metal clusters show some specific reactivity in biological medium, which makes them a very structure-dependent kind of biochemical catalysts. This is what directed us to study the smallest gold clusters.

1.2 The DFT

1.2.1 Ab initio techniques

At the heart of the *ab initio* techniques lies the intention of solving the Schödinger equation for any system where the only relevant interaction is the electromagnetic one[1], i.e. any system where no nuclear reactions or particle disintegrations happen, nor where the masses involved are too large... from everyday objects down to

atomic-sized systems. As simple as it seems, this presents a cyclopean task when applied to the many-body problem: just as in classic mechanics, in quantum mechanics the analytical solution is too unpractical to be searched. A first reduction of the complexity comes from restricting ourselves to the search of the fundamental states of whatever system we are studying: in this circumstance we can remove the time dependency of the Schödinger equation. A second one is called the Born-Oppenheimer approximation: because of the atomic nuclei being much larger and with much lower velocities than the electrons, we can consider their respective dynamics to be decoupled, and we can approximate the nuclei to be static; in this manner we only need to solve the Schödinger equation for a system of N electrons under a potential $v(\mathbf{r})$, and these will be the parameters that will define our system. These simplifications are especially appropriate when we are concerned with study of atoms and molecules, but even then the problem is unmanageable: each wavefunction Ψ is described in an orthonormal basis set; so for an atomic/molecular system with N electrons, the amount of variables grows exponentially with N.

How to find the wavefunction, then? We know that the fundamental state of a quantum system will be the one for which the energy is minimum. Hence we can stablish a variational principle on the energy functional defined as:

$$E[\Psi] = \frac{\left\langle \Psi|\hat{H}|\Psi \right\rangle}{\langle \Psi|\Psi \rangle} \tag{1.1}$$

where

$$\left\langle \Psi|\hat{H}|\Psi \right\rangle = \int \Psi^* \hat{H} \Psi dx \tag{1.2}$$

in which the Hamiltonian operator $\hat{H}$ is the Hamiltonian of an N-electron system

$$\hat{H} = \sum_{i=1}^{N} \left(-\frac{1}{2}\nabla_i^2 \right) + \sum_{i=1}^{N} v(\mathbf{r}_i) + \sum_{i<j}^{N} \frac{1}{r_{ij}} \tag{1.3}$$

with $v(\mathbf{r}_i)$ being the external potential felt by the electron i due to the nuclei of charges Z_α

$$v(\mathbf{r}_i) = -\sum_{\alpha} \frac{Z_\alpha}{\mathbf{r}_{i\alpha}} \tag{1.4}$$

With this in hand, if we perform a full minimization of this functional respect to all possible trial N-electron wavefunctions, down to the ground state energy of the considered system (E_0), the trial wavefunction for which this happens will be the ground state wavefunction (Ψ_0)

$$E_0 = min_\Psi E[\Psi] = E[\Psi_0] \tag{1.5}$$

With the right wavefunction, we can tackle the problem of solving Schrödinger

equation, which is still a complicated differential equation with a number of variables that grow exponentially with N. One of the biggest problems is that the potential $v(\mathbf{r})$ has both a classical electrostatic term and a non-classical exchange-correlation (XC) term. This v_{XC} has no analytical functional form, hence we can only undertake it with approximations.

The first such approximation was the Hartree equation[2], which amounts basically to remove the non-classical XC term out of $v(\mathbf{r})$, and solving the Schroedinger equation by constructing trial wavefunctions as a product of N-wavefunctions (one for each electron). The next piece in the puzzle of the *ab initio* method was provided by the Slater determinants[3], which gives us a way to construct N-electron wavefunctions that strictly respect the electronic exchange, as it follows the Fermi-Dirac statistics. This piece would be fitted shortly after in the Hartree-Fock approximation[4], which is an extension of the Hartree equation to account for the quantum exchange effect among the electrons, using Slater determinants instead of wavefunction products. Nevertheless, the electron correlation contribution was left outstanding. To fix this, solutions have been proposed like Sherrill and Schaefer's configuration interaction method[5], that expresses the trial wavefunction as linear combinations of a electronic states (given their Slater determinant), called configuration state functions. This introduces formally the correlation, but in turn, increases the required computational power to prohibitive levels if we mean to study systems with more than a few electrons.

1.2.2 DFT

As we have seen in the previous section, formally ab initio methods applied to atomic/molecular systems present the main difficulty of the excessive processing power they demand. In order to be able to calculate realistic systems, it was needed to greatly reduce the number of variables; the Thomas-Fermi model was the first step[1]. In 1927 Thomas establishes the original assumptions of the model[6]: *"Electrons are distributed uniformly in the six-dimensional phase space for the motion of an electron at the rate of two for each h^3 of volume"* and that there is an effective potential field that *"is itself determined by the nuclear charge and this distribution of electrons"*. The Thomas-Fermi model substitutes the atom or molecule with an ideal Fermi gas of electrons, only subjected to an effective external potential given by the positions of the electrons and the nuclei. In this manner, we made everything to depend on a single variable, the electron distribution or electron density $\rho(\mathbf{r})$. With two elegant and reasonable assumptions, the Thomas-Fermi model removes the enormous amount of variables that the Hartree-Fock calculations needed. Nevertheless, it is still a model, and while it has worked well to estimate certain atomic properties, provides only a rough approximation for molecular calculations: it can't even predict the existence of the atomic bond. On the other hand, it has proven itself very accurate in the prediction of the properties of metallic systems, as the

electrons that conform the metallic bond can be described as a good approximation of an ideal Fermi gas.

Would it be possible to adopt this approach and use it to actually solve the Schrödinger equation? To solve the Schrödinger equation by substituting all the electrons with a single electron density? Hohenber and Kohn proved two theorems in 1964 that legitimize the use of $\rho(\mathbf{r})$ as basic variable[7]. The first theorem says: *The external potential v(**r**) is determine, within a trivial additive constant, by the electron density $\rho(\boldsymbol{r})$.* Remembering that N and $v(\mathbf{r})$ completely fix the Hamiltonian, and having in account that N is given by $\rho(\mathbf{r})$, it follows that $\rho(\mathbf{r})$ also determines the GS of the wavefunction Ψ, and all the other electronic properties of the system.

The second theorem states: *For a trial electronic density $\tilde{\rho}(\boldsymbol{r})$ such that $\tilde{\rho}(\boldsymbol{r}) \geq 0$ and $\int \tilde{\rho}(\boldsymbol{r})d\boldsymbol{r} = N$*

$$E_0 \leq E_v[\tilde{\rho}] \tag{1.6}$$

where $E_v[\tilde{\rho}]$ is

$$E_v[\tilde{\rho}] = T[\rho] + V_{ne}[\rho] + V_{ee}[\rho] = \int \rho(\mathbf{r})v(\mathbf{r})d\mathbf{r} + F_{HK}[\rho] \tag{1.7}$$

where

$$F_{HK}[\rho] = T[\rho] + V_{ee}[\rho] \tag{1.8}$$

where V_{ee} = classical repulsion between electrons + nonclassical term. This theorem provides us with a variational principle that is analogous to the one for wavefunctions.

With these two theorems, we can move on from the original interacting many-body problem into a fictitious non-interacting system, where each electron is considered separately, and it is subjected only to an effective potential, but restricted to share the electronic density with the many body problem. We are converting an equation with N coupled variables (the wavefunctions of each electron) to a system of N equations only coupled by the electron density. And we are solving the system by using a functional which depends solely on the electron density, which is where the name of DFT comes from.

The biggest problem comes from F_{HK}. In it we have the non-classical part of the energy functional, the E_{XC}. As we have seen in the previous section, a formal accounting of this part of the Hamiltonian would require the consideration of the infinite basis that describe electron wavefunctions, hence removing all the advantage we had won. Instead, E_{XC} is accounted for through different, approximate functionals; for this reason we cannot formally consider DFT as an *ab initio* method, and should be called a mean field theory instead. Nevertheless, to the extent that the theorems DFT is based on are formally *ab initio*, even if a realistic consideration is not, it can be practically considered as such.

Let us enter more deeply on how DFT works; also let us keep in mind that the mathematical derivation that follows is made for a spinless electronic density.

The extension of DFT to spin-dependent systems is almost straightforward, but we do not show it here for simplicity. For a non-interacting system (V_{ee}=0) the Kohn-Sham kinetic energy is obtained with the Levy constrained-search [1] as

$$T_{KS}(\rho_0) = \min_{\Psi \mapsto \rho_0} \langle \Psi | \hat{T} | \Psi \rangle = \sum_{i=1}^{N} \langle \psi_i | -\frac{1}{2}\nabla^2 | \psi_i \rangle \tag{1.9}$$

where the minimization is taken over all the antisymmetric N-electron wavefunction Ψ that yields the ground state density ρ_0. $\hat{T}$ is the kinetic energy operator and Ψ is also the Slater determinant composed from the Kohn-Sham orbitals $\psi_i(\mathbf{r})$. The minimization of the energy functional (Eq. 1.7) using Lagrange multipliers subject to the constrain $\int \rho_0(\mathbf{r})\, d\mathbf{r} = N$ for a system of N electrons with

$$\rho_0(\mathbf{r}) = \sum_{i=1}^{N} |\psi_i(\mathbf{r})|^2 \tag{1.10}$$

takes us to the Euler equation:

$$\mu = v_{KS}(\mathbf{r}) + \frac{\partial T_{KS}(\rho)}{\partial \rho(\mathbf{r})} \tag{1.11}$$

where μ is the Lagrange multiplier. Therefore, for a given external potential of the Kohn-Sham reference system ($v_{KS}(\mathbf{r})$), one obtains the $\rho_0(\mathbf{r})$ that satisfies the Euler equation just by solving the Kohn-Sham equations:

$$\left(-\frac{1}{2}\nabla^2 + v_{KS}(\mathbf{r}) \right) \psi_i(\mathbf{r}) = \varepsilon_i \psi_i(\mathbf{r}) \tag{1.12}$$

where ε_i are the eigenvalues of the Kohn-Sham equations. In DFT, the Kohn-Sham equation is the Schrödinger equation of an effective system (the "Kohn-Sham system") of non-interacting particles that generate the same density as any given realistic system of interacting particles. The Kohn-Sham equation is defined by a local effective (fictitious) external potential, $v_{KS}(\mathbf{r})$, in which the non-interacting particles move. In order to find a more explicit representation of the Kohn-Sham potential, the energy functional is rewritten as:

$$E(\rho) = T_{KS}(\rho) + \int \rho(\mathbf{r}) v(\rho)\, d\mathbf{r} + J(\rho) + E_{xc}(\rho) \tag{1.13}$$

where $J(\rho)$ is the electronic Coulomb energy,

$$J(\rho) = \frac{1}{2} \int \int \frac{\rho(\mathbf{r}_1)\rho(\mathbf{r}_2)}{|\mathbf{r}_1 - \mathbf{r}_2|}\, d\mathbf{r}_1 d\mathbf{r}_2 = \frac{1}{2} \langle \rho(\mathbf{r}_1) || \rho(\mathbf{r}_2) \rangle \tag{1.14}$$

and the symbol || represents the $1/|\mathbf{r}_1 - \mathbf{r}_2|$ operator. Also, the E_{xc} functional in Eq. (1.13) is defined as:

$$E_{xc}(\rho) \equiv T(\rho) - T_{KS}(\rho) + V_{ee}(\rho) - J(\rho) \tag{1.15}$$

This expression summarizes all non-classical interactions between the electrons and the difference of the kinetic energies of the interacting and non-interacting N-electron system. Hence the accuracy of DFT will be determined by the quality of the approximation used for the calculation of $E_{xc}(\rho)$. This is the major problem with DFT because the exact functionals for the exchange and correlation are not known except for the free homogeneous electron gas. However, good approximations have been implemented during the last 30 years. One of the first developed approximations was the local-density approximation (LDA)[8], where the functional depends solely upon the value of the electronic density at each point in space

$$E_{xc}^{LDA}(\rho) = \int \epsilon_{xc}(\rho)\rho(\mathbf{r})\, d^3\mathbf{r} \tag{1.16}$$

where $\epsilon_{xc}(\rho)$ is the XC energy density, known accurately from quantum Monte Carlo and other many-electron methods[9]. The LDA is so accurate for solids that it is still widely used in condensed matter physics, but however it is less used for atoms and clusters because they bear less equivalence to an uniform electron gas although is not a bad starting point. Many generalizations of the LDA of Eq. (1.16) were proposed during the next years after the seminal article in Reference [8], but the first practical one was the generalized gradient approximation (GGA)[10–13],

$$E_{xc}^{GGA}(\rho) = \int \epsilon_{xc}^{GGA}(\rho, \nabla\rho)\rho(\mathbf{r})\, d^3\mathbf{r} \tag{1.17}$$

which introduces the density gradients $\nabla\rho(\mathbf{r})$ as additional local arguments of the XC energy density. Specially in clusters, the GGA functional has improved the results for molecular geometries and ground-state energies. There are other refinements of the GGA functionals, like the meta-GGA ones [14]. These functionals include a further term in the expansion, i.e., the gradient of the density and the Laplacian of the density. The most recent approximations for the XC energy include the hybrid functionals where the exchange part of the energy is substituted by the exact exchange energy calculation using the Slater determinants [15, 16].

The GS density is the electronic density that minimizes the energy functional and hence satisfies the Euler equation. Then, performing the functional derivative of the energy functional and comparing with Eq. (1.11), the Kohn-Sham potential has the following explicit form:

$$v_{KS}(\mathbf{r}) = v(\mathbf{r}) + \int \frac{\rho(\mathbf{r}')}{|\mathbf{r} - \mathbf{r}'|}\, d\mathbf{r}' + v_{xc}(\rho) \tag{1.18}$$

where the exchange-correlation potential is defined as $v_{xc}(\rho) \equiv \delta E_{xc}(\rho)/\delta\rho(\mathbf{r})$. Inserting the Eq. (1.18) in Eq. (1.12) yields finally the canonical Kohn-Sham equations:

$$\left(-\frac{1}{2}\nabla^2 + v(\mathbf{r}) + \int \frac{\rho(\mathbf{r}')}{|\mathbf{r}-\mathbf{r}'|}\, d\mathbf{r}' + v_{xc}(\rho)\right)\psi_i(\mathbf{r}) = \varepsilon_i\psi_i(\mathbf{r}) \tag{1.19}$$

This set of equations has to solved iteratively. How we chose to love them, and what type of basis we use for each wavefunction will depend on the equations implementation.

1.2.3 deMon: density of Montreal

1.2.3.1 Theoretical Approach of *deMon*

deMon (density of Montreal) is a system of programs for DFT calculations of atoms, molecules, and solids [17]. A good way to understand the *deMon* code is to look at it within its historical context. During the 1970's, Slater's Xα method had been tried and abandoned by the *ab initio* community [18]. Part of the difficulty was in the scattered wave, muffin-tin implementation of the time. Major numerical improvements came about through the introduction of Gaussian-type orbitals (GTO) and the use of auxiliary fitting functions in the linear combinations of atomic orbital (LCAO)-Xα program [19, 20]. Other major advances were Axel Becke's introduction of efficient, accurate, atom-centred numerical integration, Vosko-Wilk-Nusair's parametrization of the LDA[21] based upon Ceperly and Alder's accurate quantum Monte Carlo calculations of the correlation energy of the homogeneous electron gas, as well as the emergence of good quality GGAs such as those of Becke [22] and Perdew [23]. By the 1980's, it had become clear that it was time to update the old LCAO-Xα strategy and write a modern DFT program with analytic derivatives capable of automatic geometry optimizations by means of new algorithms like for example the most sophisticated Broyden-Fletcher-Goldfarb-Shanno (BFGS) method [24]. This goal was realized in *deMon*. These and other characteristics make this code one of the most popular among the *ab initio* community. Its main features and the basic theory of its functionalities are explained hereafter.

To avoid unnecessary complications and as commented above, I restrict myself to the closed-shell case. The extension to the open-shell formalism is straightforward and it is explained in detail in Ref. [25]. In *deMon* code, linear combinations of atomic Gaussian–type orbitals (LCGTO) are used for representing Kohn-Sham orbitals. In this ansatz, the Kohn–Sham orbitals $\psi_i(\mathbf{r})$ are expanded into atomic orbitals as:

$$\psi_i(\mathbf{r}) = \sum_{\mu} c_{\mu i}\, \mu(\mathbf{r}) \tag{1.20}$$

where $\mu(\mathbf{r})$ represents an atomic orbital and $c_{\mu i}$ are the corresponding molecular orbital coefficients. With this expansion, the electronic density can be rewritten in

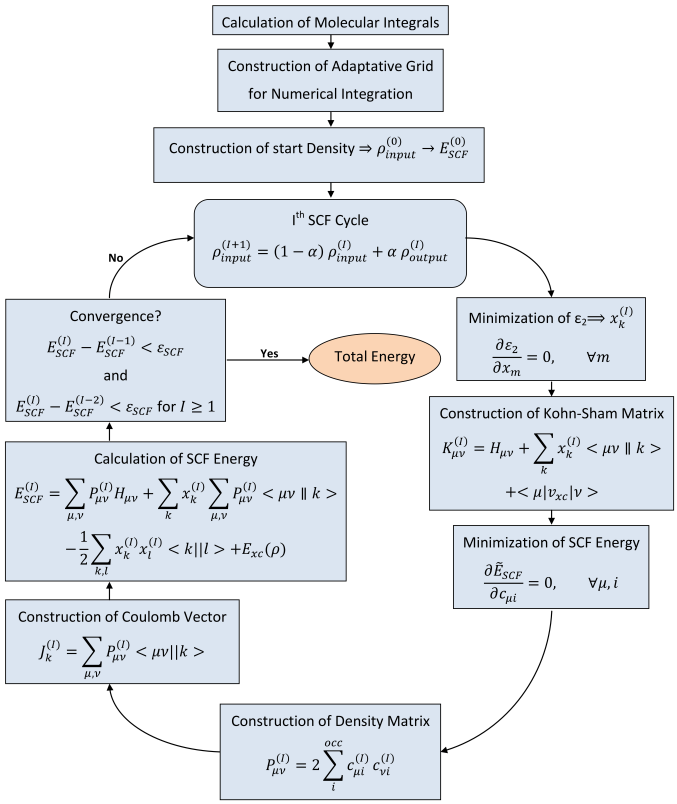

Figure 1.1: Flowchart of the SCF procedure as it is implemented in *deMon* code[26].

terms of the density matrix:

$$\rho(\mathbf{r}) = \sum_{\mu,\nu} P_{\mu\nu}\, \mu(\mathbf{r})\, \nu(\mathbf{r}) \tag{1.21}$$

where $P_{\mu\nu}$ represents an element of the closed-shell density matrix, defined as:

$$P_{\mu\nu} = 2 \sum_{i}^{occ} c_{\mu i}\, c_{\nu i} \tag{1.22}$$

Combining Eqs. (1.20) and (1.21), the Kohn–Sham self-consistent field (SCF) energy Equation (1.13) for a system of $\bar{N}$ atoms can be rewritten in the following form:

$$E_{SCF} = \sum_{\mu,\nu} P_{\mu\nu}\, H_{\mu\nu} + \frac{1}{2} \sum_{\mu,\nu} \sum_{\sigma,\tau} P_{\mu\nu}\, P_{\sigma\tau}\, \langle\, \mu\nu \,\|\, \sigma\tau \,\rangle + E_{xc}(\rho) \tag{1.23}$$

The Kohn–Sham SCF energy collects all terms depending on the electronic density and the SCF convergence procedure is based on this energy expression, as shown in Fig. 1.1. It is also important to remark here that the total energy is the sum of E_{SCF} and the nuclear repulsion energy (they are decoupled because of the

Born-Oppenheimer approximation), which is calculated from the nuclear charges Z_A and atomic position vectors $\mathbf{A}$ as $\sum_{A>B}(Z_A Z_B)/|\mathbf{A}-\mathbf{B}|$. In Eq. (1.23), $H_{\mu\nu}$ is expressed as:

$$H_{\mu\nu} = \langle\mu| - \frac{1}{2}\nabla^2|\nu\rangle - \sum_{C}^{\bar{\mathrm{N}}}\langle\mu|\frac{Z_C}{|\mathbf{r}-\mathbf{C}|}|\nu\rangle \tag{1.24}$$

and it represents the matrix elements of the core Hamiltonian. The matrix elements are the kinetic and nuclear attraction energy of the electrons and describe the dynamics of an electron in the nuclear framework. The computation of the matrix scales formally as N^2, where N is the number of the basis functions. The second term in Eq. (1.23) represents the Coulomb repulsion energy of the electrons and it scales as N^4. However, for the calculation of the $E_{xc}(\rho)$, a numerical integration has to be performed. This integration scales formally as $N^2 \times G$, where G is the number of grid points used to perform the numerical integration. In *deMon*, the calculation of the N^4 scaling Coulomb repulsion energy is avoided by introducing an auxiliary function expansion for the electron density because the calculation of this term represents the most computationally demanding operation. This improvement reduces the formal scaling of the Coulomb repulsion energy to $N^2 \times M$, where M is the number of auxiliary functions (approximately two to three times N). The variational approximation of the Coulomb potential is based on the minimization of the self-interaction error:

$$\varepsilon_2 = \frac{1}{2}\langle\rho-\tilde{\rho}||\rho-\tilde{\rho}\rangle \tag{1.25}$$

This approximated density, $\tilde{\rho}(\mathbf{r})$, is expanded in primitive Hermite Gaussians $\bar{k}(\mathbf{r})$ which are centred at the atoms:

$$\tilde{\rho}(\mathbf{r}) = \sum_k x_k\,\bar{k}(\mathbf{r}) \tag{1.26}$$

With the LCGTO expansion for $\rho(\mathbf{r})$ and $\tilde{\rho}(\mathbf{r})$ we obtain for ε_2:

$$\begin{aligned}\varepsilon_2 =& \frac{1}{2}\sum_{\mu,\nu}\sum_{\sigma,\tau}P_{\mu\nu}P_{\sigma\tau}\langle\mu\nu||\sigma\tau\rangle - \sum_k x_k\sum_{\mu,\nu}P_{\mu\nu}\langle\mu\nu||k\rangle \\ &+ \frac{1}{2}\sum_{k,l}x_k x_l\langle k||l\rangle\end{aligned} \tag{1.27}$$

Because ε_2 is positive definite, the sum of the first and third term is equal or greater than the second term. With this inequality, an approximated SCF energy, which is

based on Eq. (1.23) is derived as:

$$\tilde{E}_{SCF} = \sum_{\mu,\nu} P_{\mu\nu}\, H_{\mu\nu} + \sum_{k} x_k \sum_{\mu,\nu} P_{\mu\nu}\, \langle\, \mu\nu \,||\, k \,\rangle - \frac{1}{2} \sum_{k,l} x_k\, x_l \langle\, k \,||\, l \,\rangle + E_{xc}(\rho) \tag{1.28}$$

Hence, only three–centre electron repulsion integrals (ERIs) are required for the SCF and energy calculation in *deMon*. This represents the most accurate energy model available in this code.

The SCF procedure, as depicted in FIGURE 1.1, may be divided in two parts. The first one is the determination of the fitting coefficients of the approximated density and the second is the determination of the molecular orbital coefficients. Thus, the expansion coefficients x_k of the approximated density are calculated by the minimization of ε_2 restricted to the constrain of the charge conservation ($\int \tilde{\rho}(\mathbf{r}) d\mathbf{r} = n$), i. e.

$$\frac{\partial \varepsilon_2}{\partial x_m} = -\sum_{\mu,\nu} \langle \mu\nu || m \rangle + \sum_{k} x_k \langle k || m \rangle = 0, \;\; \forall m \tag{1.29}$$

Concerning the second part of the SCF procedure, the variation of $\tilde{E}_{SCF}$ with respect to the molecular orbital coefficients, constraining the Kohn-Sham orbitals to be orthonormal yields:

$$\frac{\partial \tilde{E}_{SCF}}{\partial c_{\mu i}} = \sum_{\nu} \left(H_{\mu\nu} + \sum_{k} x_k \langle \mu\nu || k \rangle + \langle \mu | v_{xc} | \nu \rangle \right) c_{\nu i} - \sum_{\nu} \sum_{j} S_{\mu\nu} c_{\nu j} \varepsilon_{ji} \;\; \forall\, \mu, i \tag{1.30}$$

From this equation, we can derive the canonical LCGTO Kohn-Sham equations in matrix form,

$$\mathbf{K}\,\mathbf{c} \;=\; \mathbf{S}\,\mathbf{c}\,\varepsilon \tag{1.31}$$

with the elements of the Kohn-Sham Matrix $\mathbf{K}$ defined as:

$$K_{\mu\nu} = H_{\mu\nu} + \sum_{k} x_k \langle \mu\nu || k \rangle + \langle \mu | v_{xc} | \nu \rangle \tag{1.32}$$

where $\mathbf{c}$ is the molecular orbital coefficient matrix, $\mathbf{S}$ represents the overlap matrix, and ε the Kohn-Sham orbital energies. Thus, as can be seen from FIGURE 1.1, the calculation of the molecular core and electron repulsion integrals, as well as the construction of the grid for the numerical integration of the exchange-correlation contributions are outside the SCF loop. From the start density, which is obtained from the core Hamiltonian, the first Coulomb vector $J_k^{(0)} = \sum_{\mu,\nu} P_{\mu\nu}^{(0)} \langle \mu\nu || k \rangle$ is constructed. With this vector, the expansion coefficients of the approximated density

are calculated and then Kohn-Sham matrix is built. From the diagonalization of the Kohn-Sham matrix a new set of molecular orbital coefficients is obtained. The density matrix is constructed from the new molecular orbital coefficients and then a new Coulomb vector is generated. The SCF cycle is repeated until energy convergence is achieved. Thus, the SCF procedure is terminated once three consecutive values of the total energy differ by less than ε_{SCF} among themselves. In case that the convergence is not reached, the electron density produced by the Ith iteration is mixed with the input density for the Ith iteration to produce the input density of the next iteration:

$$\rho_{input}^{(I+1)} = (1-\alpha)\rho_{input}^{(I)} + \alpha\rho_{output}^{(I)} \tag{1.33}$$

where α is the mixing parameter varying between 0 and 1. The mixing can also be performed with respect to the xc potential, or alternatively, with respect to the whole density matrix.

1.2.3.2 Computational Considerations

Before moving on from the description of the code, there are some notes that must be made, in regards to its implementation.

The basis sets: Basis sets are created in the space defined by the Kohn-Sham equations for each atomic species, using LCGTOs that best describe the electronic orbitals of the neutral isolated atom[27], and usually come from the contraction of slater-type orbitals: in this manner, the basis are described simply by their contraction patterns[28]. The patterns for each basis are arranged in shells, and a shell collects all contracted orbitals of the same angular momentum quantum number like p_x, p_y, p_z or d_{xx}, d_{xy}, d_{xz}, d_{yy}, d_{yz} and d_{zz}. The GTOs of which the contracted orbitals ($\mu(\mathbf{r})$) are lineal combinations, are called primitive orbitals ($g(\mathbf{r})$):

$$\mu(\mathbf{r}) = \sum_{k=1}^{K} d_{\mu k} g_k(\mathbf{r}) \tag{1.34}$$

$$g_k(\mathbf{r}) = (x-A_x)^{a_x}(y-A_y)^{a_y}(z-A_z)^{a_z} e^{-\zeta_k(\mathbf{r}-\mathbf{A})^2} \tag{1.35}$$

The exponents ζ_k and contraction coefficients $d_{\mu k}$ are listed in free format under the shell definition line, one line for each primitive orbital[29].

These bases do not always consider all the electrons in the atom, but sometimes they only do it for the outer shells (in this case we will need effective-core potentials (ECPs) which we will see below); this is particularly true for atomic species that have a large amount of electrons.

The auxiliary basis sets: These basis work in all aspects as the main ones, with the only difference that they are used, as we said in the previous section, to

avoid the formal computation of the Coulomb repulsion energy, term which scales with N^4.

The Effective Core Potentials: Many atomic species have a very large number of electrons. Considering them all complicates the calculation, sometimes making it not a useful tool to analyse the system. Furthermore, the actually interesting phenomena, like atomic bonding, repulsion... happen chiefly in the outer electronic shells. So it makes a good deal of physical sense only calculating these outer electrons, while we substitute the nuclei and the inner electronic shells with an effective potential, called effective core potential. ECPs in *deMon* are defined according to the functional form[29]:

$$U^{ECP} = U_L + \sum_{l=0}^{L-1} \sum_{m=-l}^{l} \left[U_l(r) - U_L(r)\right] |l,m\rangle \langle l,m| \tag{1.36}$$

$$U_l(r) = \sum_{i=1} C_{li} r^n e^{-\zeta_{li} r^2} \tag{1.37}$$

where the radial power n must satisfy $n \geq -2$. Positive coefficients C_{li} correspond to a repulsive contribution to the potential.

It is worth of note that these ECPs sometimes need to be tweaked to account for relativistic phenomena, like the spin-orbit coupling. For these cases, the relativistic (RECPs) and quasi-relativistic (QECPs) effective core potentials were built.

1.3 The research subject: Transition Metals

Once we are intent on testing ab initio methods on a per-case basis, and we have chosen to use the DFT approach through the *deMon* code, the next step is to select the systems we will study. In principle, it seems like a good idea to stick to systems with a reduced number of atoms, to be able to perform the calculations in a reasonable time. This needs not to be the case, however: by using periodic boundary conditions, the properties of periodic systems like crystals can be calculated, as long as the unit cell does not contain too many atoms. In any case, having a tool that works better for smaller number of atoms, and that allows us to predict the properties of system of reduced size and low dimensionality, whose production is technically complex and expensive, it makes sense if we begin by exploring those systems.

Non-metallic, alkaline metallic and noble gases atomic species are not difficult to modelize to a great degree of accuracy. Their outer orbitals are either s or p, whose description, or even of their hybridization's, are well known. Transition metals, on the other hand, are characterized by their outer d orbitals, which contains up to 10 electrons, with shapes that are not as easily spherical or directional as s and p are. Not only they have a large number of electrons in denser volumes, also the different spin states of said electrons are energetically close to each other, so the magnetic

state is not trivial, and can change easily depending on each atom environment. These closely packed electrons create an environment where the quantum correlation effects will be large. Although electronic correlation can ultimately be handled by the DFT, there are more difficulties that need to be addressed, like open-shell systems involving a large number of electrons, degeneracy in the molecular orbitals, electrons from the ECPs sharing regions of space with valence electrons, relativistic corrections for heavier elements due to the high velocities their innermost electrons possess, spin-orbit coupling, among others... and this is just to calculate the ground state of an atom arrangement. Usually we want also to know the spatial configuration of the atomic arrangement that minimizes the energy, we want to perform a geometry optimization. This involves the calculation of the forces acting upon each atom, through the gradient of the electronic potential, and then allow the atoms to move slightly according to the said forces. This iterative relaxation of the initial structure is the part of the calculation that demands the most computing time.

Even then, DFT has shown a remarkable accuracy in the calculation of the properties of systems made up with transition metals. This accuracy might blur the divide between theoretical physics and experimental physics, because, in a very real sense (as we are using approximations of the fundamental laws that govern matter, i.e. ab initio techniques), it could be said that we are measuring a theoretical description of the system.

Without reliable models, small structures made of transition metals, whether clusters, nanoparticles or nanowires and thin films, seem to be the systems that can benefit the most from being studied using DFT.

1.3.1 Ultrathin Multilayers

The interest on ultrathin multilayers of magnetic materials did not take off until the theoretical possibility of magnetic coupling of thin layers across non-magnetic ones was verified experimentally, with the works on rare-earth[30] and Fe/Cr multilayers[31] (in this last case, it was observed that the coupling between Fe layers through Cr spacer was AFM). Shortly after, an unusual magnetorresistive effect was found in multilayers[32], and this phenomenon was later clearly observed and described by Baibich *et al.*[33]; the changes in the resistivity were so large that it received the name of giant magnetorresistence (GMR).

Let us describe the GMR more slowly[34], with the very same metals used by Baibich *et al.*, a Fe/Cr superlattice, but taken for simplicity to the simplest case: a trilayer of Fe/Cr/Fe. Under small external magnetic fields the Fe layers are AFM coupled, what results in a net zero magnetic moment, but a strong enough field will make the MMs of the Fe layers switch to align with itself. Now, let us consider a simple Mott mechanism, so there will be 2 conduction channels, one for spin up and another for spin down. The strongly ferromagnetic atomic species, Fe, Co and Ni, are known to have a very different scattering rate for electrons depending on whether they are aligned or not with the magnetization of the ferromagnet. With

this we can make a very simple resistor model to convince ourselves that a multilayer of ferromagnets with spacers will have very different conductivity depending on whether the FM layers are coupled in FM or AFM configuration. Nevertheless, it is important to note that the origin of the GMR is not because of the different scattering that spin-up and spin-down electrons suffer inside the FM layers; instead, it happens because of the contrast between the scattering lengths that spin-up and spin-down electrons suffer in the interface.

In the ultrathin multilayer research boom during the discovery of the GMR produced, and deeply bonded to this property, a new phenomenon was discovered in superlattices: for some materials, the coupling between the FM layers had an oscillatory dependence with the spacer thickness. This was first observed in rare earth metals, such as Gd and Y[35], but not until the work of Parkin *et al.* was it found for transition metals[36], and described as a RKKY-type oscillation.[1]

The first studies of the coupling dependence with the spacer layer thickness, made on single-crystalline multilayers, had found that the coupling between the magnetic layers remained AFM for all spacer layer thickness, decreasing in coupling strength. This changed with Parkin's *et al.* findings and the interest arisen was obvious: the GMR effect depends on the possibility of switching between AFM and FM coupling, because this is what, in turn, causes the change of the multilayer conductivity.

This oscillatory coupling is not restricted to Cr as spacer. In fact, most transition metals show this behaviour, when used as spacer layer[34], with the obvious exceptions of the 3 ferromagnets: Fe, Co and Ni. It has been observed that there is a growing dependence between the number of d electrons and the strength of this oscillatory coupling, and decreasing with Z. Indeed, starting with the Ti, Zr and Hf, for which either the coupling is too low or no coupling happens, there is only a few exceptions: while Ag and Au do not seem to show any AFM stage to their coupling dependence on layer thickness, their coupling do oscillate, what makes it seem like something is masking this AFM coupling (it is speculated it can be the lattice defects); on the other hand Pd and Pt exhibit strong FM coupling as spacers, probably because both species are readily magnetically polarized by the magnetic layers, which lead to the the development of strong MMs in the spacer layers themselves. Not only this behaviour is habitual for transition metals: they also seem to have very similar values for the λ of this oscillation, around 10 Å, with the exception of Cr. This makes no sense in the RKKY model for oscillatory magnetic coupling in multilayers, because the RKKY period is related to the details of the topology of the Fermi surface, so the model has to be refined with explicit treatment of certain elements. As we see, the thickness of the spacer layer had been a subject to which

[1] The Ruderman-Kittel-Kasuya-Yosida interaction, or RKKY, describes the damped oscillatory magnetic coupling induced in a paramagnetic metal by a localized magnetic impurity. From this it follows the conduction electrons in the vicinity of this impurity will experience a damped oscillatory spin polarization as a function of their distance with it.

great attention was devoted, both experimentally and using *ab initio* techniques. But the effects of the thickness of the FM layer in the surface effects was largely unexplored, which is why we decided to focus our efforts on it.

1.3.2 Nanoparticles and Atomic Clusters

Ultrathin layers and multilayers, despite being essentially 2-D in their most interesting properties, still represent continuous media. Our next step took us to the mesoscale, what lies between that and the atomic scale, to the atomic clusters. Atomic clusters are aggregates between ≈ 5 and $\approx 10^5$ atoms whose properties that differ from both the individual atoms and molecules, and from the continuous macroscopic matter. This is precisely one of the academic interests on clusters: their study helps us understand the transition between the properties of matter in atomic/molecular state and in bulk state. Studying them in increasing sizes, we can see how typically bulk properties arise, like band structure, phonons, plasmons, phase transitions and conductivity, among many others, and gain a better understanding of how they work. On the other hand, their unique properties make them technologically attractive: nanoelectronics, spintronics and medicine are the fields that most benefit from them.

Metallic clusters and nanoparticles, particularly of noble metals, have been with us for longer than we could realize at first. Gold nanoparticles, for example, have been used as colourants since XVII century in luxury glass manufacturing by dissolving gold on molten glass before vitrification and later reheating[37]. Also, colloidal gold and silver potions were considered to be remedies for almost every disease in the Middle Ages (maybe because noble metals would not kill on consumption), a superstitious belief that has resurfaced nowadays in the pseudo-scientific homoeopathic "therapies". It is therefore, an ironic coincidence that cluster research has shown that metallic nanoparticles have their role in modern medicine.

Nevertheless, the modern atomic clusters are not obtained through solution and vitrification. There are two paths that allow us to create metallic clusters: on one hand we can simply have a vapour of the metallic atoms, and allow them to coalesce. The size of the clusters is highly dependant on the method used to create the vapour from the bulk metal, and on the focus of said method. Common devices for the smallest clusters are pulsed lasers and ion sputtering, which dislodge individual atoms from the metallic crystal, allowing for a very narrow control of the size. On the other hand we can use chemical reactions, where reactive molecules contain the metals we wish to grow into clusters, and the products slowly accumulate said metals, leaving the rest of the molecule as a left-over. Organic compounds are very often the molecules of choice, because of their ease to form large chains of polymers, with each monomer containing the metallic atom.

While the latter method is comparatively much cheaper than the former, it has the drawback of the clusters being surrounded by a matrix of organic molecules.

Furthermore it is harder to find suitable compounds for certain metals, such as the noble metals, which rarely interact chemically with other atoms.

As we have said, atomic clusters have very different properties from the individual atom and from the crystalline state. Noble metals, known as such because of their very low reactivity, become surprisingly reactive when forming clusters of a few tens of atoms; not only that, they are known to have catalytic capabilities in organic reactions. Also they are known for their very low magnetic moment per atom, being strongly paramagnetic. Nevertheless, surprisingly high magnetism was found shortly after this thesis was started for a cluster as small as 13 atoms of silver[38], and smaller but comparable magnetism was expected for gold clusters too. Gold clusters also offered other striking properties, like their affinity for planar and hollow-cage structures. This was the reason the work on clusters for this thesis focused on gold clusters.

2

A 2D system: electronic and magnetic structure of Fe/Cr/Fe ultrathin trilayers.

> *We are told from childhood onward that everything we want to do is impossible. We grow up with this idea, and as the years accumulate, so too do the* ***layers*** *of prejudice, fear and guilt. There comes a time when our personal calling is so deeply buried in our soul as to be invisible. But its still there.*
>
> *[Paulo Coelho]*

2.1 Introduction

As we said, the ultrathin multilayers are among the most widely used nanostructured systems within the current computational technology. Their properties had already been subject of extensive research by the time we had started our own work on them.

This research had chiefly explored to great depth the dependence of the magnetic properties of multilayers with the spacer layer thickness[39, 40], due to, as we have seen, the modulability of the GMR effect depending on said magnitude. In the meanwhile, the effects of the FM layer thickness had received little attention. This led us to think it was a topic with great promise, as the FM layer thickness affects the properties of the multilayers, as found by Bloemen *et al.*[41].

The magnetic multilayers are often studied theoretically through modelization. They are parameter-adjusted models that deal with electronic and magnetic transport properties, readily measured in experiments, and come from the continuity equations like the Boltzmann equation [42, 43]. Nevertheless, to understand why

this transport (macroscopic property) happens, we first need to determine how the magnetic moments of the atoms of the trilayer couple with each other, we need to know their electronic and magnetic properties (microscopic properties). This is what we attempted to achieve with through our ab initio calculations.

Our goal is to find the magnetic structure of these trilayers from ab initio calculations and to discuss the electronic distribution, looking for the anomalies and dependencies that might happen when increasing the FM layers thickness. In order to optimize the simplification of the problem, we decided to use Fe/Cr supercells, first studied by Okuno *et al.*[44], and then took the simplest supercell system, which consists in two FM layers (made of Fe) separated by a spacer (made of Cr): a magnetic trilayer. While it would seem the best choice for a spacer layer is a non-magnetic material, this needs not to be the case. Cr is often selected to go with Fe because it couples AFM with it (in addition to Cr monolayers being coupled AFM with each other), which increases the energy difference between the P and AP states of the FM layers. For our calculations, we fixed the thickness of the Cr slab to 3 MLs. The distance between planes is $\frac{a}{2}$, being a the lattice parameter. The thickness of the Fe slab will vary between 1 and 6 MLs. All the atoms, either Fe or Cr are considered into a bcc lattice with a lattice parameter of $a = 2.88$ Å.

2.2 Computational Details

We have performed our calculations with the deMon-KS [17] electronic simulation software, through its extension for periodic systems, the Bloch-deMon [45]. Bloch-deMon performs AE-LCGTO to solve iteratively the KS equations. We will approximate the exchange-correlation energy through the LSDA [21]. Even though the generalized gradient approximation provides more accurate results, Herper *et al.* verified that this is due to a better geometry optimization [46]. Since the atomic positions were well known for our systems, LSDA was adequate [47]. The crystalline structure of our system was considered as bcc, fitting with the known crystalline structures of both Fe and Cr bulk metals [48]. In thin layers, it was known that for 3 MLs, the stable Cr structure is an unstrained bcc [49]. Furthermore, we assumed that the bcc structure was going to be held all along the system with the same lattice constant: $a = 2.88$ Å, because it had been found that the difference between studying the system using both lattice constants for each respective metal slab, and using only one for both metals, was negligible [47]. For the above reason, we did not allow any relaxation of the structure.

Regarding to computation parameters, the integration over the Brillouin zone was performed on a 74 k-point mesh. According to the convergence tests, this one proved to be a sufficient density for an accurate calculation (within 10^{-4} hartree per atom) of the ground state. We chose our energy convergence criterion in 10^{-4} hartree because the energy difference between two contiguous magnetic configurations can be as narrow as 10^{-3} hartree. The Bloch-deMon allows for a precise

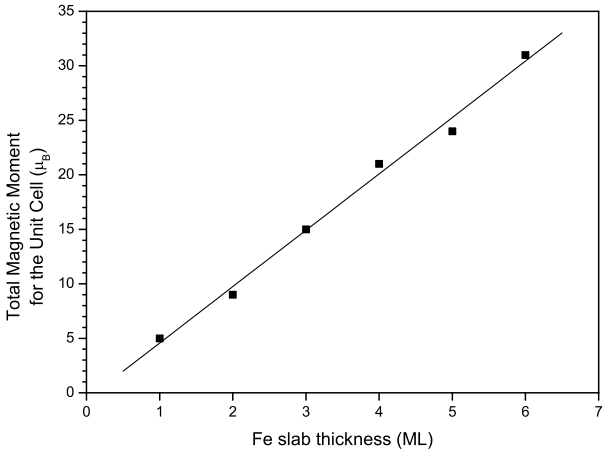

Figure 2.1:
Total magnetic moment of the unit cell of each of the systems we have calculated. The points that correspond to a thickness of the Fe slab of 1,2,3,4,5,6 have been fit linearly: $y = A + Bx$, where $A = -0.0 \pm 0.6$ and $B = 4.8 \pm 0.2$ (Error given in square mean deviation).

approach to the calculation of the magnetic properties: while we perform a variational search in the total magnetic moment per unit cell for the minimum energy, the program calculates all the energy levels of every atom in the unit cell and fills them individually up to the Fermi energy, in the way that keeps the input total magnetic moment. We used the following GTOs: for Fe atoms, the orbital valence basis set with the contraction pattern (43321/421/31) and the auxiliary basis set (9,3;9,3). For Cr atoms, we used the orbital valence basis set with the contraction pattern (63311/531/31) and the auxiliary basis set (5,3;5,3) [27]. To remove linear dependences, we saw ourselves in need to modify the basis sets.

2.3 Results and Discussion

2.3.1 Magnetic Structure

To gain a picture on the general trend of the magnetic behaviour of these trilayered systems, we first analysed the behaviour of the magnetic moment (MM), both for the whole system and for individual atoms. This will allow us to find their periodicities and anomalies. We plot in Fig. 2.1 the growth of the total magnetic moment of the 2D unit cell. As expected, it grows linearly with the thickness of the Fe layer, since we have imposed the two Fe slabs to be FM with each other. This linear dependence has a slope of 5.2 μ_B/atom, and an offset of -0.6 μ_B.

A plot of the MMs of each atom from the unit cell can be examined in Fig. 2.2. As a comparative value, in this figure there is also a plot of the MM per atom (MMA) of the ground state of the bulk bcc Cr. This ground state shows a magnetic configuration that is very similar to a spin density wave (SDW), so we take the maximum of its amplitude, 0.59 μ_B [50]. The MMA for bulk bcc Fe, 2.2 μ_B, is plotted as well. In Fig. 2.2 we see that the MM of the Fe monolayers (MLs) are all coupled FM with each other. The MMs of the Cr MLs couple AFM with each

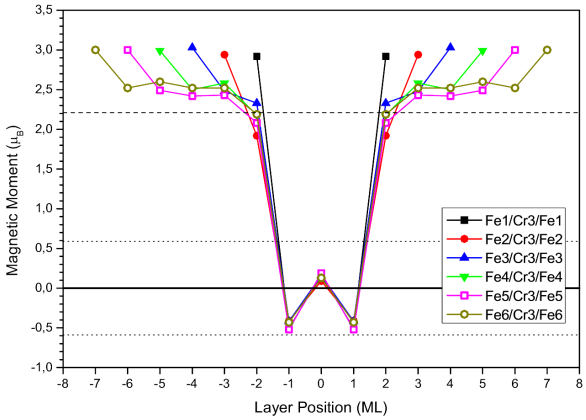

Figure 2.2: Magnetic moments per atom (MMA) for all the systems. The layer position is considered taking the centre in the central Cr ML. The values of the MMA of the bulk Fe, 2.21, and of the maximum of the SDW in bulk Cr, 0.59, are outlined as dashed and dotted lines, respectively.

other and with the Fe ones. The Fe atoms in the surface of the trilayer have a higher MM than the other ones, around 3 μ_B, higher than the bulk value, because the border effect causes them to have many electrons out of the metallic bond, whose spin cannot be balanced. The Fe atoms in the interface with the Cr ones have a MM slightly smaller than the bulk value because, as we will show below, the interface Fe atoms are drained of electrons by the Cr atoms. The other Fe atoms will have a MM around 2.4 μ_B, slightly higher than the bulk value. The increase of the thickness of the Fe slabs in 1 ML implies adding 2 Fe atoms to the unit cell in the inner region of the slab, where they will have a MM of 2.6 μ_B, what produces the slope we observe.

On the other hand, the MMs of the Cr atoms at the interface range from 0.4 μ_B to 0.5 μ_B, close to the maximum of the incommensurate SDW observed in bulk Cr, 0.59 μ_B, coupled antiparallelly to the interface Fe. The central Cr has instead a low MM, ranging from 0.1 μ_B to 0.2 μ_B, coupled antiparallelly with the interface Cr ML. The resultant behaviour is remarkably similar to a commensurate SDW, such as the ones found for much thicker Cr slabs by Niklasson et al. [51]. This is what was expected from the magnetic phase diagram of thin films for a thickness of 3MLs and a T=0K, as seen in the excellent review by Zabel [52], but the existence of SDWs for such thin Cr film is not well defined. Nevertheless, the profile of the MMs we found for the Cr atoms corresponded with the SDW state, and did not fit with the other two possible options: paramagnetic [53] and normal AF [54]. Previous calculations using non-ab initio methods (tight-binding) with trilayers of similar thickness had not found SDW [54]. The SDWs have double periodicity: [51, 55] a short range wave, with period of 2MLs [53], and a long range one, whose period shows a discontinuous dependence on the thickness of the Cr layer. In our case, being only 3MLs thick, both periods match. The behaviour we calculated is similar to one-SDW order found through *ab initio* calculations in Cr ultrathin layers sandwiched by Fe [56], where the MM of the Cr MLs closer

to the Fe are greatly affected by it [52]. Nevertheless, this magnetic ordering for Cr interlayers appears when they are thicker than 33 MLs. For interlayers thinner than 21 MLs the SDW order corresponds with a half-SDW [57]. This apparent contradiction with our results happened only because we restricted the calculation to a FM configuration between both Fe slabs while having an odd number of Cr MLs. As Cr atoms couples AF with Fe ones, the only possible SDWs in Cr are either non-SDW or an integer number of SDWs. For the case of the Fe atoms, the MMs we found were in good agreement with the results of Herper *et al.* [58] and Klautau *et al.* [59]. The MM profile of the Fe atoms found in Ref. [58] even shows their electronic depletion we had found in the interface. Comparing with the study of Fe/Cr supercells with different thickness in Ref. [59], we obtained very similar values for the Fe MMs, with the outer Fe layer being an obvious exception, since inside a supercell there will be no surface effects. The Cr MM were, on the other hand, larger in our calculations, what hints that interfacial roughness would have a larger effect for Cr atoms than for Fe. Another difference with some of the literature is that we predicted the appearance of SDW in the Cr slab while in the work of Klautau, the MM of the Cr atoms of different monolayers share the same absolute value. Our Cr MM were, instead, almost identical to the ones obtained through tight-binding *ab initio* calculations by Stoeffler and Gautier for Cr spacers of 10 MLs thick [60]. One of our colleagues performed in the past a set of calculations very similar to our current ones with a different computational method [61] and we obtain similar results for the general behaviour of the Fe atoms, but where he found an anomalously large FM MM for the interface Fe layer in the systems $Fe_5/Cr_3/Fe_5$ and $Fe_7/Cr_3/Fe_7$ whereas now we did not, now. Because we used the same geometry, discrepancies can be due to the mesh of only 45 k-points used by Pereiro *et al.*, which we verified to be insufficient for these systems.

2.3.2 Charge Distribution and Electronic Structure

A summary plot of the charge distribution of our 5 systems appears in Fig. 2.3. In this graph we represent a total MPA of each atom minus their respective Z, to give an idea of the electron excess/defect that each atom presents with respect to their isolated, neutral state.

Since this system has a specular symmetry with respect to the central ML, we show only half of the trilayer. The most obvious feature is the charge excess peak in the central Cr ML; then the MPA of the consecutive atoms of the unit cell oscillates between electronic excess and defect. The interface Cr layer has a Mulliken population very close to the Cr atomic number, but slightly higher. This small deviation from the behaviour of the other systems becomes large when we separate the charge transfer along the unit cell in their spin up and spin down components. The Fe interface layer is the main electron donor, giving up between 0.4 and 0.5 electrons per atom, independently of the system. The electron excess/defect of the remaining Fe layers will oscillate decreasingly.

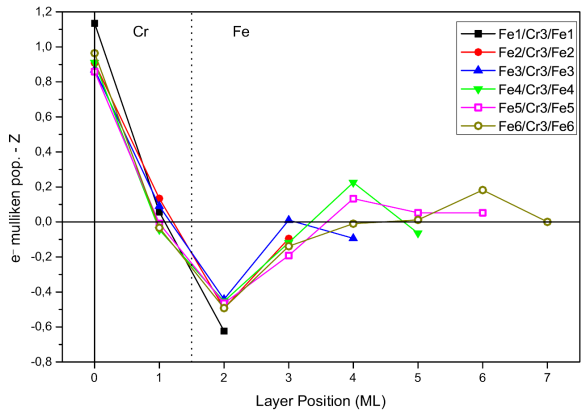

Figure 2.3:
Deviation of the Mulliken population of the different atoms of the unit cell with respect to their Z, giving account of their electronic excess or deficiency. Layers are numbered from the central Cr ML. Because of the symmetry of the systems, we only need to represent half of each trilayer. We separate with a vertical dotted line the Cr and the Fe atoms.

The electron injection and depletion happens in the orbitals S and D: in the inner Fe MLs, mainly in the S orbitals, while for the Fe interface MLs it happens in the D orbitals; this is why the electron defect in the Fe interface MLs leads to the smaller MM we have seen in the previous section. Directionally, we found that among the D orbitals, the charge displacement happens mainly in the orbitals with a component on the direction perpendicular to the slab.

A striking feature was that the oscillation of the difference between the Mulliken population and the atomic number Z for each of the Fe atoms follows roughly a Friedel-like oscillation, which would arise from the discontinuity between the Fe and Cr slabs [62]. Despite our system not being at all the type of system where Friedel oscillations belong, we performed a parametrical fitting of this difference to the said oscillation: $f(x) = A\cos(Bx+C)/x$, for all the systems except the 131 one (because there were not enough points). The coefficients found are shown in Table 7.1. B has an actual physical interpretation, since $B = 2\,k_F$, where k_F, relates to the E_F through the equation: $E_F = \hbar^2\,k_F^2/2\,m^*$, where m^* is the effective mass of the electrons in the system. With this relation, we can estimate the value of the m^*, because E_F is a value given by our calculations, with this equation:

$$m^* = \frac{\hbar^2\,B^2}{8\,E_F}. \tag{2.1}$$

Our results for the effective mass are also shown in Table 2.1. We obtain low values, ranging from 0.1 to 0.5 times the free-electron mass, due to the reduced dimensionality (2D) of our systems [63]. These values are rough approximations, in any case, because for such thin films too few points are available to perform an accurate fitting of the parameters, since we are using finite charge to study a behaviour that depends formally on charge density (even accepting the validity of using the Friedel oscillation formula for an ultrathin multilayer). The general trend observed is that effective mass decreases as the Fe slabs grow thicker. Such behaviour corresponds with what was reported by Johnson et al. [64]. And it

Table 2.1:
Value of the three different parameters of the curve-fitting of the difference between the Mulliken population and the atomic number Z of each atom of the system 232, 333, 434, 535 and 636, to a Friedel-like oscillation ($f(x) = A\,\frac{\cos(Bx+C)}{x}$). Units for the parameters are: A is in positive electron charges (e), B is in MLs (distance between 2 consecutive monolayers is 1,43 Å) and C is a dimensionless phase (radians). Next to them, the value of Fermi energy obtained from our theoretical calculations (in eV), and the value we calculated for the effective mass (m^*) from Eq. 2.1, in electron masses (m_e).

system	A	B	C	E_F	m^*
232	1.0	1.5	-0.06	-1.9	$\simeq 0.5$
333	0.9	1.6	-0.17	-3.7	$\simeq 0.3$
434	0.9	1.5	0.07	-3.2	$\simeq 0.3$
535	0.9	1.3	0.25	-3.6	$\simeq 0.2$
636	0.9	1.0	0.66	-3.4	$\simeq 0.2$

happens because the hybridization between the orbitals of the Cr atoms with the orbital of the Fe atoms is less important the thicker the Fe slab is. It is to be noted that the effective mass is not well defined for transition metals, since the free electron approximation is not valid for them. Nevertheless, systems with reduced dimensions (in our case 2D ones, like multilayers and superlattices) will not be entirely metallic as the bulk would be. In this case, effective mass can be used, not as an approximation, but as a useful tool to help describe the conductivity variations that can happen, such as GMR or GMR-like conductance [65]. Though all the MLs follow approximately this distribution, the surface Fe one will have a population close to the opposite to what it would have according to the model. This compensates for the trilayer not being infinite-layered, ensuring that there is no net excess or deficiency of electrons in the system. Hence, we have decided to remove these points from the fitting. Friedel oscillations arise from impurities inside a bulk or abrupt changes in the electronic structure. In the case of a point-like impurity, a true Friedel oscillation of the electronic density would have a singularity for where the impurity is. Integrating in the space coordinates, to transform charge density into electric charge, would yield an oscillation similar to the ones we obtain in Fig. 2.3. Nevertheless the system is not a bulk with impurities, but a trilayer, so we cannot have true Friedel oscillations. Yet, if we consider only our unit cell, this could be assumed to be a 1D system (the unit cell being a perpendicular string of atoms perpendicular to the 2D system). Under this assumption, the central Cr atoms could be considered to be the impurity, a result that is interesting. If the Fe slabs were much thicker, this behaviour would be completely expectable, but we have found it is conserved even for much thinner Fe slabs.

The magnetism and the electron distribution of a system are given by the electronic microscopic structure. Also, electronic transport depends on two factors that come from the electronic structure: the scattering probability and the electron mobility. The scattering probability, simply from Fermi's golden rule, will be larger

if there are more available states for that electron, i.e. larger value of the density of states (DOS) at Fermi energy ($DOS(E_F)$). Through our calculation, the DOS, but not the electron velocities, are known. From the analysis of the DOS of each system, we can study the contribution from the different MLs to the total DOS at Fermi energy and we find that the Fe surface ML will have the largest contribution, followed by the Cr and Fe interface layers. Middle Cr ML will always have the smallest contribution. For the Fe middle layers, there are not enough data to stablish trends. With the DOS data we can also estimate the exchange splitting (XS). The XS gives an approximate idea of how active the system is magnetically. We find that the XS is -1.0 eV for the 131 system, -1.1 eV for the 232, -1.6 eV for the 333, -1.7 eV for the 434, -1.7 eV for the 535 and -2.0 eV for the 636. As we increase the thickness of the Fe slab, the XS grows very slowly, except for an abrupt change: a sudden rise from 232 to 333, due to a qualitative change in the structure of the Fe slabs: the 333 system has a middle Fe ML, while the 232 one only has surface and interface Fe MLs. This gives an idea of how quickly a low dimensional system can retrieve some bulk-like characteristics: estimating the XS in the same way we did, for bulk Fe it has a value of -2 eV. It should be noted that the values we obtain for the XS include the Cr spacer as well. But this does not diminish the fact that there is an abrupt change in this property because of the apparition of a central Fe ML, and hence, bulk-like characteristics.

It is well known that the interface spin-dependent scattering between the slabs is a key factor of the spin-dependent resistivity in multilayers [66–68], phenomenon which is the origin of the GMR. Most of the interface dependence found in them is related to the roughness in the interface, and the mismatch between the band structure of both slabs [69]. In perfect interfaces, though, there is yet a third factor we might take into account. If the electron finds a different value of resistivity when it crosses a certain interface, there will be a reflection term, even if it goes to a region with a lower resistivity. This reflectivity will also contribute to the interface resistance. In Fig. 2.4, we plot the jump of the $DOS(E_F)$ value from the interface Fe ML to the interface Cr ML, both for the spin up and spin down channels, along the 6 systems we have calculated. A large difference between the jump of the spin up and the spin down channel will imply that the reflectivity term we have mentioned will be noticeably different for the spin up and the spin down electrons, hence contributing to a global spin dependent resistivity in the interface. This factor is important in the system 131 and it is almost negligible in the rest, except for the systems 333 and 636. It is to be noted that this jump in the DOS value appears to be controlled by the spin up channel, since the jump values in the spin down are regularly smaller (except in the system 131, that is qualitatively different).

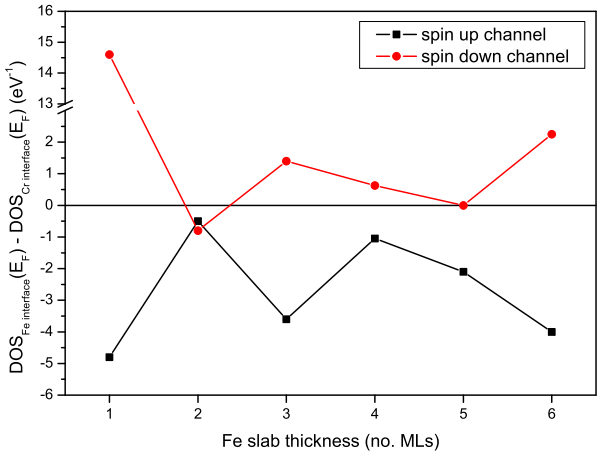

Figure 2.4:
Evolution, with respect to the thickness of the Fe slab, of the difference between the DOS at the Fermi energy of the interface layers of Fe and Cr, both for the spin up and spin down electrons.

2.4 Conclusions

My first approach to the computer simulation of solid state systems in the nanoscale provided us with very important lessons on how to approach this kind of research. Ab initio calculations require much more computing resources (chiefly time, memory and processing power) than modelization, to study the same systems. For this reason, they are expected to provide much more accurate and reliable results, but also, they compel us find ways in which to optimize those resources. Our calculations on $Fe_n/Cr_3/Fe_n$ ($n = 1 \rightarrow 6$) ultrathin trilayers were done without a geometry optimization, because it was deemed too costly. While this at first could seem to be an important loss of accuracy, we have shown in Sec. 3.2 that it was acceptable. On the other hand we also have to accept software limitations: our initial intent was to calculate both FM and AFM configurations of the Fe slabs, but only the FM one was doable. Bloch-deMon was an extension to periodic boundary conditions of a program designed to calculate atoms, molecules and atomic clusters: a finite amount of atoms. As such it only accepted discrete amounts of μ_T, which is correct for molecules, but periodic systems can discrete values of μ_T when averaged per unit cell. This was the case, according to the literature, for the AFM configuration.

Concerning the studied system itself, we found the magnetic structure, layer by layer, of our Fe/Cr/Fe trilayers. The results we obtained improved and added new data to previously published results for these systems [53, 54, 56, 57, 59, 60]. The MMA of the Fe atoms are parallel, and their values are close to the bulk value, being higher for the surface Fe ML and lower for the interface Fe ML. The MMA of the interface Cr atoms are slightly smaller than the bulk value, and almost zero for the middle Cr ML. The Cr MLs couple AFM with each other and with the Fe ones. This related with previous publications about Cr spin-waves, only that those Cr slabs were much thicker than ours. Hence, the Cr MMs follow the profile we would expect from a commensurate SDW, as it would corresponds to the position of our

Cr slab in the Cr phase diagram, except that SDW behaviour is not well defined for such a thin slab. The μ_T of the unit cell was found to follow a linear law.

We also studied the charge distribution through MPA. The most notable feature was that the Fe interface MLs are depleted of electrons, that accumulate in the Cr central ML. There are small population deviations with respect to the isolated atom state in the rest of the MLs, depending on the thickness of the Fe slab. Having all this in account, we found that these deviations fit to a Friedel-like oscillation. Considering this, it was possible to obtain a rough approximation for the m^*_σ in the systems 232, 333, 434, 535 and 636. m^*_σ ranged from 0.1 to 0.5 times m_e, and decreasing with the iron thickness layer. The shape of the oscillation indicated that, in terms of charge distribution, Cr layers could be considered to be acting as a perturbation that will accumulate electrons, perturbation whose influence decays inversely with distance.

The density of states for the atoms of the unit cell, each representing a different ML, was calculated as well. We found that the MLs that rule the behaviour of the properties based on the DOS are the Fe surface, the Fe interface and the Cr interface. The Fe surface ML has always a part of the total resistivity that is due to the $DOS(E_F)$ much larger for spin down electrons than for spin up ones. Finally, we have also managed to draw a qualitative image of one of the factors that contributes to the spin-dependent resistivity in the trilayer interfaces of these systems. We found a short range oscillation of this factor, that can be important in the systems 131 and 333 and 636.

3

2D→3D transition in noble metal clusters: the case of Au_8 clusters.

> *In our language, the word for "true" can also mean "perfect." Likewise,* ***gold*** *is called the "perfect metal." And we have a saying, "He who does not grow old, surely must be made of* ***gold****!"*
> *[Mai Chang]*

3.1 Introduction

Within the current trends of the research in nanoscience, the development and study of structures with a low number of atoms (clusters and nanoparticles) has become a topic of major interest, where different fields of knowledge (Physics, Chemistry, Biomedicine and Engineering) converge. The noble metals: Cu, Ag and Au in particular are the focus of much of this research. The Au clusters, particularly, show a widespread of very interesting properties that are being predicted: interaction and stabilization of DNA[70], relatively high magnetic moments[71, 72], structure-dependent adsorption of amino-acids[73], role in organic catalysis[74–76], properties of molecules where they interact with sulphur[77, 78]. Most of these properties of Au clusters come from the low-dimensionality structures they conform, in contrast with Ag and Cu. It could be thought that Au, Ag and Cu, being isoelectronic, would play an interchangeable role in molecules or atomic aggregates. This is often the truth, especially when it comes to chemical properties. The clusters of these three elements adopt planar structures from one to eight atom size. But, while Ag and Cu 8-atom clusters have been shown to adopt the geometry of a distorted bi-capped octahedron with symmetry D_{2d}[79, 80],(see Fig. 3.1(d)) ab initio calculations have fairly established that the 8-atom gold cluster is shaped like a 4-point

star, a tetra-capped square with symmetry D_{4h} (see Fig. 3.1(a)). This GS was found in calculations with both pseudo-potentials [79–83] and perturbative methods. [84].

Au clusters keep their 2D character up to 12 atoms: in this cluster, the lowest energy structure is already tridimensional. The reason for this late 2D-3D transition in the Au small clusters has attracted considerable attention[79, 80, 82, 85–87]. Before our work, this had been found to happen due to strong d-d orbitals overlap in the 2D structures[79, 80, 86], which makes them energetically competitive with respect to the 3D ones. The Ag and Cu clusters are less electronically dense and there will not be as much d-d overlap, hence the 2D structures will not be energetically favoured. Using a different approach, we show that the d-d overlap actually lowers the energy for 3D Au clusters, and the exchange–correlation (XC) and the electron-electron (e-e) repulsion favours 2D geometries.

Ab initio calculations using the Density Functional Theory (DFT) has been throughout the main tool and playground to explore the geometry of these very small clusters. How can it help to also understand the reasons behind them adopting one structure or another? To understand what favours one certain geometry over others we have to go beyond the comparative analysis of the different isomer energies. We need to study the properties of their electronic structure, such as the shape of the orbitals and the electron density and localization on different structures for the 8-atom neutral clusters of Au and Ag. From this comparison, we will try to deduce why Au clusters tend to arrange in 2D structures.

3.2 Computational Details

We performed all-electron calculations within the frame of DFT. We solved each system using LCGTO-KSDFM[17]. The calculations were carried out with the program DEMON-KS3P5, and the E_{XC} term was solved with the GGA, in the PW91[11] parametrization. It has been shown that the GGA is the approximation that gives the best results for geometry optimizations of these small clusters[88, 89]. The orbital basis set used in our calculations had the contraction pattern (22211/22211/221) for describing the outer 17 electrons: $5p^6 5d^{10} 6s^1$. The core electrons are considered in the model-core potential with the contraction pattern[28] (7:12,9,7,5). The electron density is expanded in the auxiliary basis set (5,5;5,5) in order to avoid the calculation of the N^4 scaling Coulomb repulsion energy, where N is the number of the basis functions[27].

We optimized 9 different geometries that can be seen in Fig. 3.1. We chose these ones from the structures that appear commonly in the literature for metallic clusters of 8 atoms, and then, other regular arrangements, like a cubic one and a FCC one. They all had a first geometry optimization through a Born-Oppenheimer molecular dynamics (BOMD) simulation. After this first approach, the geometry of each cluster was optimized further with a Broyden-Fletcher-Goldfarb-Shanno

algorithm[24]. Also, for each geometry, a search in the magnetic state that yields the energy minimum for zero external magnetic field and T=0, was carried out.

The search of the magnetic minimum state was done between multiplicities 1 and 11, and it was found to be 1 in every case. The chosen convergence criteria were, in atomic units: 10^{-7} for energy, 10^{-6} for electron density and 10^{-4} for the gradient. The d orbital components were treated considering 6 Cartesian d functions: d_{XX}, d_{XY}, d_{XZ}, d_{YY}, d_{YZ}, d_{ZZ}.

3.3 Results and Discussion

3.3.1 Geometry

After performing geometry optimization in all our systems, we found that the energy minimum happens for the tetra-capped square structure. In Fig. 3.1 we report the energies (in eV) of every geometry respect to the minimum configuration. By the time these calculations were done, it was already a well established fact that the 2-D structure of Fig. 3.1(a), a D_{4h} tetra-capped square, was the structural minimum for the 8-atom Au clusters[79, 80, 90]. The second lowest energy structure was found to be a distorted form of the D_{2d} bi-capped octahedron (Fig. 3.1(b)), which was also (when undistorted) the energy minimum of Ag and Cu 8-atom clusters. The third structure was also 2D: a mono-capped hexagon with C_{2v} symmetry (Fig. 3.1(c)). The 4th lowest energy structure is 3-D: a bi-capped octahedron with C_{2v} symmetry that we call (Fig. 3.1(d)). This structure is also extremely distorted.

A remarkable trend is that the 3D structures are distorted. We started the convergence procedure of the calculation with a regular arrangement, and the final result was the distorted structure. This means that in Au 3D 8-atom clusters, the regular structures are unfavoured against their distortions. Attempting to find a geometrical reason behind these distortions, we proceeded to analyse the average distance between first neighbour atoms, and the average coordination number in each cluster. Results are shown in Table 3.1. We have found the following: the first neighbour distance is slightly larger in 3D cluster than in 2D ones (2.68 and 2.62 against 2.56 and 2.61 Å). Also, the distortions in the 3D clusters seem to distort reducing the average coordination number of their atoms: their coordination indices changes from 4.5 in the regular 3D structures to 3.75 and 3. Hence we conclude that geometry optimization of 8-atom clusters tend to produce structures with a low coordination index, and large average distance among atom nuclei. This points toward a relaxation of the nuclear and electron-electron repulsion being energetically favourable, conforming hollow structures. An analogous behaviour has been recently calculated for larger Au clusters (from 20-50 atoms)[91–93], but it has not been reported yet for the smaller ones.

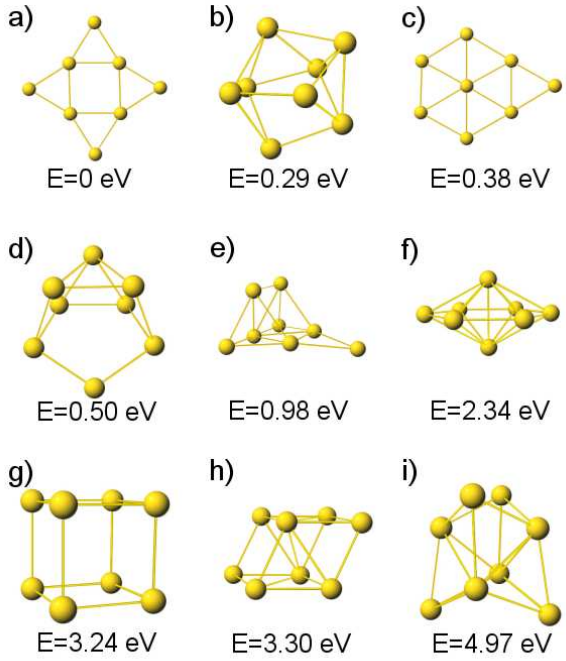

Figure 3.1:
Lowest energy structures of the gold 8-atom cluster according to our calculations are presented. Below each structure, we show the energy difference respect to the fundamental one, the D4h tetra-capped square, in eV. Structures a) and c) are 2D, while the rest are 3D.

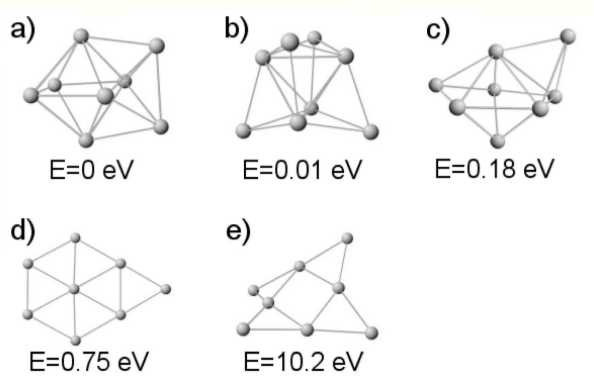

Figure 3.2:
(a)-(c) The 3 lower energy structures of the silver 8-atom cluster according to our calculations are presented. Below each structure, we show the energy difference respect to the fundamental one, the D2d bi-capped octahedron, in eV. 2D structures d) and e) were added for comparison. It is to be noted how the e) structure, originally a D4d tetra-capped square is not stable as a purely bidimensional structure for silver.

Table 3.1:
The value of different structural parameters of the 4 lower energy of the 8-atom Au cluster are given. coord is the average coordination index of each cluster. coord* is the average coordination number of the regular structure the cluster comes from (this parameter is significant for 3D clusters since they are heavily distorted). $\bar{d}$ is the average distance among first neighbours, and $\bar{D}$ is the average distance among all the cluster atoms. Distances are given in Å. Columns (a), (b), (c), (d) correspond to the a), b), c) and d) structures in Fig. 3.1.

	(a)	(b)	(c)	(d)
coord	3.0	3.75	3.5	3.0
coord*	3.0	4.5	3.5	4.5
$\bar{d}$	2.56	2.68	2.61	2.62
$\bar{D}$	3.97	3.29	3.81	3.44

3.3.2 Electronic Structure

In our previous work [38] we found that the structure that minimizes the energy of 8-atom Ag clusters is the bi-capped octahedron (Fig. 3.2(a)), and the second lowest structure is a tetra-capped tetrahedron with T_d symmetry (Fig. 3.2(b)). These coincide with the minimum structures for Cu[80]. These two structures are almost degenerate with a difference of only 0.006 eV between them. The third lowest structure, a capped pentagonal bi-pyramid with C_s symmetry, has a higher energy, 0.182 eV over the fundamental state. The Cu lower energy structures had been reported to be found as well in a narrow energetic margin[79, 80]. In contrast, the differences we found between Au structures were wider: as we see in the Fig. 3.1, the 5 lowest energy structures span over 1 eV.

With the broken down components of the total energy (in Table 3.2), we calculated the differences between the energy terms of each cluster and the same energy component of the lowest energy structure (that is 2D). We only included the energy terms that showed a dependence on the dimensionality of the cluster. The kinetic energy (ΔE_K) component favours 3D structures: they lower the E_K by 37.30 and 38.58 eV respect to the lowest-lying cluster (which is 2D), and the other 2D cluster increases it by 3.26 eV. The kinetic energy is lowered by $d-d$ orbital interaction[82]: tighter-packed 3D clusters will have heavier $d-d$ interaction. In the 2D clusters, the a) structure has a smaller distance between first neighbours than the c) one (see Fig. 3.1 and Table 3.1) so it will have a smaller kinetic energy as well. The Coulomb (ΔE_C) interaction is opposite as the 3D clusters have it raised by 3800 and 2461 eV respect to the lowest-lying one, while the other 2D cluster raises it by only 1008 eV. The exchange-correlation (ΔE_{XC}) term favours 2D too: the increase is 2.06 and 2.74 eV in the 3D clusters, while in the other 2D cluster is reduced by 0.13 eV. Despite this, ΔE_K and ΔE_C differ by several orders of magnitude from the total energy difference respect to the lowest-lying cluster, ΔE_T. The ΔE_{XC} term shows the same bias as the total energy (favouring 2D structure) and is in a

Table 3.2:
We present the energy of each one of the 4 lower energy Au clusters from our calculations, the energy of the 3 lowest-lying structures for Ag and the energy of two 2D structures for Ag according to our calculations. The first column is the name of the structure according to Figs. 3.1 (for Au) and 3.2 (for Ag). Second column is the total energy of the clusters respect to the energy of the lowest-lying one. Following columns are the differences of the kinetic, coulombian and exchange-correlation components of the energy respect to their value for the lowest-lying cluster. Energies are given in eV(*results taken from Ref. [38]).

structure	ΔE_T	ΔE_K	ΔE_C	ΔE_{XC}
Au (a) 2D	0.0	0.0	0.0	0.0
Au (b) 3D	+0.29	-37.30	+3800	+2.06
Au (c) 2D	+0.38	+3.26	+1008	-0.13
Au (d) 3D	+0.50	-38.58	+2461	+2.74
Ag (a) 3D*	0.0	0.0	0.0	0.0
Ag (b) 3D*	+0.01	-7.00	-3462	+0.03
Ag (c) 3D*	+0.18	-1.03	-2522	+0.02
Ag (d) 2D	+0.75	+5.71	-32662	+0.36
Ag (e) 2D	+10.25	+56.71	-150955	+6.78

similar order of magnitude. Hence we conclude it is the E_{XC} term the one that controls the preference small gold cluster have for planar structures.

In Table 3.2 we compare these results with previous results by our research group [38] for 3D silver clusters, plus two 2D silver clusters whose structures are the lowest energy 2D structures for gold; we did this to improve the comparison between Au and Ag clusters. For them, we keep observing the same trends as for Au clusters, regarding to the E_K and E_C. E_{XC} is still the term that decides the minimum structure, but its importance is much lesser than in the Au. For Ag clusters, though, E_{XC} favours 3D structures over 2D ones.

To understand where this comes from, and what it means, we will analyse the electronic localization in the clusters, as electron localization is related to the XC energy (see Appendix A). The electron localization is not an observable, hence it cannot be univocally defined. Because of this, there are available several theoretical methods to quantify it. We adopt Becke and Edgecombe's definition[22], commonly known as ELF. In this definition and within the DFT framework, an increase of the electron delocalization corresponds with a reduction of the E_{XC}, whereas the opposite behaviour is predicted for the E_{XC} if the localization increases. Electrons are delocalized for ELF values around 0.5, and they are localized for ELF values close to 1. ELF values close to 0 means that there are not electrons in that point: if we have large regions with ELF close to 0 within a system, this indicates a high degree of localization in the rest of the system. Taking this in account, we will show the HOMO and the ELF for the systems, in Figs. 3.3 and 3.4 respectively.

As shown in Fig. 3.3a), the HOMO of the (a) structure does not accumulate around any particular atom. Instead, it is almost equivalent for every atom. In Fig. 3.4a), the ELF shows, as expected, two shells of electron localization, one for each

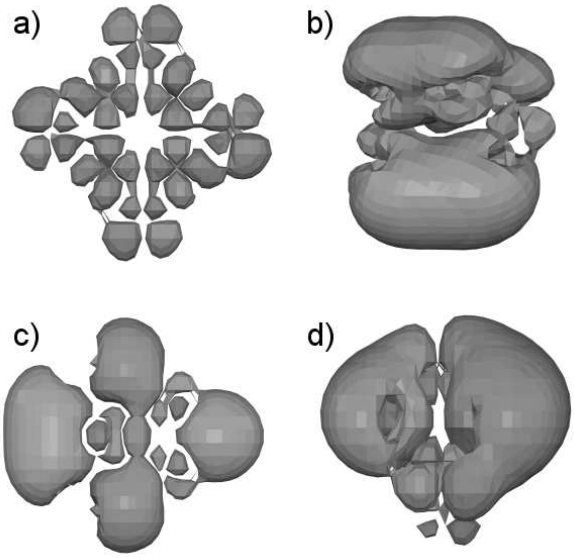

Figure 3.3:
The highest occupied molecular orbital (HOMO) is plotted for the 4 lowest energy structures of the 8-atom Au cluster. a), b) c) and d) are the HOMO of the a), b), c) and d) structures of Fig. 1 respectively. Isomers a) and c) are 2D, while b) and d) are 3D.

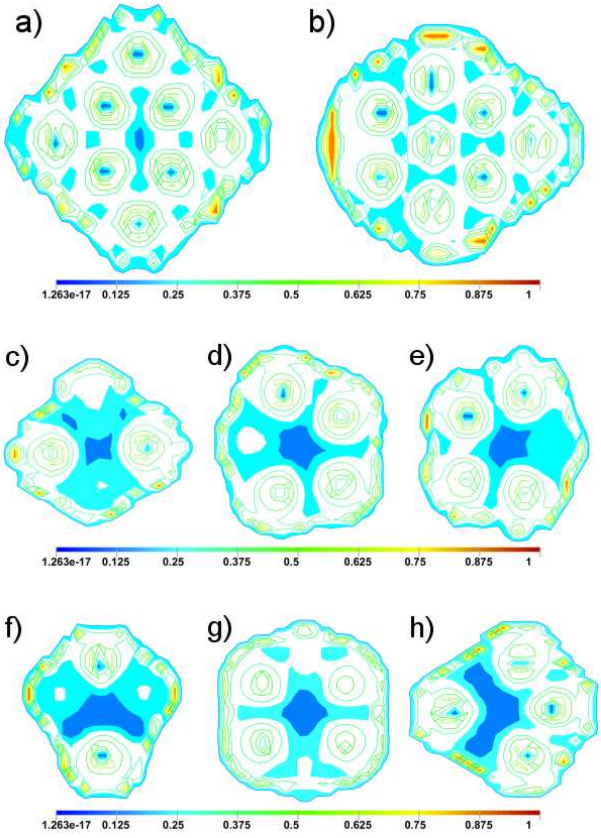

Figure 3.4:
The electron localization function (ELF) is plotted for the 4 lowest energy structures of the 8-atom Au cluster. a) and b) are the ELF on the plane Z of the Fig. 1 a) and c) clusters respectively. It is to be noted that Z is the plane where all the atoms are contained in both these clusters. c), d) and e) are respectively the ELF in the planes X, Y, Z of the Fig. 1 b) structure. f), g) and h) are respectively the ELF in the planes X, Y, Z of Fig. 1 d). We have shaded the area where ELF drops below 0.25 or rises over 0.75, and a darker shade for where ELF drops below 0.125, or rises over 0.875. ELF takes values between 0 and 1.

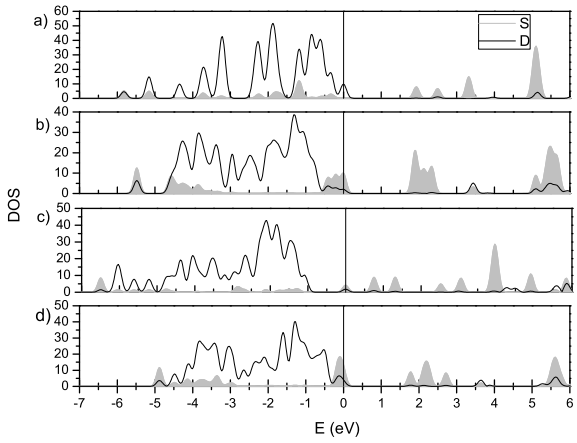

Figure 3.5:
The partial density of states (pDOS) of the s-type and d-type orbitals are plotted for the 4 lowest energy structures of the 8-atom Au cluster. a), b), c) and d) are the pDOS of the a), b), c) and d) structures of Fig. 1, respectively. The origin of energies is placed in the energy of the highest occupied molecular orbital in each case.

atom, another enclosing the whole domain of the cluster. Within the domain of the cluster, we see that the ELF does not drop below 0.25, except for a very small region in the centre. In Fig. 3.3b) the HOMO of the (b) structure shows a degree of bipolarization (and hence, stronger localization). A close inspection of the ELF in Figs. 3.4c), d) and e), reveals that inside the cluster domain shell, there is a relatively large region whose ELF value drops below 0.25. These plots show how the electrons are more delocalized in the 2D structure than in the 3D one, hence explaining why the XC term favours the 2D structure over the 3D ones. The other 2D (HOMO in Fig. 3.3c) and ELF in Fig. 3.4b)) and 3D (HOMO in Fig. 3.3d) and ELF in Figs. 3.4f),g),h)) structures follow the said trends.

The DOS depicted in Fig. 3.5, shows that the s-d hybridization is greater for Au clusters than for Ag ones, due to the s-d orbitals spatially overlapping more greatly in Au (outer orbitals in Au are larger than Ag ones, while interatomic distance with first neighbours is close to the value for Ag clusters). This case is analogous to the findings of Bronbeck et al.[80] for Au and Cu. The analysis of the DOS graphics show a low component of S orbital in the HOMO for the 2D clusters while it is very large for the 3D ones, due to their higher sphericity. This is the origin of the kinetic energy term favouring 3D structures. It is to be noted that the d bands are very narrow in the (a) structure, due to its highly symmetric geometry. This slim width is a lot more obvious when analysing the components of d: d_{zz},d_{xz} and d_{yz} are dominant. Even though the (c) structure is very regular too, we do not see it in the d bands. But splitting it into its components we see that each one of them creates narrow bands. The distorted structures (b) and (d) have a very wide d band instead.

3.4 Conclusions

Is there a relationship between the structural deformations of the 3D clusters with the fact that 2D clusters are energetically much more favoured in Au than in Ag and Cu? From our own and others' works[38, 79], we know that the minimum energy structures for Au and Ag have a very small difference when considering the average distance between nearest neighbours (within 1%), and these distances are sensibly higher for them than for Cu. This reduced size is well known to be due to relativistic effects[82, 94]. This relativistic shortening of the size of the Au clusters increases the classical Coulomb repulsion among the Au nuclei and among the electrons of the cluster, hence favouring structures where the average distance between atoms is larger. The two-dimensional structures have a larger average distance between atoms even if the average distance between first neighbours is smaller, because the coordination number is lower. It has been observed for larger Au clusters (from 20 to 50 atoms) that while they are 3D, their lowest energy structure is not tight-packed like, but instead, they tend to form cage-like structures. We have found that this is the case too even for clusters as small as 8 atoms, considering only their 3D structures. We can observe in the Fig. 3.1 and Table 3.1 that the 3D clusters deform in a way that reduces the coordination number, and create "cavities" in their inside. The apparition of these cavities causes the ELF value to drop in them, hence making the electrons to be more localized in the 3D clusters than in the 2D ones. This higher delocalization of the 2D structures will make the E_{XC} factor to be favourable to them (which, as we have seen, is the decisive energetic factor), stabilizing them as the lowest energy structure. Our findings conflict with past works on this topic who shift the control of the dimensionality to the E_K term[80, 82]. In their studies they find that the E_K favours 2D structures because of the importance of $d-d$ interaction. We have shown that this $d-d$ overlapping is actually more important in the 3D clusters, hence the E_K will be lowered for them. In Ref. [80] the 8-atom Au cluster is studied in comparison with the 8-atom Cu one. While they find the E_{XC} to control the dimensionality of the Cu clusters, they did not retrieve this behaviour for the Au case. We have shown that for Au, and Ag too, the E_{XC} is still the energy term that controls the cluster dimensionality.

4

A case for magnetostriction in very small gold clusters: Au_8

> *-Crystal isn't* ***magnetic****.*
> *-Neither is* ***gold****.*
> *[Prof. Henry Jones Jr. & Mutt Williams]*

4.1 Introduction

The magnetic state of very small metallic clusters is very sensitive to their structure. If we want to have a reliable calculation of their magnetic state we need to perform a very fine geometry optimization. But this is a two-way road: in the same fashion, when we calculate different magnetic states, we find out that their ground state structure can be slightly different. In Au clusters, this precision in the calculation is even more necessary: as we have seen in the previous chapter, Au clusters have many isomers very close in energy to each other, with different magnetic states. This hints the possibility of magnetostriction; under a magnetic field, magnetic states will have their energies changed. If there is a magnetic state that is energetically lowered enough to become the lowest laying one, and it yields a small structural distortion of the ground state geometry, we will have magnetostriction. It is important that this new structure is a deformation of the ground state and not a completely different structure, i.e. it lies in the same structural energy well. If it lies in a different energy well, the structure will not be accessible, as simply changing the magnetic field provides no energy to the cluster to jump over the energy barrier.

Now, the question is, will our ab initio calculations allow us to locate magnetostriction candidates, i.e. clusters whose structure depends on their magnetic state?

4.2 Computational Details

We performed all-electron calculations within the frame of the density functional theory. We solved each system using linear combinations of Gaussian-type orbitals within the Kohn-Sham density functional methodology[17]. The calculations were carried out with the commercial software DEMON2K 1.0.4, and the GGA, with the PBE parametrization, was used to account for the exchange-correlation energy term. We performed our calculation over a total of nine different geometries for their five lowest magnetic states. These nine geometries were obtained through steepest-descent energy minimizations of 5000 random configurations of eight gold atoms with the OPTIM package[95]: The full geometry optimization for these nine geometries was done using a Born-Oppenheimer molecular dynamics simulation. All calculations were at $T = 0K$. Charge and spin distributions on the atoms of the clusters are obtained through a Mulliken population analysis.

4.3 Results and Discussion

After performing a geometry optimization in all of our systems, for the lowest magnetic configurations, we found that the energy minimum of each cluster happened for a total magnetic moment zero, as expected from previous works both on gold and silver for the eight atom structures[76, 79]. Nevertheless, this systematic magnetic study of the eight atom gold clusters revealed that for some symmetries, the structure is spin dependent. We have found this to be the case both for the D_{4h} and the T_d geometries. The case of D_{4h} is particularly important, because, as we have seen in the previous chapter, this cluster is the lowest lying isomer, found to be so in all recent works (including our own). In this case we found that the lowest magnetic moment configurations show the following energies: for multiplicity $m = 1$, the total energy (E_T, in hartrees) is -1087.5919; for $m = 3$, $E_T = -1087.5342$; and for $m = 5, E_T = -1087.4478$. We have also found that, while the clusters with $m = 1$ and $m = 5$ share the D_{4h} structure, the one with $m = 3$ is not stable for that symmetry, and the geometry relaxation converges for a distorted structure, as we can see in Fig. 4.1. These three magnetic configurations have a different charge and spin distribution: for m=1, there are net positive charges in the longer diagonal of the inner square (atoms 2 and 4 in Fig. 4.1) of $\approx 0.21\ e$ (e being the electron charge), while most of the negative charges are in the outer square (atoms 5-8 in Fig. 4.1) with $\approx -0.08\ e$, and in the shorter diagonal of the inner square (atoms 1 and 3 in Fig. 4.1) with $\approx -0.05\ e$. As the total magnetic moment is zero, the spin distribution is not calculated. For $m = 3$, the positive charge localizes in the atoms 1 and 3, with $\approx 0.28\ e$, and the negative charges in the outer square atoms, with $\approx -0.17\ e$. The atoms 2 and 4 have a much smaller charge, $\approx 0.06\ e$. The magnetic moment distribution localizes in the outer square atoms, with $\approx 0.45\ \mu_B$, while the atoms 1 and 3 have $\approx 0.27\ \mu_B$ and 2 and 4 have $\approx -0.16\ \mu_B$. For $m = 5$,

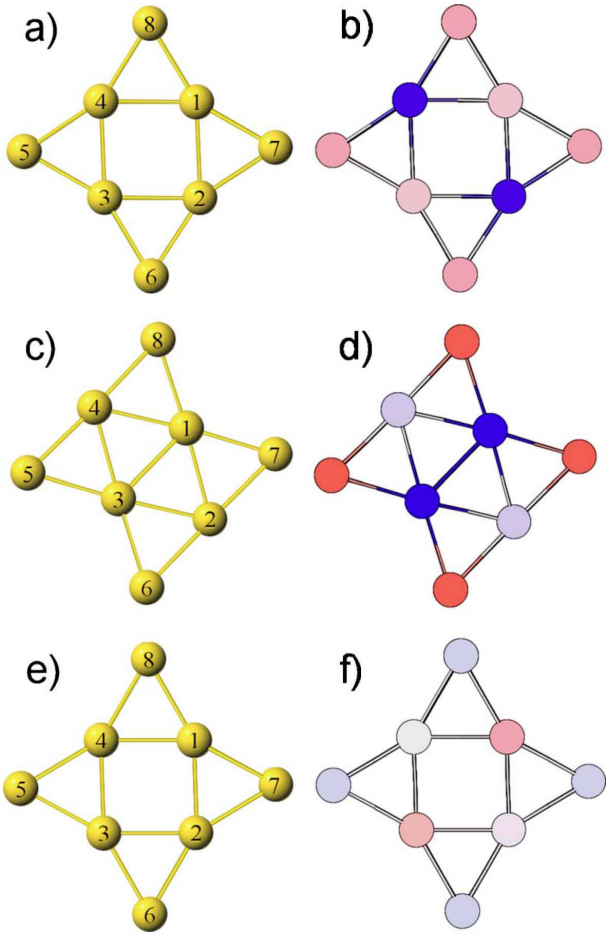

Figure 4.1:
(a), (c), and (e) represent the minimum energy structure of eight-atom Au cluster given as initial structure the one with D_4h symmetry, for multiplicities $m = 1$, $m = 3$, and $m = 5$, respectively. At the right hand side of each one, (b), (d), and (f) show the net charge in their atoms: blue represents positive charge, red represents negative charge, and white represents neutral.

the localized charges are much smaller: atoms 1 and 3 have a net charge between $-0.07\ e$ and $-0.08\ e$, and the 2 and 4, between $0.01\ e$ and $0.02\ e$. The atoms of the outer square have a net charge of $\approx 0.03\ e$. Magnetic moment distribution is fairly even: atoms $1-4$ have their magnetic moment ranging between $0.43\ \mu_B$ and $0.48\ \mu_B$, and the outer square atoms between $0.54\ \mu_B$, and $0.55\ \mu_B$. From this data, we can see that there are very noticeable shifts of the charge location depending on the magnetic configuration. The spin location also changes sharply from located mostly in the corners of the cluster when $m = 3$ to more evenly distributed when $m = 5$. Multiplicities higher than 5 were not considered for this analysis as their energy is much higher than the energy for $m = 1$. The T_d symmetry cluster is also significant because it is the structural minimum of the eight-atom Ag cluster[38]. For this geometry, the lowest energy will also belong to the lowest magnetic moment configuration: for $m = 1$, $E_T = -1087.4093\ E_h$ and for $m = 3$, $E_T = -1087.3479\ E_h$. We can differentiate two regions, for commodity: we will call core to the atoms $3, 4, 7, 8$ from Fig. 4.2, and corners to the atoms 1, 2, 5, 6. For $m = 1$, core atoms

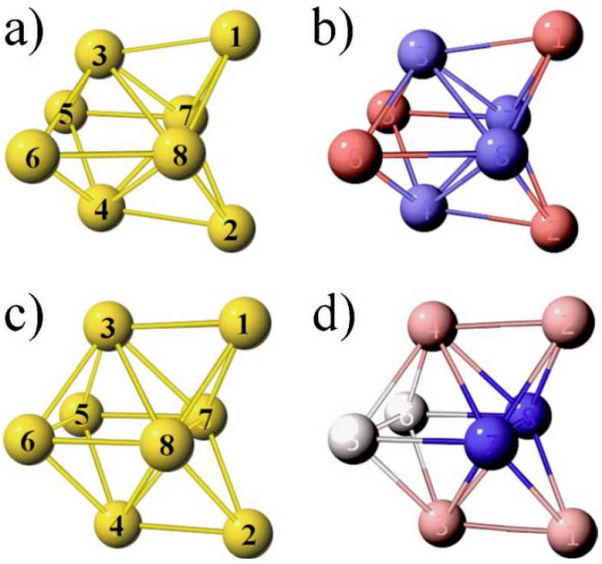

Figure 4.2:
(a) and (c) represent the minimum energy structure of eight-atom Au cluster given as initial structure the one with T_d symmetry,for multiplicities $m = 1$ and $m = 3$, respectively. At the right hand side of each one, (b) and (d) show the net charge in their atoms: blue represents positive charge, red represents negative charge, and white represents neutral.

have a positive charges between 0.40 e and 0.45 e, and the corner atoms negative charges between -0.41 e and -0.43 e. For $m = 3$, the structure distorts, as seen in Fig. 4.2. This distortion transforms the structure into a bicapped octahedron destroying the symmetry among the core atoms and among the corner atoms. Atoms 5 and 6 become almost neutral; 7 and 8 lose electron population and become positive with charges of 0.57 e. Atoms 1, 2 and 3, 4 gain similarity and have negative charges between $-0.26e$ and $-0.28e$. This small distortion has greatly changed the charge places. As for the magnetic configuration, the atoms 1 and 2, which lay outside of the octahedron, have low magnetic moments (0.19 μ_B). The atoms 3 and 4, at the vertices of the octahedron, have a relatively high spin of 0.31 μ_B. The remaining atoms: 5, 6, 7, 8 have magnetic moments between 0.22 μ_B and 0.28 μ_B. For multiplicity $m = 5$, the cluster remains undistorted, and the core and corner atoms retain their symmetry.

4.4 Conclusions

As we have just described, we found in our calculations that there are structural changes in the eight-atom gold clusters originated in their magnetic behaviour, including in the D_{4h} isomer, which is the lowest energy one. These structural changes also produce important changes in the charge and magnetic moment distribution. It has been recently shown that small gold clusters have the capability to adsorb small molecules[96], including important organic ones[70, 73–76]. It has been shown that this adsorption depends greatly on small structural changes[73]. Our findings do not only show how this can be produced: small structural changes produce great shifts in the charge distribution, changing the reaction locus or making it disappear.

We also shown that such changes can be triggered by magnetism: we have found that the Au_8 cluster is a good candidate to exhibit magnetostriction. If this magnetic state change can be induced externally, and this structural change is verified by the experiments, it would have important applications in the biomedicine field, as reactions could be induced/inhibited by magnetic fields.

5

$Au_{n,\ n=3\rightarrow7}$ clusters in a case of biological medium: interaction with the O_2 molecule.

> *It is the **rust** we value, not the **gold**.*
> *[Alexander Pope]*

5.1 Introduction

We know that Au clusters can have a large magnetic moment [71] and present and are likely to show interesting magnetostriction phenomena. This, together with their biochemical catalytic capabilities [74–76], makes them good candidates to operate as vectors in medical applications. But if gold clusters are to be used in a biological medium, it is necessary to know if they are as inert as they are in bulk state, and which conditions might cause them to vary their geometry. A cluster with an adequate catalytic ability and the right magnetostriction, under reasonably low magnetic field values, could be completely useless when the effect of oxidization is taken into account.

In this chapter we are going to explore the utility and accuracy of DFT tools to be able to predict the reactivity between transition metal clusters and oxygen, in particular whether ab initio techniques are useful to identify the locus of the reactions.

Oxidation of small Au clusters has been studied in the past, but it has always focused on oxygen molecules placed in the same plane as the bidimensional clusters[97–100]. We are going to attempt to find if other off-plane positions are possible for these bidimensional Au clusters, and establish if these structures are stable or not. Other points of interest will be: i) finding if the structure of the pure Au cluster is distorted due to the interaction with the O_2 molecule; ii) whether the

HOMO-LUMO gap is a valid method to determine the stability of these clusters. The distortion is relevant because the catalytic properties of Au clusters are highly sensitive to small torsions of their planar surface[73].

5.2 Computational Details

For this calculation, we used the program deMon-KS3p5[17]. As before, we used the PW91 parametrization of the GGA approximation to calculate the XC energy term. We have used the same orbital basis set for the Au atoms as previously: (22211/22211/221). The core electrons were accounted for in the model core potential (7:12,9,7,5), and the auxiliary basis set for the electron density used was (5,5;5,5). For the O atoms, in the same fashion, we have used the basis set (3111/311/1) to describe the 6 outer electrons, while the two 1S electrons are described by the model-core potential (5:6). The auxiliary basis set used was (5,3;5,3).

First we calculated several initial structures for each cluster size: we took the global minimum structure according to current bibliography[79–84, 86, 87]. Then, for each structure we placed one molecule in several positions around the gold cluster, including in-plane, perpendicular and parallel to the plane of the cluster (all gold clusters from 3 to 7 atoms are planar). We did a preliminary geometry optimization through a Born-Oppenheimer molecular dynamics simulation for each configuration. After this first approach, the geometry of each cluster was further optimized with BFGS. Also, we carried out a search in the magnetic state that yields the energy minimum for zero external magnetic field and T=0 for each geometry. The search of the magnetic minimum state has been done between multiplicities 1 and 11. The chosen convergence criteria were, in atomic units: 10^{-7} for energy, 10^{-6} for electron density and 10^{-4} for the gradient.

5.3 Results and Discussion

We found that gold clusters with an even number of atoms adsorb oxygen preferently in the same plane of the cluster, and converge to a spin state S=0. On the other hand, for those with odd number of atoms, the oxygen molecule is adsorbed either parallelly or perpendicularly to the plane of the cluster, converging to S=1/2. The global minima we have obtained for each system after our structure optimization calculations are shown in Fig.5.1, and their energies in Fig.5.2. In Fig.5.1 we notice additionally that the clusters with an odd number of Au atoms show a distorted structure with respect to their non-oxidized counterparts.

In Table 5.1 we show the average bond distance between first neighbour atoms for each cluster, compared to existing bibliography. There is a contraction of the Au-Au bonds of the oxidized clusters with respect to the pure ones. The Au-O bonds are longer for clusters with an odd number of Au atoms than for the ones with an even number. The Mulliken occupation of the Au-O mixed states is also

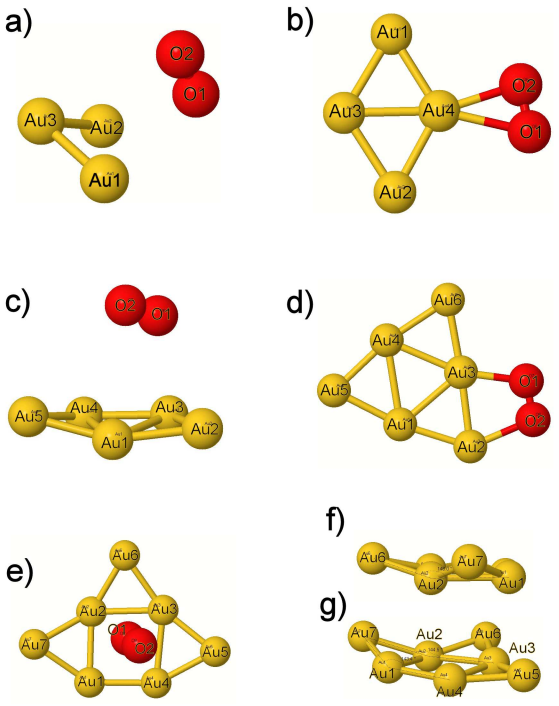

Figure 5.1:
Global minima calculated through geometry optimization for the systems Au_3O_2, Au_4O_2, Au_5O_2, Au_6O_2, Au_7O_2 (a, b, c, d, e, respectively). (f) and (g) are details of the (e) structure from a lateral perspective, instead of top-down, to appreciate the distortion respect to the planar structure.

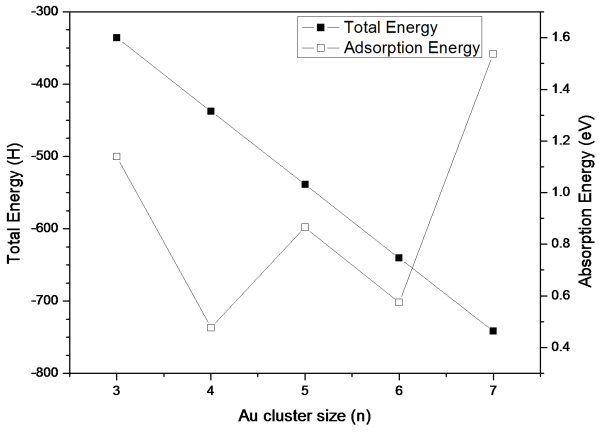

Figure 5.2:
Total energy of the structural global minima for the Au_nO_2, and the absorption energy of the O_2 molecule by the pure Au clusters, against the number of Au atoms in the cluster (n). Total energy is calculated in hartrees (H), and the absorption energy in electronvolts (eV).

Table 5.1:
Average distance between first neighbour atoms ($\bar{D}$) and average Mulliken population of their crossed states (Occ.), for Au_nO_2 clusters. We have averaged the data for the bonds between Au atoms (Au-Au), between Au and O neighbour atoms (Au-O) and between the atoms of the O_2 adsorbed molecule (O-O). The data between brackets in the distance file for Au-Au is the average distance between first neighbour atoms of pure Au_n clusters[79]. The data between brackets in the distance files for Au-O and O-O are the results obtained for the Au_nO_2 by Mills et al.[98]

		Au_3O_2	Au_4O_2	Au_5O_2	Au_6O_2	Au_7O_2
Au–Au	$\bar{D}$	2.46 (2.57)	2.56 (2.69)	2.60 (2.70)	2.59 (2.70)	2.56 (2.71)
	Occ.	0.656	0.430	0.493	0.493	0.414
Au-O	$\bar{D}$	2.93 (2.25)	2.41 (2.13)	3.05 (2.11)	2.26 (2.22)	4.21 (2.21)
	Occ.	0.090	0.109	0.050	0.148	0.005
O-O	$\bar{D}$	1.26 (1.32)	1.32 (1.27)	1.26 (1.36)	1.33 (1.26)	1.25 (1.33)
	Occ.	1.657	0.989	1.690	1.032	1.767

Table 5.2:
Difference in the Mulliken population between the isolated neutral atom and our calculated atoms inside the Au_nO_2 clusters (MPD), and the magnetic moment of each atom of the clusters in atomic units (MM). Individual atoms are labeled according to Fig. 5.1

	Au_3O_2		Au_4O_2		Au_5O_2		Au_6O_2		Au_7O_2	
	MPD	MM	MPD	MM	MPD	MM	MPD	MM	MPD	MM
O1	0.05	0.93	0.23	0.0	-0.01	0.93	0.12	0.0	-0.03	1.00
O2	-0.01	0.98	0.14	0.0	0.05	0.97	0.16	0.0	0.01	1.00
Au1	-0.09	-0.46	-0.10	0.0	0.86	-0.24	0.61	0.0	0.02	-0.13
Au2	-0.08	-0.48	-0.11	0.0	-0.54	-0.10	-1.23	0.0	0.46	0.01
Au3	0.13	0.03	-0.08	0.0	0.17	-0.26	1.20	0.0	0.95	-0.04
Au4			-0.09	0.0	0.09	-0.27	0.22	0.0	0.05	-0.25
Au5					-0.61	-0.04	-0.32	0.0	-0.45	-0.21
Au6							-0.74	0.0	-0.65	-0.04
Au7									-0.37	-0.33

larger for the even ones. From these data we can deduce that in the odd ones there is not an actual chemical bond between the gold and oxygen atoms, but weak bonding. This is likely due to magnetic coupling between the Au cluster and the O_2 molecule, and electrostatic interactions: in Table 5.2 we show the magnetic moments for each atom of the different clusters, and we can see how the magnetic moments of the Au atoms in the odd clusters align antiparallely with the magnetic moments of the O atoms. There is also a small electron defect in average in the Au atoms and a small electron excess in the O atoms, and local charge shifts that reinforce the electrostatic interaction, according to the Mulliken population analysis of the cluster atoms. Respect to the O-O states, they peak for the odd clusters, showing a much higher occupation than the Au-O states. The occupation ratio Au-O/O-O is 0.05 for Au_3O_2, 0.03 for Au_5O_2, and 0.003 for Au_7O_2. This means that the bonding states have a vanishing occupation with the cluster size, for the

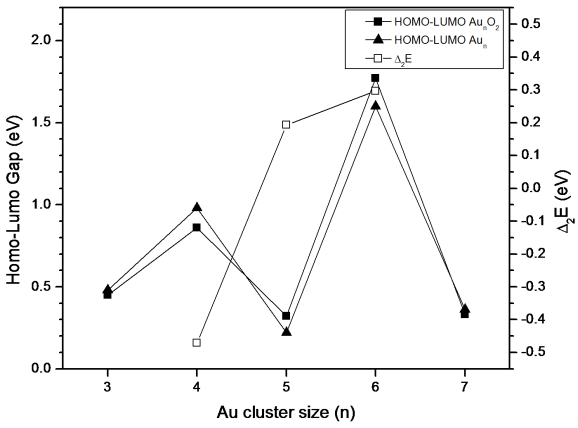

Figure 5.3:
HOMO-LUMO gap for the oxidized (filled squares) and pure (triangles) Au clusters, against the number of Au atoms in the cluster (n), and disproportionation energy ($\Delta_2 E$) for $n = 4$, 5, 6, the only values of n for which it is defined. Both plots are in electronvolts (eV).

odd ones. In the even clusters, the Au-O/O-O occupation ratio is larger, and seems to grow with size in the range of our calculations, being 0.11 for Au_4O_2 and 0.14 for Au_6O_2. The O-O bonds are also longer in the even clusters, while in the odd ones, the length of the bond is closer to the experimental value, 1.21 Å. This reinforces the perception that in the odd clusters the O_2 is an independent molecule, while in the even clusters, the O_2 has become integrated into the cluster structure. The off-plane adsorption of oxygen molecules seems to be stable, though there is not a true bonding state, as we can see in Fig. 5.2: the adsorption energy is higher for the Au_3O_2, Au_5O_2, Au_7O_2 than for Au_4O_2, Au_6O_2. For the odd clusters the adsorption energy is around 1 eV, or higher, while for the even ones, it is around 0.5 eV. To have a better picture of the relative cluster stability, we will use the disproportionation energy, defined as $\Delta_2 E(X_n) = E(X_{n-1}) + E(X_{n+1}) - 2E(X_n)$, where X_n is a cluster with a number of atoms n (in our case, the number of Au atoms, since O is constant), and plotted in Fig. 5.3. If we compare our results with those of Fernández et al.[79], we find that the cluster Au_5O_2 is particularly stable, almost on par with the peak for Au_6O_2, and more stable than Au_4O_2.

Another criterion to measure the cluster stability is often the HOMO-LUMO gap[101] (Fig. 5.3). Nevertheless we find no correlation between the gap and the stability, and our results for the non-oxidized clusters are in agreement with Ref. [79]. The HOMO-LUMO gap for the oxidized clusters shows very small variation with respect to the non oxidized ones, and we cannot find any trend in these variations; this further shows that the gap does not correlate with stability, as we have seen that the presence of the O_2 molecule.

5.4 Conclusions

Our calculations led us to find that the interaction between oxygen molecules and small, bidimensional Au clusters depends on the Au cluster having even or odd

number of atoms. For the even ones, the O_2 bonds in the cluster plane, while for the odd ones, it bonds off-plane. This off-plane interaction does not create an actual chemical bond, but a sum of magnetostatic and electrostatic weak bonds, which provide great stability. Said bonding also distorts the original structure and gives it a slight curvature. For our purposes, this means that ab initio calculations are indeed an effective tool to predict whether a cluster, or any kind of molecule, can be suitable to work in a biotic environment. Au small clusters with an even number of atoms will have their electronic properties changed by the bond with the O_2 molecule, while the ones with an odd amount will remain in the same electronic configuration. Nevertheless the possible catalytic properties will be affected because of their torsion in presence of oxygen.

6

Disagreement between theory and experiment: the case of the magnetism of Bi_4Mn clusters.

> *The metal is an* ***alloy*** *called adamantium. Supposedly indestructible.*
>
> *[Jean Grey]*

6.1 Introduction

As we have seen in the previous chapters, specifically in chapter 3, atoms in bare small clusters can exhibit far larger MMs than when isolated or within crystals[88, 102, 103]. This effect can be enhanced when impurities are added.[71] A question worth answering was whether this effect would be enhanced or muffled when the amount of impurities is as high as to constitute an alloy, and not simply a cluster with impurities. The study of transition metal binary clusters was triggered by the exceptionally high magnetism found in CoRh nanoparticles by Zitoun et al.[104] Since then, a number of magnetically enhanced nanoalloys of ferromagnetic and non-magnetic transition metals have been studied theoretically[105–108] and experimentally[109–111]. Yin et al.[112] found an enhanced magnetism in BiMn clusters for Bi-to-Mn ratios close to 2 in their Stern-Gerlach measurements, which deviated from the trend in other Bi nanoalloys like BiCo, where the magnetic moment had a small dependence with cluster size[109]. In a latter paper, Chen et al.[113] performed extensive density functional theory (DFT) calculations on Bi_nMn_m (n=1-6, m=1-12) clusters to learn their structure and how their magnetism works. While they have found quite a good agreement with the experiment for this series, there are a few large discrepancies between the theoretical value of the magnetic moment and the measured one. The most significant one is the

Bi_4Mn where DFT calculations predict a total MM $\mu_T = 5\ \mu_B$ while the experiment measures 1.6 μ_B. The cause of this discrepancy was not found, although extensive geometric optimizations and an estimation of the orbital contribution to the magnetic moment were performed to solve this problem.

Addressing the reason for these disparities is key. On one hand, the existence of an unadressed question in the literature calls for it to be explained. On the other hand, these problems might point out deficiencies in our approach to ab initio calculations, or in the experimental techniques used. The relevance of DFT calculations comes from the reliability of their predictions, and we need to learn the conditions for which they work, and if they do not work for a case, we need to learn the reasons.

6.2 Computational Details

Our first step was to perform *ab initio* calculations within the framework of the DFT over a large number of different structures of Bi_4Mn, both taken from the literature and created by the authors. We solved each system using the deMon 2003 code[29]. The calculation of the XC energy term was carried out using GGA, in the PBE ansatz[10]. The orbital basis set used in our calculations[27] for Bi and Mn takes the Stuttgart-Dresden effective core potentials RECP—SD[114]. They explicitly consider the outer 15 electrons of the Mn using a relativistic approximation, and the outer 5 ones of the Bi with a quasi-relativistic one. Spin-orbit coupling (SOC) is not considered in either case.

While the SOC term is not negligible in Bi atoms, it has been reported not to have effects in the determination of the geometry of the ground state of their clusters, such as the Bi_4[115]. The electron density is expanded in auxiliary basis sets in order to avoid the calculation of the N^4 scaling Coulomb repulsion energy, where N is the number of the basis functions. The auxiliary basis sets are GEN-A3*[29] for the Bi and A2-DZVP [116] for Mn. The inner electrons of the atoms are represented with a core model, using the Hartwigsen-Goedecker-Hutter pseudopotentials[117].

Each structure was geometrically optimized through a Born-Oppenheimer molecular dynamics simulation. After this first approach, the geometry of each cluster was optimized further with a Broyden-Fletcher-Goldfarb-Shanno algorithm[24]. Consecutively, we carried out a search in the collinear magnetic state that yields the energy minimum for zero external magnetic field and T=0 for each geometry. The calculations were converged using 10^{-7} as the convergence criterion for the self-consistent cycle, and 10^{-4} for the geometry optimization steps. It is worth noting that after this optimization, the initial structures to which we impose the different magnetic states often relax to different final structures, while different initial structures might converge to the same final structure. Hence we obtain a large number of relaxed isomers, all of them local minima in their magnetic state. We focus on the 21 geometries with lower energy, performing single-point calculations for

each isomer, searching for their fundamental magnetic state. The partial charges and magnetic moments for each one of the atoms are known through a mulliken population analysis of the electrons. Next, we perform non-collinear single-point calculations to determine the lowest-energy magnetic state for each one of the 21 isomers. These calculations are performed using a different DFT implementation, the Octopus code[118]. The Octopus calculations consider wavefunctions to be complex spinors and they include the SOC relativistic correction. In the same manner as the collinear calculations, XC energy is approximated through a GGA-PBE functional. As for the grid upon which the KS equations are solved, we have chosen a radius of 4.4 Å and a spacing of 0.1 Å. The mixing scheme is a broyden one, with a mixing factor of 0.02. The convergence factor used was ConvRelDens= 10^{-5}.

6.3 Results and Discussion

6.3.1 Collinear Calculation

In Fig. 6.1, we represent the 21 lowest-energy isomers that we have found in our calculations and in Fig. 6.2, we plot the energies of each of their available magnetic states from 1 to 9 μ_B. Our lowest energy structure is an edge-capped distorted tetrahedron with $\mu_{total} = 5\ \mu_B$. This result agrees with Chen's work[113], and is concurrently in disagreement with the experimental data[112]. In addition, our calculations over the two alternative geometries considered in Ref. [113], a pyramid and a W-like structures, are in good agreement with said work (see Fig. 6.2): the pyramidal structure (isomer 6 in Fig. 6.1) is 0.76 eV higher than the lowest-lying isomer, and the W-like structure (isomer 10 in Fig. 6.1) 1.06 eV higher.

The structures with $\mu_{total} = 5\ \mu_B$ dominate the lowest energy isomers until the 11^{th} one, and from that point on, structures with $\mu_{total} = 3\ \mu_B$ dominate instead until the 18^{th} one. Our 3 highest energy isomers have $\mu_{total} = 1\ \mu_B$, this being the μ_{total} closest to the experimental value of 1.6 μ_B. Studying separately the different isomers for each of these 3 magnetic states, we have found that the energy of clusters set to $\mu_{total} = 3\mu_B$ and $5\mu_B$ grows in average with the ground state energy. On the other hand, if the clusters are kept at $\mu_{total} = 1\mu_B$, we find no such tendency. We have made a rough linear fitting of the energy value of our 21 isomers fixed to these 3 values of μ (see Fig. 6.3), and the value of the lowest energy total magnetic moment in this crude approximation decreases from $5\mu_B$ to $3\mu_B$ to $1\mu_B$ as the isomer ground state energy increases.

Analysing each atom of the nanoalloy separately, most of the magnetic moment comes from the Mn atom, while the Bi ones typically remain close to zero. As we can see in Fig. 6.4a), electrons are shared from the Bi to the Mn, in particular from $6p$ orbitals to $4d$. This charge transfer does not generally enhance magnetism in either element, as the Mn total magnetic moment oscillates between 4 and 5 μ_B for all clusters, without correlation to charge transfers (see Fig. 6.4b). In

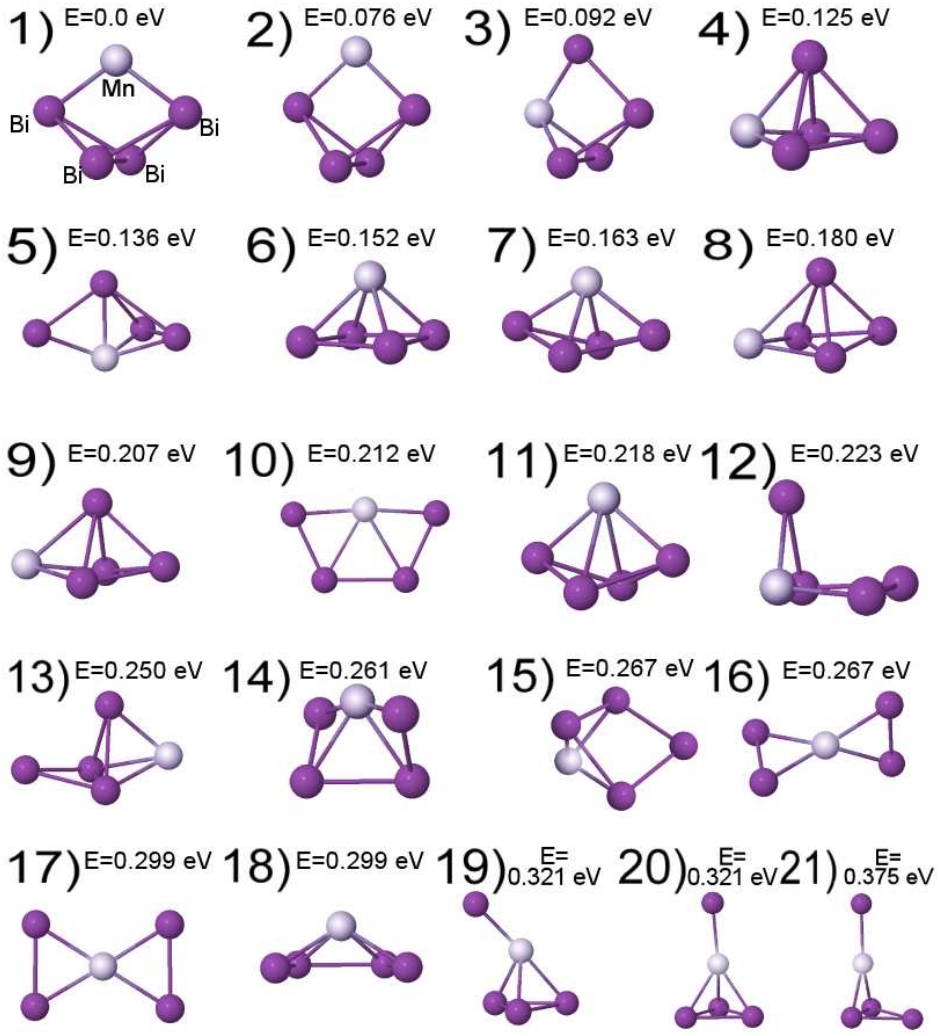

Figure 6.1:
Geometry of the 21 lowest-energy structures for the nanoalloy Bi_4Mn, with their relative energies per atom, in eV.

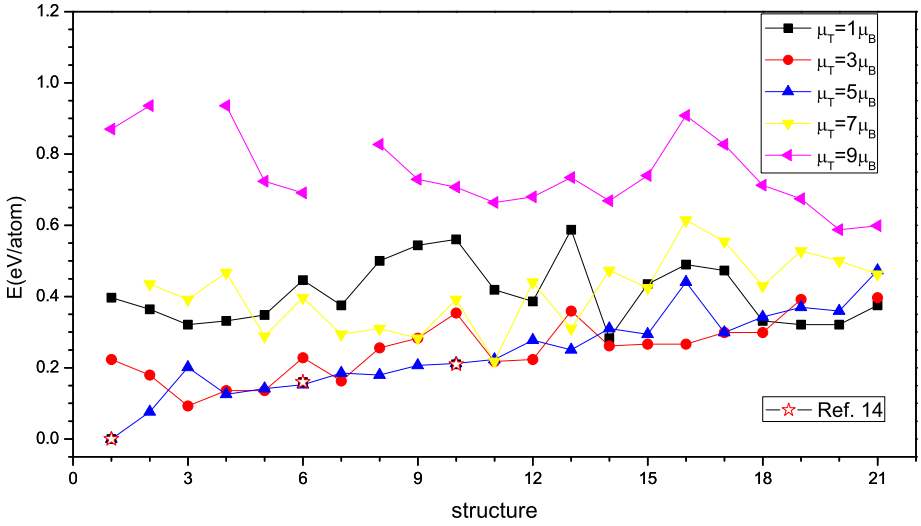

Figure 6.2:
Energy of the 21 structures with lower energy for the magnetic configurations $\mu_{total} = 1, 3, 5, 7, 9\ \mu_B$. The numbers in the x-axis correspond to the structures shown in Fig. 6.1. For the sake of comparison, we have included the relative energies to the lowest-lying isomer for the structures calculated by Chen et al.[113].

the 3 higher energy isomers, however, one of the Bi atoms stands isolated, bound only to the central Mn. This Bi, in addition to transferring $6p$ electrons to the Mn, also receives charge into its $7p$ orbital, greatly increasing its magnetic moment which couples antiparallel with the Mn. This makes the total magnetic moment of the isomer to decrease to 1 μ_B. The lower total magnetic moment state is hence originated in the enhancement of the magnetism of the Bi atoms, whose magnetic moments are either very close to zero or antiparallely aligned to those of the Mn atoms.

In Fig. 6.5 we represent the nuclear repulsion contribution to the total cluster energy. The isomers with smaller nuclear repulsion seem to favour a sextuplet magnetic configuration while structures with higher nuclear repulsion prefer the quadruplet one. There is not enough data on singlet ground states to observe any tendency.

We have not found the lowest energy isomer to have a total magnetic moment close to the experimental value. Instead, the isomers with $\mu_T = 1$ (the ones closest to the experimental value) have a much higher energy than the ground state; hence they could not make up a significant fraction of the experimental sample of Bi_4Mn.

We proceed to test other exchange-correlation functionals to find out if this could be the reason for the discrepancy. In Fig. 6.6, we show the ground states calculated for the lowest-lying isomer for different exchange-correlation (XC) functionals, and we compare them with our results for PBE functional. We performed this calculation for the values of $\mu_T = 1, 3, 5\ \mu_B$. Local functionals exhibit higher energies,

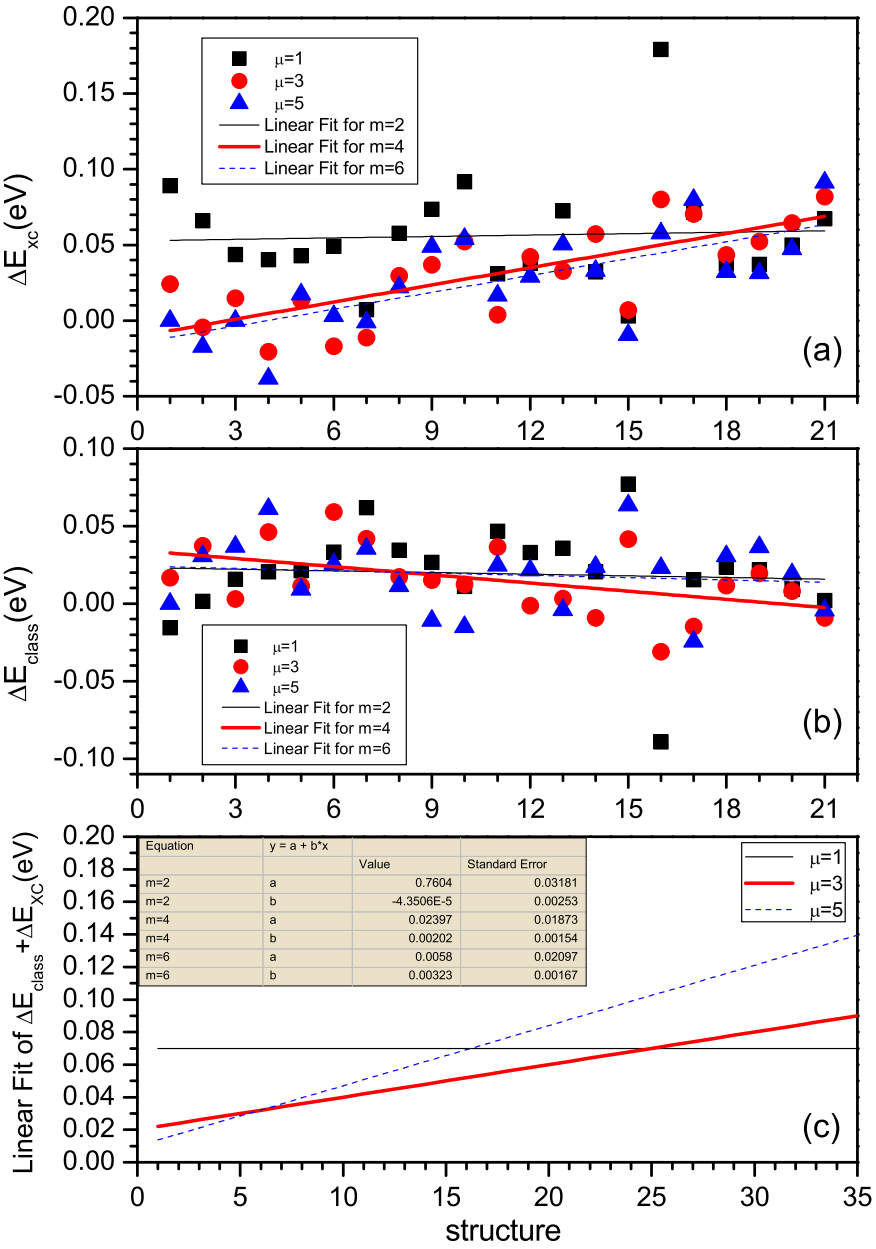

Figure 6.3:
Linear fit of the XC and classical parts of the energy of the 21 lowest energy isomers of Bi_4Mn respect to the ground state, for the values of $\mu_T = 1, 3, 5\mu_B$. (a) plots the XC component and (b) plots the classical one. (c) is the sum of both linear fits in (a) and (b), giving a very rough description of the prevalent magnetic behaviour as the ground state energy grows.

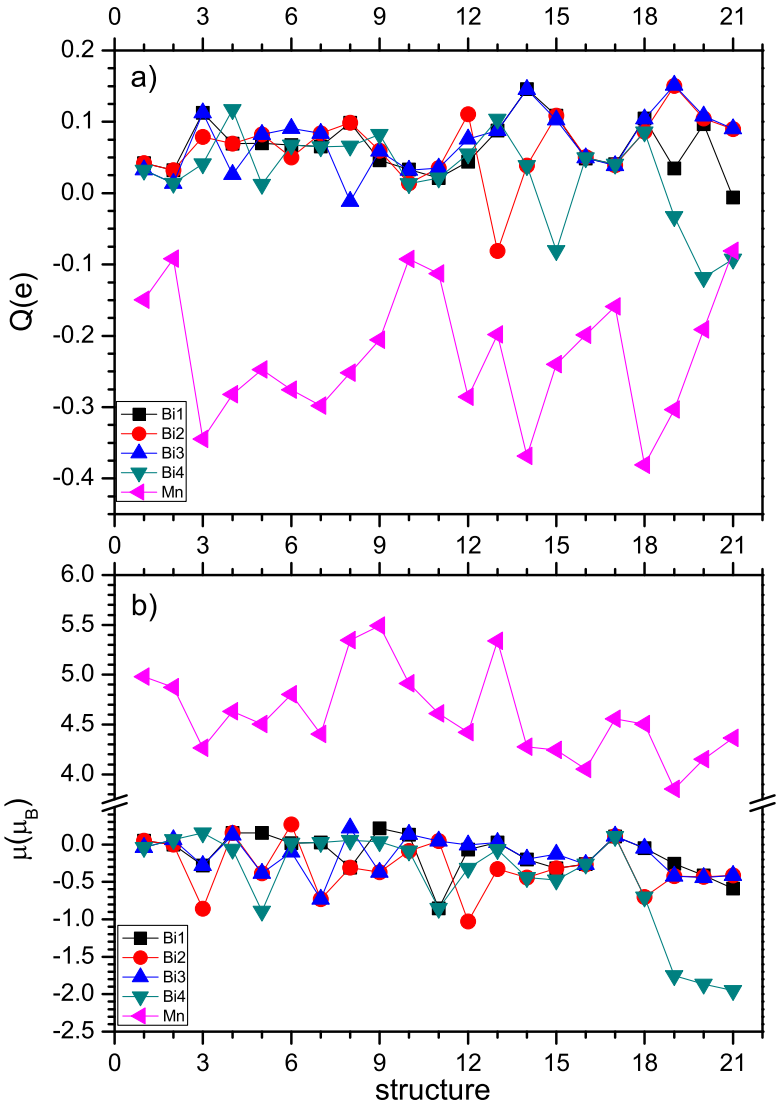

Figure 6.4:
Atomic charges (a) and magnetic moments (b) of each atom in the ground state of each one of the 21 lowest energy isomers of Bi_4Mn.

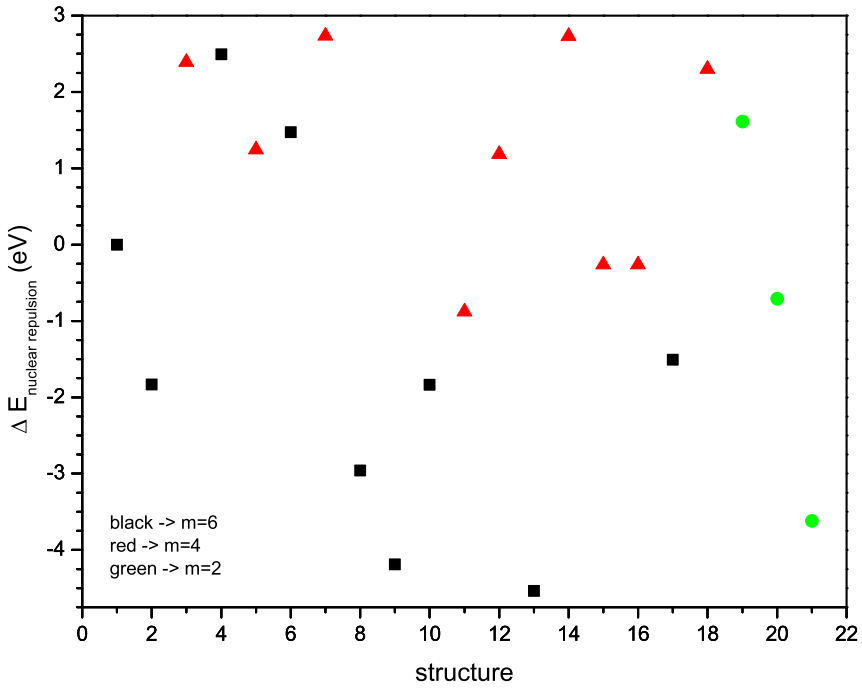

Figure 6.5:
Nuclear repulsion contribution to the total energy of the 21 lowest energy isomers of Bi_4Mn.

but all functionals provide the same energetic ordering of the three magnetic states: $\mu_T = 5\ \mu_B$ as the lowest, 3 μ_B second lower and 1 μ_B third lower. When splitting the energy in XC and classical terms, all the considered functionals keep the same ordering: XC term greatly favours the 3 μ_B and 5 μ_B states, while the bias of the classical term lowering the 1 μ_B state cannot balance it.

The final scenario we can examine with collinear calculations is the possible ionization of the experimental BiMn clusters during their production, or that their structure changes during the ionization in the Stern-Gerlach experiment. This is unlikely because of the low temperature of the process.[126] The results still do not yield any significant reduction of the total magnetic moment, as we can see in Fig. 6.7. The lowest-lying isomers are small deformations of the one for the neutral cluster, and the lowest magnetic configuration is 4 μ_B both for positive and negative ions. The lowest magnetic state of the anions is found for their third lowest-lying isomer, which has $\mu_T = 2\ \mu_B$. Even this result is larger than the experimental value, so it cannot explain the discrepancy.

As a summary, we have found that there are 3 structures of the Bi_4Mn cluster whose $\mu_T = 1\ \mu_B$. The experimental value is 1.6 μ_B, which implies that it is not isomerically pure: there has to be a population mixture of clusters with different

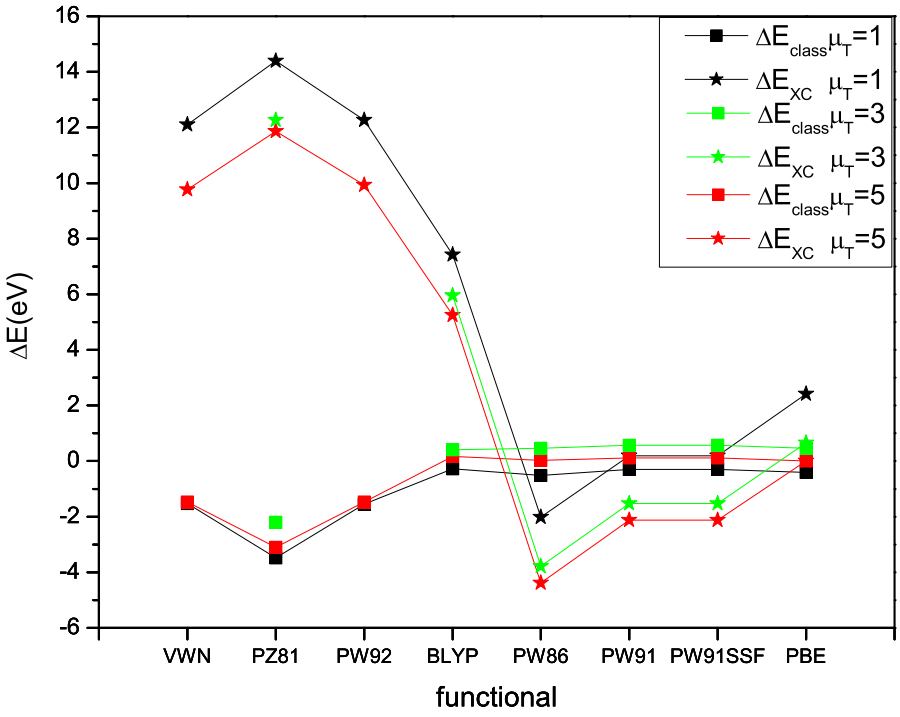

Figure 6.6:
Comparison of the 3 lowest magnetic states of the lowest-lying isomer of Bi_4Mn calculated using different XC functionals. VWN is a Dirac exchange[119] with local VWN correlation[21]. PZ81, Dirac exchange with local PZ81 correlation[120]. PW92, Dirac exchange with local PW92 correlation[121]. BLYP, B88 GGA exchange[122] with LYP GGA correlation[123]. PW86, PW86 GGA exchange[124] with P86 GGA correlation[125]. PW91, PW91 GGA exchange and correlation[11]. PW91SSF, PW91 with full spin scaling function. PBE, PBE GGA exchange and correlation[10].

structures and different μ_T, including 1 μ_B. However these 3 structures are $\approx$ 1.75 eV higher than the lowest-lying one, and there are 18 structures with lower energy than them. Consequently, it is unlikely that the experimental device can produce these isomers in a high enough ratio as to lower the magnetic moment, explaining the experimental value. Except that some other reason, unaccounted for in our calculations, happens to favour their synthesis. Nevertheless, there is another possible explanation for a fractional value of μ_T: that the magnetic moments of the cluster are not aligned collinearly. To explore this possibility, we proceeded to perform non-collinear calculations, where the magnetic moments are not constrained to match a single axis.

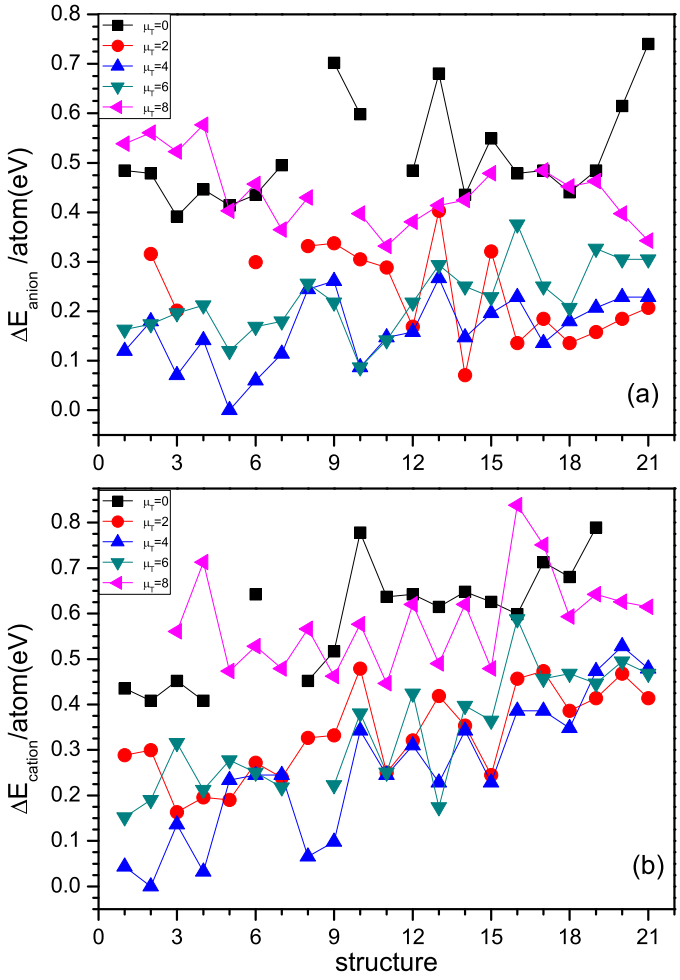

Figure 6.7:
Energy comparison of the 21 structures with lower energy for the magnetic configurations $\mu_T = 0, 2, 4, 6, 8\ \mu_B$ of the negatively (a) and positively (b) charged ions of Bi_4Mn.

6.3.2 Non-Collinear Calculation

The next step is to find out if the discrepancy can be solved with non-collinear calculations, performing them for the 21 lowest-energy structures we found in the collinear ones. In table 6.1 we show the results, with the energy and the components of the total magnetic moment for each geometry. As we can see in Fig. 6.8a), the energy dependence of the different isomers with non-collinear magnetic configuration roughly follows that of the isomers with collinear magnetism. The total magnetic moment (see Fig. 6.8b)) ranges from 3.7 to 6.4 μ_B, with the lowest-lying isomer having $\mu_T = 5.0\ \mu_B$, values which agree with the collinear calculations for the lowest energy clusters, exceeding the experimental result. In the last column

of the Table 6.1 we compare the ratio of the moduli of the total magnetic moment components: M_x and M_y against M_z is very small, specially for the lower energy isomers. We can conclude that the collinear approximation is a good one, which validates the results of our collinear calculations in the previous subsection.

Further analysis of the magnetic components of our isomers yield the orbital magnetic moment: in Fig. 6.8c), we compare the modulus of the orbital magnetic moment with the value for BiMn in bulk, 0.17 μ_B,[127] seeing that the value of the orbital magnetic moment has the same order of magnitude, being small in all cases. Studying the orbital component and comparing it with the total magnetic moment of each isomer, we find that in all cases this contribution is smaller than 10 %, except for the structure 16, where the ratio between the moduli is 14 %. From our results, we conclude that the orbital magnetic moment for these clusters is too small to be a significative factor in the total magnetic moment, so it cannot be the source of the discrepancy between the experimental results and the theoretical calculations. Furthermore, our calculated orbital magnetic moments for each isomer are well within the upper limit estimated by Chen et al., 1.35 μ_B.

6.4 Conclusions

At this point, we felt we had exhausted all the possible scenarios where ab initio calculations could have induced the known discrepancy between the experimental value of the total magnetic moment of the Bi_4Mn cluster and the theoretically calculated one. We had found that three isomers among the 21 most stable actually have a total magnetic moment below the experimental one, but these isomers are too high in energy respect to the lowest-lying one. Furthermore, there were 18 isomers with lower energy, so these three could not make up for a fraction of the population of randomly created Bi_4Mn clusters significant enough to reduce the average total magnetic moment down to the experimental value. We had found that any of the used XC functional approximations does not make the ground state of the lowest-lying isomer have a lower magnetic moment. The analysis of the positive and negative singly-charged ions had also yielded no lowest-energy structure with a magnetic moment close to the experimental one. In fact, none of the ions of the 21 isomers we have considered has a ground state with a magnetic moment lower than the experiment. This should be expected though, as the only lower magnetic state available to ions of Bi_4Mn is a singlet. The possible presence of ions would not help us explain the experiment unless we had found ground states at $\mu_T = 0$ μ_B. From our non-collinear calculation, we rule out other two possible sources of the disagreement: i) the magnetic configuration is collinear to a high degree, even when allowing the individual atomic magnetic moment to arrange freely, and still produces states with high magnetic moment: between 4 and 6.4 μ_B, hence this cannot be the source. ii) The orbital magnetic moment is too low in absolute value compared to the total magnetic moment to produce a significant reduction in it.

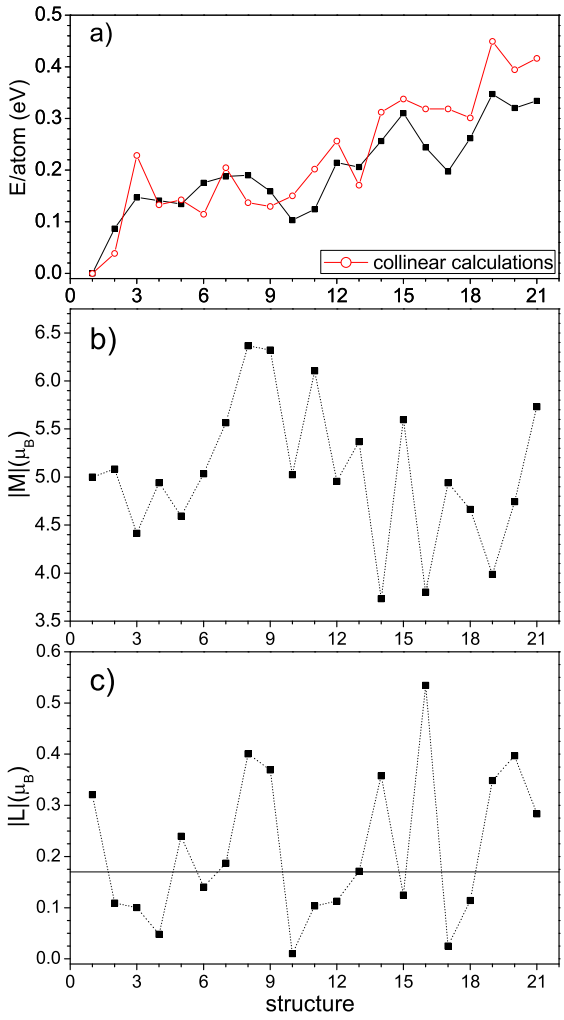

Figure 6.8:
Energy (a), magnetic moments (b) and orbital moments (c) for the 21 lowest-energy isomers of Bi_4Mn found in the non-collinear calculations. In a) we have included the energies of the different isomers from collinear calculations using the Octopus code, for comparison. In c), the horizontal line marks the value of the orbital magnetic moment in bulk BiMn.

struc	$E/_{atom}$	M_x	M_y	M_z	$\|M\|$	$\|L\|$	$\|L\|/_{\|M\|}$	$M_{xy}/_{M_z}$
1	0.000	0.009	-0.006	5.00	5.0	0.321	0.060	0.00
2	0.087	0.001	-0.007	5.08	5.08	0.109	0.02	0.00
3	0.147	-0.070	0.005	4.41	4.41	0.100	0.02	0.02
4	0.141	0.009	0.018	4.94	4.94	0.048	0.01	0.00
5	0.134	-0.186	-0.409	4.57	4.6	0.240	0.05	0.10
6	0.175	-0.039	-0.005	5.03	5.03	0.141	0.03	0.01
7	0.188	-0.634	-0.262	5.52	5.57	0.187	0.03	0.12
8	0.190	-0.243	-0.088	6.36	6.37	0.401	0.06	0.04
9	0.159	-0.028	-0.133	6.32	6.32	0.369	0.06	0.02
10	0.103	-0.022	-0.014	5.02	5.03	0.010	0.002	0.01
11	0.124	0.814	0.096	6.05	6.11	0.104	0.02	0.14
12	0.214	0.039	0.011	4.96	4.96	0.113	0.02	0.01
13	0.206	0.056	-0.218	5.36	5.37	0.171	0.03	0.04
14	0.256	-0.135	-0.128	-3.73	3.73	0.358	0.10	0.05
15	0.310	-0.044	0.097	5.60	5.59	0.125	0.02	0.02
16	0.244	0.229	-0.052	3.80	3.8	0.534	0.14	0.06
17	0.197	0.008	0.046	4.94	4.94	0.025	0.01	0.01
18	0.262	0.345	0.363	4.64	4.66	0.114	0.03	0.11
19	0.347	-0.286	0.392	3.96	3.99	0.349	0.09	0.12
20	0.320	-0.235	-0.038	4.74	4.74	0.397	0.08	0.05
21	0.334	0.798	0.42	5.66	5.73	0.283	0.05	0.16

Table 6.1:
Spread of the results obtained in our non-collinear calculations. First column labels each structure according to their energy ordering in the collinear calculations. Second column units are electronvolts. Columns from 3 to 5 are the Cartesian components of the total magnetic moment and units are μ_B. Column 6 is the modulus of the total magnetic moment and units are μ_B. Column 7 is the modulus of the orbital moment and units are μ_B. Column 8 is the dimensionless ratio of the orbital moment and the total magnetic moment. Column 9 is the dimensionless ratio of the XY plane component of the total magnetic moment and the Z axis component.

All these consistently negative results in our search for a source of the discrepancy in the calculations suggest that said source is not an actual error of the calculations. Furthermore, the possibility that DFT method itself is not reliable to study this cluster is unlikely: the DFT results are in fairly good agreement for almost all the other Bi_mMn_n clusters. Nevertheless arriving at a negative result is not good enough. We want to know if we can rely on ab initio calculations as a tool, not just to describe what is already experimentally known, but to know why the experimental results are the ones they are.

Did the obtained theoretical data give us any clue as to why this disagreement happens that is not explicit?

In Sec. 6.3.1, we suggested that the experimental sample of Bi_4Mn could be composed of a population of different structures. This would be the most obvious

explanation as to why the magnetic moment of the experimental clusters is not integer. Would it possible that some of our structures 19, 20, 21 made up a significant fraction of said sample? We had found no reason why DFT would increase the energy of these structures specifically, so the only other option, for that experimental sample composition to be true, is that a factor in the experiment favoured their production. We thought it was remarkable that the structures 19, 20, 21 were very similar the lowest-lying isomer for Bi_3Mn clusters (a tetrahedron), and could be obtained from them by simply adding an extra Bi atom to the Mn end of the tetrahedron. If Bi_3Mn clusters formed much more quickly in the experimental device than Bi_4Mn ones, it would not be unreasonable to think that the later would form from the former. Bi_3Mn also has a large electrostatic dipole we have calculated to be 2.4 D in the direction that connects the Mn atom with the centre of the triangle formed by the three Bi atoms. This dipolar moment makes them highly stable, and could help a fourth Bi atom to couple to the Mn, instead of breaking up the tetrahedron to form the calculated Bi_4Mn lowest-lying structure. If the process of measurement of mass and magnetic moment of the clusters is fast enough, or if the energy barrier between these mono-capped tetrahedron structure and the lowest laying isomer is high enough, they might not have enough time to relax into the said lowest-lying isomer during their flight in the Stern-Gerlach device (the flight time is estimated in around 10 ms). This would result in some of our structures 19, 20 or 21 making up a large fraction of the measured Bi_4Mn clusters.

To verify this, the path we think it would be most viable is perform an analysis of the optical properties of the experimentally obtained Bi_4Mn clusters to identify their geometry, and see if they match with the isomers theoretically obtained as the lowest energy ones, or instead they match with any of the 19, 20, 21 isomers that actually show a low total magnetic moment. If the later case were true, then we would have to explain why the experimental set-up produces structures that theoretically at $T = 0\ K$ are known not to be the fundamental one.

This explanation is not mere speculation: it shows that the task of the ab initio calculations is not just explaining the experimental results, or predicting results where experiments cannot (yet) be made. When problems arise, ab initio calculations also should be able to lead the experiment in the right direction, to find the solution.

7

Characterization of Au nanoparticles with DDA: when ab initio is not enough.

> *Although* ***gold dust*** *is precious, when it gets in your eyes, it obstructs your vision.*
>
> *[Hsi-Tang]*

7.1 Introduction

As an atomic cluster grows in size, it begins to acquire some bulk-like properties, and lose some of the genuinely nanoscale ones: this realm is the mesoscale. When clusters have as many atoms as to enter the mesoscale, they are commonly called nanoparticles (NPs), albeit this nomenclature is far from standardized. This mixture of properties, together with the possibility to tailor their shape and size have made the noble-metal NPs specially attractive to the applied fields of catalysis, photonics, electronics, sensing, biolabeling and imaging[128, 129]. For example, i) the number, location, and intensity of surface plasmon bands in Au and Ag nanocrystals exhibits a strong correlation with the particle shape[130] which makes these nanoparticles (NPs) useful as therapeutic agents due to surface-plasmon absorption in the near-infrared spectral region[131], or as biosensors when absorption takes place in the visible wavelength range[132]; ii) the presence of sharp edges and tips has been shown to generate an electric-field enhancement,[133] which is important for applications involving metal nanoparticles as sensors; iii) the reactivity and selectivity of metal nanocatalysts depend strongly on the crystallographic planes exposed on the particles surface and, thus, may be tuned by controlling the particle

morphology[134]; iv) additionally, nanoparticle morphology will ultimately determine the way in which nanoparticles can be assembled. Hence, the ability to control the size and shape of noble metal NPs is highly desiderable.

NPs are large enough that there is a relative ease to produce them, and we can rely on many strategies: photochemistry[135], thermochemistry[136], wet-chemistry[137], and biochemistry[138]. By using these different routes, different shaped and size-controlled Au nanostructures, such as nanowires[135], rods[137], nanoplates[135, 138], belts[139], multipods[137], nanocages[140], nanostars[141] and nanocrystals of different geometries (cubes[137], tetrahedra[142], octahedra[139], decahedra[143], icosahedra [144] and bipyramids[145]) have been obtained in recent years. Materials that are so readily available through experimental means are ideal to compare with theoretical calculations. The main drawback is that the study of these systems cannot be realistically performed, nowadays, through ab-initio techniques, not without extreme approximations. In this case we are forced to fall back to a different, but much more commonly used, computational method: computer-assisted modelization. An experimental physics group of USC colleagues has recently found a method to reliably control the shape and size of Au NPs by choosing an appropriate solvent in which the NPs grow[146]. This consisted on a one-pot water-based synthesis route to obtain nanometre-sized uniform gold nanoparticles with decahedral and ultrasmall triangular shapes by reducing Au precursor with citric acid and the commercially available block copolymer Tetronic T904 (from BASF) with high monodispersity.

While characterization of the shape of these NP can be done by means of electron microscopy (see Fig.7.1), a reliable study of the experimental sample size distribution should include the analysis of its optical spectrum. Through our model calculations we can obtain theoretical spectra for each size and geometry of the nanoparticles, and then these spectra are weighed with the measured size distribution to observe if the spectrum fits with the experimental one, and ensure that the measured size distribution is correct.

7.2 Computational Details

The spectra of the Au NPs has been calculated using a DDA[147]. In this approximation the NP is replaced by a cubical array of point dipoles. This approximation was implemented by means of the program DDSCAT[148], which calculates the scattering and absorption of electromagnetic waves by targets with arbitrary geometries, modelizing said targets with the DDA. The electromagnetic scattering problem for an incident periodic wave interacting with this array of point dipoles can be solved this way arbitrarily close to the exact solution. This approximation is legitimately used within a certain NP size range. The discussion of this range, and a deeper discussion on the DDA can be found in the Appendix B.

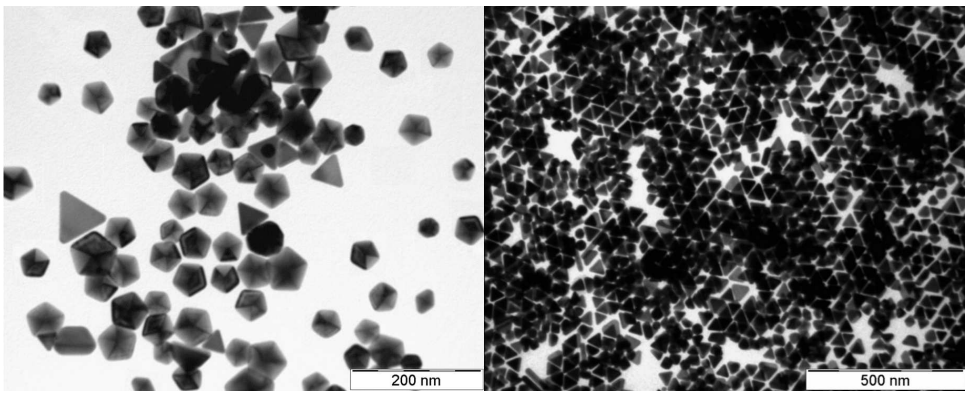

Figure 7.1:
TEM images of: (in the left hand side) Au decahedra synthesized at 80 C in the presence of 0.8 mM T904, 30 mM citric acid 0.5 mM HAuCl4 and 1mM HCl; (in the right hand side) Au triangular nanoplates synthesized at 80 C in the presence of 6 mM T904, 12 mM citric acid 0.5 mM HAuCl4 and 3 mM HCl.

Table 7.1:
First and second columns show the possible values of the b and a dimensions of the decahedral possible NPs, third and fourth columns show the relative population of the possible values for each dimension, and the last column the approximated relative population of each possible NP stemming from those combinations, assuming that these b, a dimensions are independent variables.

b	a	b pop.	a pop.	NP pop.
30	20	51	13	12
30	25	51	52	45
35	25	18	52	15
35	30	18	27	9

For the problem proposed by our colleagues, we considered as targets several sizes of the decahedral and triangular NPs. According to the data we chose particles with the following dimensions: equilateral triangles with side (s) = {40,45,50,55} nm and width (w) = 10 nm; decahedrons with the side of the pentagonal base (b) = {20,25,30,35,40} nm and apex (a) = {20,25,30,35} nm. Without data on the relative frequencies between b and a, we considered the rough approximation that both dimensions are independent of each other, in order to construct our nanoparticles. It is to be noticed that this approximation overestimates the population of the less frequent decahedrons and underestimate the more common ones. With these data, the most frequent decahedral NPs are the ones shown in Table 7.1.

As for the triangle NPs, the experimental populations of the triangles with s = 40,45,50,55nm are 7,25,36,25% respectively. The values of the NP frequencies will be used as weight factors on each of the NPs spectra to obtain the average spectrum for the decahedral NPs.

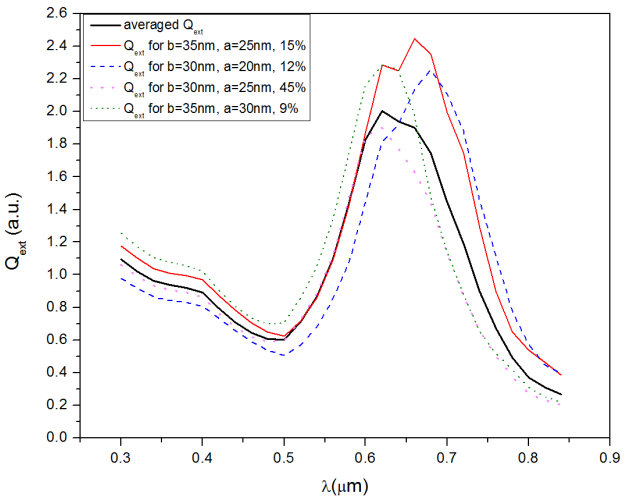

Figure 7.2: Extinction spectra calculated with ddscat for the decahedral NPs with a relative population $\geq 9\%$, in arbitrary units.

The determination of the relative dielectric function of gold respect water has been done using the data of the gold dielectric function from the experimental work of Johnson and Christy[64] and the theoretical approach of Etchegoin et al.[149] The water dielectric function is harder to find because what is commonly used is the data from harmonic oscillator models fitted to the experimental value. As a first approximation we use the function from the work of Dagastine et al.[150] For the triangular NPs, since the solute concentration is quite high, this water dielectric function had to be tuned. We found no data of the water dielectric function for small solute concentrations in the optical spectrum range. Nevertheless we extrapolated data from much lower frequencies to a good accuracy from the results of Gulich et al.[151] and Nörtemann et al.[152] In this approximation, we decrease linearly the real part of the dielectric function as the solute concentration increases, while the imaginary part increases exponentially.

7.3 Results and Discussion

Comparison between the calculated SPR peak (see Fig. 7.2) for the decahedron NPs and the experimental result (Fig. 7.3) shows that the theoretical peak is broader and happens for slightly longer wavelengths.

The red-shift happens because of approximating as pure water as the dielectric medium where the NPs are embedded. The peak broadening is attributed to our overestimation of the population of less common NPs, which are red-shifted respect to the most common ones. Analysing the spectrum of each type of decahedron, we find that the SPR peak is red-shifted the greater the ratio: base side/apex is. Furthermore, when this ratio is much greater than 1, the peak splits in two: when the difference between base side and apex is so large, the absorption spectra will be different whether the light hits the NPs peak-on or edge-on. This splitting of

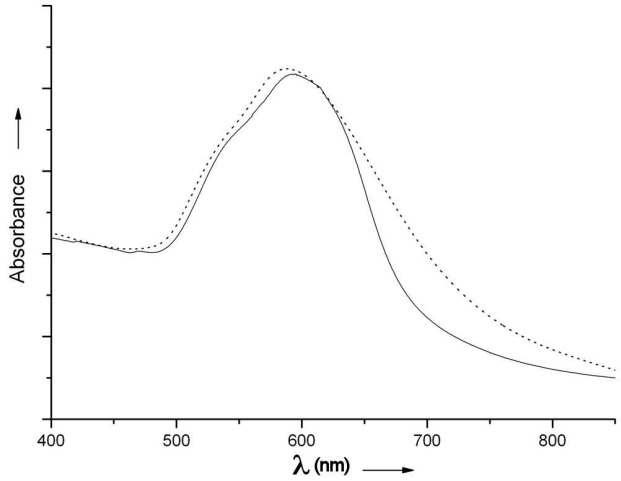

Figure 7.3:
UV-Vis experimental extinction spectrum (in arbitrary units) of Au decahedra (in solid line) compared against the theoretical prediction for said spectra obtained with DDSCAT (in dotted line).

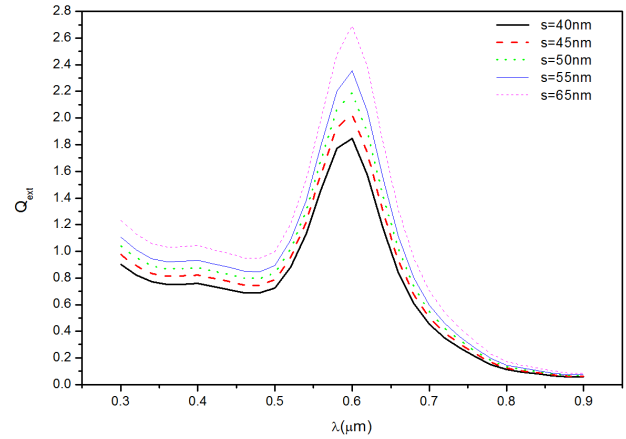

Figure 7.4:
Extinction spectra calculated with ddscat for the four sizes of the triangular NP with a relative population larger than 5%, and for the one with $s = 65$, in arbitrary units. This last value is added for theoretical purposes.

the SPR happens due to having a longitudinal spectra and a transversal spectra different from each other, but neither dimension being negligible respect to each other, and it has already been observed for gold nanorods in different stages of experimental growth procedures[153].

Regarding the triangular nanoplates, because of having a higher concentration of polymer, the red-shift of the theoretical SPR was heavily red-shifted. To solve this we made a strong correction to the water dielectric function to account for the solute, as we have discussed. The SPR after this adjustment (see Fig. 7.4) is in very good agreement with the experimental data, as we can see in Fig. 7.5.

The profile of the spectra does not seem to change as we increase the size of the nanoplates, but on a closer inspection, we notice that as the size increases, there is a very small red-shift of the peak position. To make it apparent, we divided the value of the spectra by the value of the spectrum of the smallest NP, in Fig. 7.6.

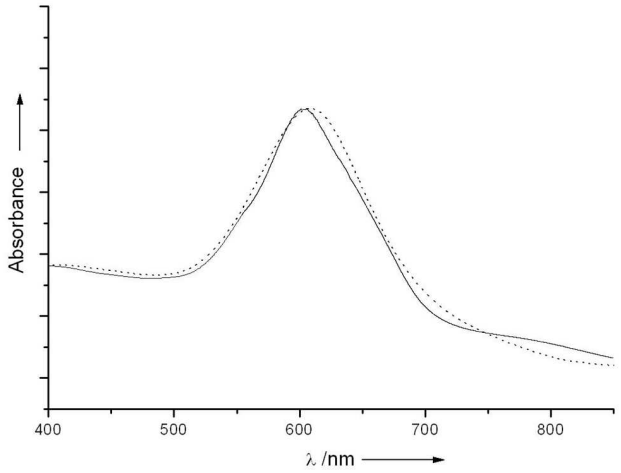

Figure 7.5:
UV-Vis experimental extinction spectrum (in arbitrary units) of Au triangular nanoplates (in solid line) compared against the theoretical prediction for said spectra obtained with DDSCAT (in dotted line).

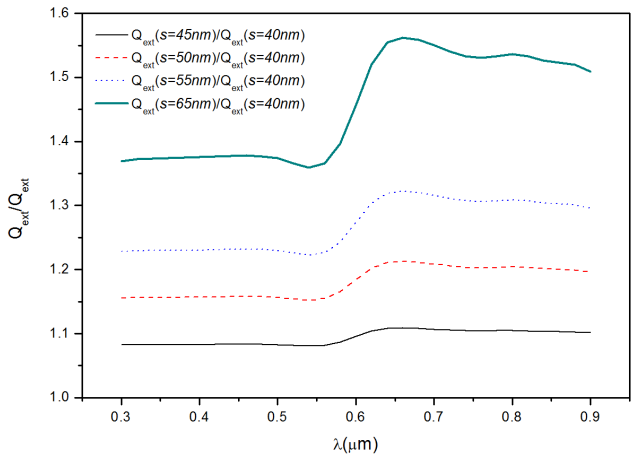

Figure 7.6:
Quotient between the extinction spectrum of the 4 larger triangular nanoplates and the smallest nanoplate considered in the ddscat calculations. NP with $s = 65$ nm is not relevant from a experimental point of view, but is considered for theoretical purposes.

We have considered as well a nanoplate of size $s = 65$ nm. Though this value makes up for very little of the triangular NP population, it will help us see the patterns for growing NPs. Instead of showing a constant value in average, as we would expect if the peak remained in the same position, this quotient plots an approximately step function. The step is higher for larger nanoplates, and its steepest point happens at longer wavelengths. This implies that the SPR has shifted to red frequencies. In Fig. 7.6, we can also appreciate a small peak for $\lambda = 800$ nm. This peak is imperceptible for the smaller nanoplates, but it grows with s and it can be attributed to the quadrupolar mode excitation, which is found also in the experimental spectrum (Fig. 7.5).

7.4 Conclusions

As we have seen, we were able to obtain a very accurate calculation of what the extinction spectra of large samples of both bipyramids and triangular nanoplates should look like. We achieved this by using a very simple modelization of how gold nanoparticles work: simply assuming they can be substituted by a cubic lattice of point dipoles. We have also used rough estimations of the values of dielectric function of the aqueous media the nanoparticles were submerged in. Despite all of this, the results happen to be very accurate compared to the experimentally obtained spectra, which means that this method would have a very high possibility of success if it were relied on as the sole method to characterize experimental nanoparticle samples. DDA is, hence, a very good option to learn the composition of the experimental sample if it cannot be directly observed through microscopy.

8 Conclusions

> *The Quest would have been in vain, even at the bitter end. So let us forgive him! For the Quest is achieved and now all is over. I am glad you are here with me. Here at the end of all things.*
>
> *[Frodo Baggins]*

We started our thesis attempting to find out more about the physical systems we studied, about the properties of thin films and clusters made of transition metals. But beyond that, we also wanted to learn which problems could be solved by means of ab initio techniques on systems where one could consider a small number of atoms (hence a small number of electrons). We wanted to learn what new problems could arise, how to solve them, and how do the ab initio findings mesh with the experimental measurements. So, we are going to consider our concluding remarks under two main groups: methodological and physical.

8.1 Methodology

We have used 3 different versions of the deMon code for the work of this thesis. The bloch-deMon was the first one we used and is an extension to periodic systems, as we have seen in the second chapter. It was a very functional extension, but it had also problems that were owed to its origin in a code designed for clusters and molecules. The main drawback is the inability to handle non-integer values (in μ_B) of the MM per unit cell (which hurts when calculating low MM structures like AFM ones). This can be offset, though, by chosing properly the systems one will chose to calculate, and with the advantages of bloch-deMon: DFT software written to calculate periodic systems often use planewaves as the basis set to construct the

wavefunctions, because they are faster to compute than gaussians; nevertheless, to calculate non-3D systems, it is necessary to repeat the film or the wires periodically to cover all the space, leaving a gap of vacuum as part of the unit cell. This is done because planewaves only work in 3D, but it increases greatly the required computational power. By using gaussians, on the other hand, bloch-deMon can calculate 2D and 1D-symmetric systems in the same way as it does 3D, with the expected reduction in computational requirements. The other 2 versions of the deMon code are simply updated versions of the deMon itself, and they were used for the calculation of our atomic clusters. We started with Au, which was and still is a troublesome atom to calculate: because of the large number of electrons, the relativistic effects are heavy, which contracts the atomic radius (to the point of almost making it as large as the radius of the Ag, the previous atom in the 11th period). Furthermore, the atoms of this period, the noble metals, have a filled outermost f orbital, which makes them unlikely to form chemical bonds.

Only with deMon we managed to find that the 3D isomers of the Au_8 clusters are not completely regular, but they further relax to small distortions that increase their volume. While this could be a dubious result, we consider it is reliable because it fits nicely with the trends found for larger, cage-like, Au clusters, and with the general trend of Au clusters to favour 2D structures. The flexibility of this software allowed us to calculate a number of properties beyond the structure and the magnetism, such as the orbitals and the ELF. It was precisely the analysis of the orbitals and the ELF that gave us the insight on where could lie the actual reason for the preference of Au for 2D structures.

Focusing on the Au clusters, DFT techniques have proven to be good enough to make predictions, and obtain answers in different scenarios like finding the lowest-lying structures of clusters, showing the possible changes that external magnetism can produce in clusters and even the interaction between clusters and molecules. Nevertheless, disagreements between the *Ab initio* predictions and the experimental results happen. How to deal with them?

We found one such case for the Bi_mMn_n alloy clusters: the experiment produced several sizes of clusters whose measured MM was much smaller than the one later found by the calculations, and the most glaring case was the Bi_4Mn. Which was the reason for this inconsistency? What we did was first to explore every single possible failure in the calculations: finding a large sample of local minima geometries that were not too high in energy respect to the lowest-lying isomer, considering different functionals for the E_{XC}, calculating ionized clusters (because the experiment temporarily ionizes them), and finally allowing a non-collinear relaxation of the magnetic state (this non-collinear calculation was performed with a program called Octopus that performs DFT calculations, but solving the KS equations point by point, as a finite element method, instead of using bases). None of these attempts would yield a lowest-lying isomer with the expected magnetic moment. But having exhausted all the possibilities, and thoroughly examined every case, the answer

had to be among the data we had collected, if we just could see it. We knew we had found isomers whose fundamental state had the right magnetic state to explain the experimental data, but they were much higher in energy than the lowest-lying one. Could their experimental production favoured somehow? Examining the other clusters of the Bi_mMn_n family, we realized that the Bi_3Mn had the same shape as these low-magnetic isomers, removing one Bi in a peripheric position. And thus we finally found a possible explanation: if the time it takes to create a Bi_3Mn in the heated Bi+Mn vapour is shorter than what it takes to create Bi_4Mn, then Bi_3Mn can be a preceding step in the formation of Bi_4Mn. So, among the measured Bi_4Mn, there could be a number of them whose structure was not yet well relaxed, and that would be what the experiment measured. Two big "*if*s", but reasonable ones, and that should be tested experimentally.

After handling the problems of small atomic clusters, we were confronted with nanoparticles made up by thousands of atoms, whose dimensions could be measured in tens of nm, slightly less than 2 orders of magnitude more than our clusters. Such large systems cannot be handled through ab initio methods at the current level of computing technology, no matter what drastic approximations we use. So, having in account the information we wanted to calculate about the nanoparticles, their extinction spectra, we looked for a suitable modellization: the DDA. The DDA bears no similarity at all with the *ab initio* methods: it does not make any assumption about the internal structure of the nanoparticle, it does not consider the electrons in the nanoparticle as the agents of the reflection, refraction and absorption of the incoming electromagnetic waves. Instead it substitutes the nanoparticle with a lattice of point dipoles that occupy the same volume, and whose frequency is determined by the dielectric function of the material of which the nanoparticle is made. Despite being such a crude approximation, it produces very accurate results (except for not being able to predict the full height of a small peak due to the quadrupolar modes excitation, due to the dipolar nature of the model), and it helps characterizing experimental samples.

Because of this, it pays to know that each system we study will have different calculation requirements, and because the computational resources we have access to are not infinite, it pays to always consider if an *ab initio* calculation is the most suitable for our goal.

8.2 Physics of Ultrathin Films and Clusters

Regarding our findings on the physical systems we studied:

- The Fe/Cr/Fe trilayers have shown interesting phenomena that, as usual in multilayers, happen in the interface. In this case, the interface Fe atoms become depleted of electrons in favour of the central Cr MLs. This acts as a perturbation that creates Friedel-like oscillations in the MPA of the rest of Fe

atoms. Quite interestingly, we can estimate a value of the electron m^*, even though the concept of effective mass is not well defined for 2D systems. This m^* shows a decline as the Fe slab thickness increases, going from 0.5 to 0.2 m_e.

- Au_8 clusters are interesting for several reasons. First, their ground state structures do not undergo the 2D-3D transition that the other noble metal clusters (Cu and Ag) do when increasing the cluster size past 7 atoms; instead they experience this transition when they reach 12 atoms. While it was known that the final reason was the relativistic effects that Au electrons suffer, the mechanism was not clear in the literature. We found that the higher electron density in Au clusters than in Ag and Cu strains the 3D structures, distorting them to increase their volume-to-no. of atoms ratio. This distortion produces a higher localization in 3D isomers, which makes them less energetically favoured by the E_{XC} term, which is found to control de dimensionality of the structures.

- Au_8 also have their structures dependant on the magnetic state. We have found that when forced to have higher magnetic state than the lowest one (which is also the magnetic ground state), lowest-lying Au_8 isomer geometry changes slightly, with its symmetry switching from D_{4h} to C_{2v}. Also, the lowest energy 3D isomer at a higher magnetic state stops being distorted and regains the D_{2d} symmetry. If we could, through external magnetic fields, change the magnetic state of these clusters, we would be able to regulate the properties that depend on the geometry (such as chemical activity with organic molecules, as literature shows for other sizes of Au clusters).

- Au_n clusters from 3 to 7 show a chemical reactivity with oxigen that depends on whether they have an even or odd number of atoms. For the even ones, the O_2 bonds in the cluster plane, while for the odd ones, the oxygen molecule "sits" in a non-bonding state off-plane, relatively far from the cluster.

- In the case of Bi_4Mn there was a disagreement about the value of the total MM of the cluster between the experimental measurement (1.6 μ_B) and the theoretical calculations (5 μ_B). The experimental MM was not an integer value, what meant that the experimental sample could not be isomerically pure, and it would have to be made up with, at the very least, a majority of isomers whose MM was 1 μ_B and a minority with higher values like 3, 5, 7... μ_B. As we said in the previous section, after examining every way the calculations could be wrong, or calculating the wrong thing, we found nothing. Instead, we found 3 isomers whose energy was much higher than the lowest-lying one, but whose MM was 1 μ_B, as we needed, to make up the majority of the experimental sample. Also, we found that maybe it was too much of a coincidence that their structure was very similar to the lowest-lying structure of the Bi_3Mn clusters. So if during the experimental process, Bi_3Mn clusters

formed first and then Bi_4Mn ones would form from them by adding an atom of Bi to its Mn vertex (which would be favoured by the dipolar moment of the Bi_3Mn), we would be able to explain the experimental result. As we said, this possibility needs to be examined by the experimentalists.

A

The Electron Localization Function as a measurement of Electron Correlation and Exchange

As we have said in our thesis, the Electron Localization Function is only one of the possible definitions of the electron localization. Intuitively, it is natural that electron localization should be linked to the electronic effects of correlation and exchange: the electronic exchange stems from the fact that they are identical particles and they can exchange places with their neighbours in different quantum states without having any effect on the properties of the system, which implies a degree of delocalization; on the other hand the correlation effects should be greater for regions where the electrons can easily find close neighbours, which implies they are spatially localized. This is what the ELF represents, to a good degree: it is a distribution function of the probability of finding another electron respect to one electron taken as reference. Nevertheless, if we want to use the ELF to justify the results of our calculations, we need to find a formal link between ELF and E_{XC}.

From the original Becke and Edgecombes definition of ELF[22] we have that, for open-shell atomic systems:

$$ELF = \frac{1}{1+\chi} \tag{A.1}$$

with

$$\chi = \frac{\tau_\sigma - \frac{1}{4}\frac{(\nabla\rho_\sigma)^2}{\rho_\sigma}}{2^{\frac{5}{3}} C_F \rho_\sigma^{\frac{5}{3}}} \tag{A.2}$$

where τ_σ is the kinetic energy density for the σ-spin, ρ_σ is the electron density for the σ-spin and C_F is the Fermi constant, as in defined by Kohout&Savin[154]. For closed-shell atoms: $\tau_\sigma = \frac{1}{2}\tau = \frac{1}{2}\sum_i^n |\nabla\Psi_i|^2$

Using the virial theorem for the $E_{XC}[\rho]$ and the kinetic energy $T_S[\rho]$ functionals from Levy&Perdew[155]:

$$E_X[\rho] = -\int \rho(\vec{r})\, \vec{r}\nabla \left(\frac{\partial E_X}{\partial \rho}\right) \tag{A.3}$$

$$T_S[\rho] = -\frac{1}{2}\int \rho(\vec{r})\, \vec{r}\nabla \left(\frac{\partial T_S}{\partial \rho}\right) \tag{A.4}$$

Using Fuentealba's approximation[156]:

$$T_S[\rho] = -\frac{1}{2}E_X[\rho] - \frac{1}{2}\int \rho(\vec{r})\, \vec{r}\nabla\phi(\vec{r})\, d^3r - \frac{1}{2}T_C[\rho] \tag{A.5}$$

where:

$$\phi(\vec{r}) = \frac{Z}{r} - \int \frac{\rho(\vec{r})}{\vec{r}-\vec{r\prime}} d^3\vec{r\prime} \tag{A.6}$$

and T_C is the kinetic part of the correlation energy.

Since $E_{XC}[\rho] = E_X[\rho] + E_C[\rho]$, and having in account that $E_X[\rho] \gg E_C[\rho]$, and from Ref. [155]: $T_C = -E_C$, T_S can be approximated as:

$$T_S[\rho] \approx -\frac{1}{2}E_X[\rho] - \frac{1}{2}\int \rho(\vec{r})\, \vec{r}\nabla\phi(\vec{r})\, d^3r \tag{A.7}$$

By definition:

$$T_S[\rho] = \int t_S(\rho)\, d^3r \tag{A.8}$$

and

$$T_S[\rho] = -\frac{1}{2}\int \nabla_r^2 \gamma_S(r, r\prime)\big|_{r\prime=r}\, d^3r \tag{A.9}$$

where $\gamma_S(r, r\prime)$ is the first-order reduced density matrix.

From this, as seen in another paper by Fuentealba[157], we have:

$$t_S[\rho] = \frac{1}{2}\sum_{i=1}^{n} |\nabla\Psi_i(r\prime)|^2 - \frac{1}{4}\nabla^2\rho(r) \tag{A.10}$$

hence

$$\tau_\sigma = \frac{1}{2}\sum_{i=1}^{n} |\nabla\Psi_i(r\prime)|^2 = -\frac{1}{2}e_X - \frac{1}{2}\rho(r)\, \vec{r}\nabla\phi(r) + \frac{1}{4}\nabla^2\rho(r) \tag{A.11}$$

So, ELF approximated form is:

$$ELF \approx \left(1 + \frac{-\frac{1}{2}e_X - \frac{1}{2}\rho(r)\, \vec{r}\nabla\phi(r) + \frac{1}{4}\nabla^2\rho(r) - \frac{1}{4}\frac{(\nabla\rho_\sigma{}^2)}{\rho_\sigma}}{2^{\frac{5}{3}}C_F\rho_\sigma^{\frac{5}{3}}}\right)^{-1} \tag{A.12}$$

expression from which we take the dependence between E_{XC} and localization: higher localization corresponds with a less relevant contribution of the E_{XC} to the total energy.

B The Discrete Dipole Approximation

B.1 Introduction

The discrete dipole approximation (DDA) is one of the most common methods used to calculate the scattering and absorption of electromagnetic waves by small particles or arrangements of them. This is done by means of substituting the scatterer particle, whichever its geometry, with a lattice of point dipoles in its place and their polarization is what will give the scattering properties of the NP. To calculate the polarizations, we have these dipoles interact with the electromagnetic wave and with each other, situation that can be solved with a system of linear equations, obtaining each dipole polarization.

The first approach to the DDA was done in 1964, where it was used to study the optical properties of molecular aggregates[158, 159]; and then in 1973 it was improved to account for retardation effects, in the study of light scattering by interstellar dust grains[160]. The DDA as such was further developed, formalized by Draine and co-workers[147, 161–163] and eventually implemented into the publicly available program DDSCAT[148].

B.2 The Method

The explanation of how DDA works has a double focus: the point dipoles and the scattering problem. The point dipoles will be arranged in a periodic lattice. This is not a necessary condition for DDA, but it is for the use fast Fourier transform (FFT) methods, which greatly accelerate the calculations for large numbers of dipoles (amounts of dipoles much larger than $\sim 10^4$ are not readily computable without FFT). To generate our lattice we create first a trial one defined by the lattice spacing d and the coordinates (x_0, y_0, z_0) of the lattice point nearest the origin. The value of d has to be large enough as not to create too many dipoles that becomes computationally unmanageable, and small enough that the shape of the

particle we want to simulate is well defined. Then we define the volume V that the lattice will occupy. After the lattice is created with the set of point dipoles $j = 1, ..., N$, we rescale d to $d = (V/N)$. The point dipole lattice will now have both the volume and geometry of the particle we want to modelize, and each dipole j will have polarizability a_j.

To calculate the polarizabilities one of the most common approaches is to use the Clausius-Mossotti polarizability $\alpha_j^{CM} = \frac{3d^3}{4\pi}\frac{\epsilon_j - 1}{\epsilon_j + 2}$ where ϵ_j is the dielectric function of the target material at location $\mathbf{r}_j$[160]. This formula gives the exact result for infinite cubic lattices in the long wavelength approximation ($kd \to 0$). Anyhow in a realistic setting, it has been shown that there should be a correction term on $O[(kd)^3]$. This correction accounts for the lattice dispersion relation (LDR) between the polarizability $\alpha(\omega)$ of an infinite lattice of point dipoles and a continuum of refractive index $m(\omega)$. $\alpha^{LDR} \approx \frac{\alpha^{CM}}{1+(\frac{\alpha^{CM}}{d^3})}[(b_1 + m^2 b_2 + m^2 b_3 S)(kd)^2 - \frac{2}{3}i(kd)^3]$

$$b_1 = -1.891531 \qquad b_2 = 0.1648469 \tag{B.1}$$

$$b_3 = -1.7700004 \quad S \equiv \sum_{j=1}^{3}(\hat{a}_j \hat{e}_j)^2 \tag{B.2}$$

where $\hat{a}$ and $\hat{e}$ are unit vectors defining the incident direction and the polarization state.

The scattering problem must be solved for the target lattice of point dipoles ($j = 1, ..., N$) with polarizabilities α_j, located at positions $\mathbf{r}_j$. Each dipole has a polarization $\mathbf{P}_j = \alpha \mathbf{E}_j$, where $\mathbf{E}_j$ is the electric field at $\mathbf{r}$ that is due to the incident wave $\mathbf{E}_{inc,j} = \mathbf{E}_0 exp(i\mathbf{k}\mathbf{r}_j - i\omega t)$ plus the contribution of each of the other N - 1 dipoles: $E_j = E_{inc,j} - \sum_{k \neq j} A_{jk} P_k$ where $-\mathbf{A}_{jk}\mathbf{P}_k$ is the electric field at $\mathbf{r}_j$ that is due to dipole $\mathbf{P}_k$ at location $\mathbf{r}_k$, including retardation effects. Each element $\mathbf{A}_{jk}$ is a 3×3 matrix: $\mathbf{A}_{jk} = \frac{e^{ikr_{jk}}}{r_{jk}} x \left[k^2(\hat{r}_j k \hat{r}_j k - \mathbf{1}_3) + \frac{ikr_{jk}-1}{r_{jk}^2}(3\hat{r}_j k \hat{r}_j k - \mathbf{1}_3)\right], j \neq k$ where $k \equiv \omega/c, r_{jk} \equiv |\mathbf{r}_j - \mathbf{r}_k|, \hat{r}_{jk} \equiv (\mathbf{r}_j - \mathbf{r}_k)/r_{jk}$, and $\mathbf{1}_3$ is the 3×3 identity matrix. Defining $\mathbf{A}_{jj} \equiv a_j^{-1}$ reduces the scattering problem to finding the polarizations $\mathbf{P}_j$ that satisfy a system of $3N$ complex linear equations:

$$\sum_{k=1}^{N} \mathbf{A}_{jk}\mathbf{P}k = \mathbf{E}_{inc,j} \tag{B.3}$$

Once the previous equation has been solved for the unknown polarizations $\mathbf{P}_j$, the extinction and absorption cross sections C_{ext} and C_{abs} may be evaluated[161]:

$$C_{ext} = \frac{4\pi k}{|\mathbf{E}_0|^2} \sum_{j=1}^{N} Im(\mathbf{E}_{inc,j} * \cdot \mathbf{P}_j) \tag{B.4}$$

$$C_{abs} = \frac{4\pi k}{|\mathbf{E}_0|^2} \sum_{j=1}^{N} \left\{ Im[\mathbf{P}_j \cdot (\alpha_j^{-1}) * \mathbf{P}_j *] - \frac{2}{3}k^3 |\mathbf{P}_j|^2 \right\} \tag{B.5}$$

The scattering cross section $C_{sca} = C_{ext} - C_{abs}$. Differential scattering cross sections may also be directly evaluated once the P_j are known[161]. In the far field the scattered electric field is given by: $E_{sca} = \frac{k^2 e^{ikr}}{r} \sum_{j=1}^{N} e(ik\hat{r} \cdot \mathbf{r}_j)(\hat{r}\hat{r} - \mathbf{1}_3)\mathbf{P}_j$

The system of equation B.3 for each polarization j is solved iteratively using the complex-conjugate gradient method[161], which involves primarily matrix-vector $\mathbf{A} \cdot \mathbf{v}$ multiplications. Due to the structure of the matrix $\mathbf{A}$, it has been shown[164] that it can be handled by the FFT method. Its only drawback is that it requires 3D computations over $8N_xN_yN_z$ points, where $N_xN_yN_z$ is the number of sites in a rectangular region of the lattice containing all the N occupied lattice sites. This means that structures with large vacuum regions inside the dipole lattice may cause the FFT method to lose some of their advantage over conventional techniques for evaluating $\mathbf{A} \cdot \mathbf{v}$, since $N_xN_yN_z$ may be much larger than the actual number of dipoles N.

B.3 Validity Criteria

There are two obvious criteria for validity of the DDA: (1) $|m|kd \lesssim 1$ (so that the lattice spacing d is small compared with the wavelength of a plane wave in the target material), and (2) d must be small enough (N must be large enough) to describe the target shape satisfactorily. Define the effective radius a_{eff} of a target of volume V by $a_{eff} \equiv (3V/4\pi)^{1/3}$. The first criterion is then equivalent to:

$$N > \frac{4\pi}{3}|m|^3(k \cdot a_{eff})^3 \tag{B.6}$$

Thus targets with large values of $|m|$ or scattering problems with large values of ka_{eff} will require that large numbers of dipoles be used to represent the targets. Unfortunately the second criterion has not yet been formulated precisely. It has been shown [161] that even in the $kd \to 0$ limit the polarizations are too large in the surface monolayer of dipoles in a pseudosphere, and similar errors must also occur for other target shapes. As a result the rate of energy absorption by the dipoles in the surface monolayer is too large, which leads to an error in the overall absorption cross section in proportion to the fraction $\sim N^{-1/3}$ of the total volume that is contributed by the surface monolayer. As a result, when $|m| \gg 1$ the DDA can seriously overestimate absorption cross sections, even in the dc limit $|m|kd \ll 1$. For materials with $|m| \gg 1$ other techniques appear to be superior to the DDA[165].

C

List of Publications

1. D. Baldomir, M. Pereiro, M. Iglesias, V. Pardo, **J. Botana**, J. E. Arias, K. Warda, G. Wiatrowski, and L. Wojtczak, ACTA PHYSICAE SUPERFICIERUM **7**, 95 - 103 (2004).

2. V. Pardo, P. Blaha, M. Iglesias, D. Baldomir, K. Schwarz, M. Pereiro, **J. Botana**, and J.E. Arias, JOURNAL OF MAGNETISM AND MAGNETIC MATERIALS **290–291P1**, 349 - 352 (2005).

3. M. Pereiro, **J. Botana**, D. Baldomir, K. Warda, L. Wojtczak, S. V. Mankovsky, M. Iglesias, V. Pardo, and J. E. Arias, JOURNAL OF MAGNETISM AND MAGNETIC MATERIALS **290–291P1**, 392 - 395 (2005).

4. M. Iglesias, A. Rodríguez, P. Blaha, V. Pardo, D. Baldomir, M. Pereiro, **J. Botana**, J.E. Arias, and K. Schwarz, JOURNAL OF MAGNETISM AND MAGNETIC MATERIALS **290–291P1**, 392 - 395 (2005).

5. M. Pereiro, D. Baldomir, S. V. Mankovsky, K. Warda, J. E. Arias, L. Wojtczak and **J. Botana**, JOURNAL OF PHYSICS-CONDENSED MATTER **19**, 106210-1 - 106210-14 (2007).

6. **J. Botana**, M. Pereiro, D. Baldomir, J.E. Arias, K. Warda and L. Wojtczak, JOURNAL OF MAGNETISM AND MAGNETIC MATERIALS **316**, e360-e364 (2007).

7. **J. Botana**, M. Pereiro, D. Baldomir, J. E. Arias, K. Warda and L. Wojtczak, JOURNAL OF APPLIED PHYSICS **103**, 07B716-1 - 07B716-3 (2008).

8. M. Pereiro, D. Baldomir, **J. Botana**, J. E. Arias, K. Warda, and L. Wojtczak, JOURNAL OF APPLIED PHYSICS **103**, 07A315-1 - 07A315-3 (2008).

9. **J. Botana**, M. Pereiro, D. Baldomir, H. Kobayashi, and J. E. Arias, THIN SOLID FILMS **516**, 5144-5149 (2008).

10. **J. Botana**, M. Pereiro, D. Baldomir, and J. E. Arias, THEORETICAL CHEMISTRY ACCOUNTS **122**, 297-304 (2009).

11. D. Serantes, D. Baldomir, M. Pereiro, **J. Botana**, V. M. Prida, B. Hernando, J. E. Arias, and J. Rivas, JOURNAL OF NANOSCIENCE AND NANOTECHNOLOGY **10**, 2512-2517 (2010).

12. D. Baldomir, D. Serantes, M. Pereiro, **J. Botana**, J. E. Arias, S. H. Masunaga, and J. Rivas, JOURNAL OF NANOSCIENCE AND NANOTECHNOLOGY **10**, 2717-2721 (2010).

13. M. Pereiro, **J. Botana**, D. Baldomir, D. Serantes, and J. E. Arias, JOURNAL OF NANOSCIENCE AND NANOTECHNOLOGY **10**, 2594-2599 (2010).

14. **J. Botana**, M. Pereiro, D. Baldomir, D. Serantes, and J. E. Arias, JOURNAL OF NANOSCIENCE AND NANOTECHNOLOGY **10**, 2787-2790 (2010).

15. S. Goy-López, J. Juárez, A. Cambón, **J. Botana**, M. Pereiro, D. Baldomir, P. Taboada and V. Mosquera, JOURNAL OF MATERIALS CHEMISTRY **20**, 6808-6814 (2010).

16. **J. Botana**, M. Pereiro, D. Baldomir and J. E. Arias, JOURNAL OF CHEMICAL PHYSICS **134**, 034307-1 - 34307-6 (2011).

17. A. S. Botana, P. M. Botta, C. de la Calle, A. Piñeiro, V. Pardo, **J. Botana**, M. Pereiro, D. Baldomir, J. A. Alonso, and J. E. Arias, JOURNAL OF APPLIED PHYSICS **109**, 07E114-1 - 07E114-3 (2011).

18. A. Piñeiro, A. S. Botana, V. Pardo, **J. Botana**, M. Pereiro, D. Baldomir, and J. E. Arias, JOURNAL OF APPLIED PHYSICS **109**, 07E158-1 - 07E158-3 (2011).

D

Resumo da presente Tese Doutoral

Na presente Tese Doutoral, recóllese o traballo de investigación realizado polo doutorando Jorge Botana Alcalde durante a súa etapa de posgrao. En liñas xerais, o traballo consistiu no estudo das propiedades estruturais, eléctricas e magnéticas, de distintos sistemas de baixa dimensionalidade, compostos por metais de transición. Os sistemas estudiados son de dous tipos: tricapas ultrafinas de ferro e cromo, nas que dúas capas de ferro están cubrindo unha capa central de cromo, e clusters atómicos, ben de ouro, ben dunha aleación de bismuto e manganeso. Este traballo realizouse usando técnicas ab initio, é dicir, empregando os primeiros principios. Para os nosos sistemas, iso tradúcese na resolución da ecuación de Schrdinger non relativista para un sistema formado por moitos electróns. A nosa aproximación a un problema tan complexo consiste no uso da Teoría do Funcional Densidade (TFD), que convirte o problema de moitos corpos, considerando cada electrón interactuando con todos os outros electróns, ao problema dun único corpo, no que cada electrón interactúa únicamente cun potencial efectivo creado pola densidade electrónica. A implementación desta aproximación para a solución dos sistemas que quixemos calcular realizouse principalmente co programa de TFD deMon (density of Montral).

D.1 Tricapas de $Fe_n/Cr_3/Fe_n$ (n = 1→7)

A interese polas multicapas de materiais magnéticos, como son o Fe e o Cr, débese en grande medida a dous fenómenos que se producen exclusivamente nestes sistemas. Por unha banda está o acoplamento magnético oscilatorio (AMO): para certas combinacións de metais de transición, se colocamos paralelas duas capas dun material ferromagnético separadas por unha capa espaciadora non ferromagnética, o acoplo entre ambas as capas ferromagnéticas oscila entre ferromagnético e antiferromagnético ao cambiar o ancho da capa espaciadora. Pola outra banda temos

a Magneto-Resistencia Xigante(MRX): a resistividade de multicapas como as anteriores é moito máis elevada para valores baixos dun campo magnético externo, e redúcese moito para valores altos. Este fenómeno é consecuencia de que se produce unha resistividade dependente do acoplamento entre o momento magnético das capas ferro e o espín dos electróns que transitan nelas e de que ao incrementar o campo magnético aplicado sobre a multicapa, pasa dunha configuración inicial de acoplamento antiferromagnético entre as capas ferromagnéticas a un acomplamento ferromagnético. Por isto mesmo, a MRX e o AMO están íntimamente relacionados, o cal, a súa vez produciu unha eclosión na investigación das propiedades das multicapas ferromagnéticas e a súa dependencia coa natureza e grosor da capa espaciadora. A dependencia co grosor das capas ferromagnéticas, en troques, non recibira apenas atención, e foi neste punto que a nosa investigación se enfocou.

Para atacar este problema, fixemos os nosos cálculos coa versión extendida a sistemas periódicos do deMon, o noso programa de TFD, chamada Bloch-deMon. Así calculamos a estrutura electrónica e magnética dun caso particular de multicapas, a tricapa, usando o Fe como material ferromagnético, e o antiferromagnético Cr como espaciador. O grosor cas capas de Fe varía entre 1 e 7 monocapas. Nestes cálculos atopamos que a diferencia de carga de cada un dos átomos cas capas de Fe respecto do seu estado neutro presenta unhas oscilacións tipo Friedel, como se a capa de Cr actuase como unha perturbación puntual. Asumindo a natureza tipo Friedel destas oscilacións, e extendendo o concepto de masa efectiva (que está relacionado coa mobilidade electrónica, e consecuentemente coa conductividade) á sistemas bidimensionais, obtivemos o valor da masa efectiva dos electróns nas distintas capas de Fe. Os valores observados da masa efectiva varían dende 0.5 m_e para o caso de $Fe_2/Cr_3/Fe_2$ ata 0.2 m_e para o $Fe_7/Cr_3/Fe_7$, mostrando un descenso monótono.

Por outra banda, é sabido que a MRX é un fenómeno que sucede nas interfaces das capas, e a maior parte se debe á rugosidade das interfaces (o que da lugar a interaccións entre os átomos magnéticos que están "fora de lugar" na rede e os spins dos electróns), e ao desacoplamento das estruturas de bandas entre as capas de distintos metais. Tamén existe un terceiro factor: o desacoplamento no valor da densidade de estados na enerxía de Fermi para os distintos metais na interface. Como a resistividade intrínseca dun material depende tamén do valor da enerxía de Fermi, producirase un salto de resistividade ao pasar dun metal a outro, o cal crea un termo de reflectividade puramente cuántico que se opón á propagación dos electróns, o cal incrementa a resistencia interfacial. Nos nosos cálculos atopamos que este termo é moi importante no sistema $Fe_1/Cr_3/Fe_1$ e significativo nos sistemas $Fe_3/Cr_3/Fe_3$ e $Fe_6/Cr_3/Fe_6$, sendo desprezable no resto.

D.2 Clusters de ouro moi pequenos

Entre as tendencias máis actuais na investigación en nanociencia, o desenvolvemento e estudo de estruturas cun número de átomos moi pequeno (clusters) é un

dos principais focos de atención, onde converxen distintos campos do coñecemento: a Física, a Química, a Biomedicina e a Enxeñaría; e entre os clusters máis estudados están os feitos de metais nobres (os que teñen as súas bandas d completas): Cu, Ag e Au. En concreto os clusters de Au amosan unha variedade de propiedades e comportamentos, entre os verificados experimentalmente e os preditos teóricamente: interactúan e estabilizan o ADN, teñen uns momentos magnéticos relativamente altos, son capaces de realizar unha adsorción de aminoácidos que dependa de lixeiras modificacións estruturais, desempeñan un papel de catalizador en reaccións químicas orgánicas e interactúan fortemente con moleculas que conteñen xofre. Moitas destas propiedades proveñen da tendencia dos clusters de ouro a formar estruturas 2D ou pseudo-2D (como caixas e outras estruturas ocas).

Poderíase pensar que o ouro, a prata e o cobre, sendo isoelectrónicos, poderían desempeñar papeles intercambiables en moléculas ou agregados atómicos, e isto é a miúdo unha asunción correcta, sobre todo cando se trata de reaccións químicas. Pero, mentres que está probado que as estruturas estables para os clusters de 8 átomos de prata e de cobre adoptan a forma dun octaedro con dous átomos adicionais nun dos lados, con simetría D_{2d}, os cálculos ab initio realizados ata o momento veñen demostrando que a estrutura de máis baixa enerxía para o cluster de 8 átomos de ouro ten forma de estrela de catro puntas, un cadrado con 4 átomos nos seus lados e simetría D_{4h}. Este estado fundamental é o resultado tanto de cálculos usando pseudopotenciais como métodos perturbativos.

Os clusters de ouro mantéñense conformando estruturas 2D para tamaños de ata 12 átomos: neste cluster, a estrutura de máis baixa enerxía xa é 3D. A razón para esta tardía transición 2D a 3D ten atraído a atención de moitos investigadores. Antes do traballo realizado nesta tese, a explicación máis coñecida era que sucedía debido a un moi forte solapamento entre orbitais d-d, para as estruturas 2D, que as favorecía enerxéticamente respecto das 3D. A prata e o cobre, sendo menos densos electrónicamente (por ter tamaños semellantes ao do átomo de ouro, pero moitos menos electróns), presentan un solapamente entre orbitais d-d moito máis feble, e este factor reduce moito o seu peso na reducción de enerxía das estruturas 2D.

Para atacar esta cuestión, realizamos os nosos propios cálculos en clusters 8 átomos de ouro usando o deMon, computando unha relaxación de xeometría dun gran número de configuracións iniciais. Nos nosos cálculos obtivemos, como era de agardar, que a estrutura de máis baixa enerxía era a bidimensional de simetría D_{4h}, pero a octaédrica D_{2d} era a segunda de máis baixa enerxía, por debaixo doutras estruturas 2D. Sen embargo non conservaba perfectamente a simetría dita, senon que estaba deformada, reducindo a coordinación dos átomos. A deformación é producto dunha relaxación puramente electrostática: como dixemos, os átomos de ouro teñen un tamaño semellante ao dos átomos de prata, por efectos relativistas, pese a ter moitos máis electrons; isto produce tensións adicionais nas interaccións electrostáticas núcleo-nucleo e electrón-electrón dos átomos do cluster de ouro, que

se estabilizan reducindo o índice de coordinación. Este fenómeno xa fora observado para clusters de ouro moito maiores (a redor de 20 e 50 átomos), que anque 3D, a súa estrutura tiña foma de caixa ou gaiola. No noso caso, incluso clusters 3D tan pequenos como 8 átomos sufren unha deformación que incrementa o seu volume, creando unhas pequenas "cavidades". A aparición destas cavidades (nas que o valor da función de localización electrónica (FLE) é case cero) incrementa a localización electrónica no cluster, o cal implica que a reducción enerxética polos efectos puramente cuánticos de intercambio e correlación será menos importante. Así, os clusters 2D terán un termo de correlación-intercambio que os favorecerá enerxéticamente respecto dos 3D. Os nosos resultados entran además en conflicto directo coa literatura anterior no punto referido ao solapamento dos orbitais d-d. Nós demostramos que dito solapamento é mais importante nos clusters 3D, e que é para estas estruturas que o termo cinético da enerxía se ve reducido.

Mentres que os clusters de 8 átomos de ouro non son magnéticamente activos, a súa estrutura sí que amosa unha interesante dependencia co seu momento magnético. Isto é interesante porque a literatura predí que pequenos clusters de ouro teñen unha capacidade para adsorber pequenas moléculas (incluso moléculas orgánicas importantes para a vida) moi dependente de pequenos cambios estruturais. Nós atopamos cómo é posible que se produza iso: os pequenos cambios estruturais inducidos por un pequeno cambio no momento magnético xeneran relativamente importantes transferencias de carga duns átomos a outros, o cal variará os "locus" de reacción completamente. Por outra banda, ao deberse a un cambio de momento magnético total, é moi razoable pensar que un campo magnético externo poda inducir ditos cambios, o cal nos da unha medida de control sobre a potencial capacidade de adsorción dos clusters. Además, convirte aos clusters de 8 átomos de ouro en potenciais candidatos para amosar o fenómeno de magnetostricción, de grande aplicación en diversas disciplinas.

D.3 Interacción de clusters de ouro de distinto tamaño coa molécula de osíxeno

Como dixemos, os clusters de ouro teñen aplicacións potenciais no campo da biomedicina. Pero se queremos usalos en medio orgánico, temos que verificar que sexan inertes ao igual que o son en estado bulk (excepto, obviamente, para a aplicación que busquemos), e baixo qué condicións podería variar a súa estrutura. Un cluster cunha adecuada capacidade catalítica podería volverse completamente inutil se os efectos da oxidación destrúen as súas propiedades.

A oxidación de pequenos clusters de ouro xa fora estudada con anterioridade, pero sempre enfocándose na interacción entre moléculas de osíxeno e clusters de ouro no mesmo plano. Nós fixemos cálculos usando o deMon para comprobar se hai estados ligados ouro-osíxeno fora de plano que sexan estables. Outro punto

de interese foi averiguar se a estrutura dos clusters de ouro se distorsionan pola interacción coas moléculas de osíxeno.

O que atopamos foi que a interacción entre as moléculas de osíxeno e pequenos clusters bidimensionais de ouro depende de se o número de átomos do cluster é par ou impar. Para os clusters con número par de átomos, a molécula de osíxeno forma un enlace co cluster no seu propio plano, mentres que para os clusters con número impar de átomos, o "enlace" prodúcese fora do plano do cluster. Esta interacción fora do plano, non produce un enlace químico real, un estado ligado, senon un estado feblemente ligado debido a unha suma de interaccións magnetostáticas e electrostáticas, que produce unha grande estabilidade, en todo caso. Este enlace feble tamén produce que a estrutura orixinal se deforme, dotándoa dunha certa curvatura. En conclusión, os pequenos clusters de ouro con número par de átomos verán cambiadas as súas propiedades electrónicas debido ao enlace químico coa molécula de osíxeno, mentres que os clusters con un número impar de átomos conservarán a súa configuración electrónica, pero as súas potenciais propiedades catalíticas ou adsorbantes poden verse afectadas pola torsión.

D.4 Desacordo entre teoría e experimento: clusters de bismuto-manganeso

Os clusters puros posúen, por natureza da escala de tamaño, propiedades moi interesantes e distintas da materia en estado contínuo, incluíndo excepcionalmente grandes momentos magnéticos. Este efecto pode ser potenciado cando se engaden impurezas. Unha pregunta que era preciso respostar era se este efecto das impurezas se incrementaría ou degradaría cando a proporción de impurezas fose tan grande como para non poder considerar o cluster como unha suma de metal puro mais impurezas, senon como unha aleación de dous ou máis metais. Dende que se plantexou esta pregunta, lévanse estudado teoricamente moitas nanoaleacións de metais de transición ferromagnéticos con non magnéticos, que resultan ter un magnetismo potenciado. Nun artigo de Yin et al. sobre as súas medidas cun dispositivo Stern-Gerlach, atopouse que o momento magnético de nanoaleacións de bismuto e manganeso era excepcionalmente alto para unha proporción de bismuto a manganeso de 2, o cal o diferenciaba doutras nanoaleacións de bismuto. Nun artigo posterior, Chen et al. realizaron cálculos TFD estensivos sobre ditas nanoaleacións de bismuto e manganeso, segundo a fórmula Bi_nMn_m con n=1-6 e m=1-12. Mentres que o acordo destes resultados teóricos estaba en xeral en bo acordo co experimento, había algúns casos nos que a disparidade entre ambos era moi grande. O caso máis significativo era o do Bi_4Mn, onde os cálculos DFT prediciron un momento magnético total de 5 magnetóns de Bohr (μ_B), mentrea que as medidas experimentais atoparon que dito cluster tiña un momento total de 1.6 μ_B (que o momento magnético non sexa enteiro implica que a mostra experimental non

é isoméricamente pura: a maioría dos clusters terán un momento magnético de 1 μ_B, mentres que haberá unha minoría con momentos magnéticos maiores, de 3 μ_B, 5 μ_B, 7 μ_B, etc). A causa desta discrepancia permaneceu descoñecida a pesar dos esforzos realizados para solventala.

Para tentar resolvela, realizamos unha estensiva optimización de xeometría de centos de configuracións iniciais converxidas en xeometría usando modelos rápidos de tight-binding para chegar a 21 xeometrías. Estas 21 estruturas foron despois relaxadas completamente usando o deMon, e tamén se usaron para facer cálculos de clusters ionizados, en caso de que o medido polo dispositivo Stern-Gerlach fose un cluster ionizado. Adicionalmente, usouse outro código TFD, chamado OCTOPUS, que admite o uso de spinores, o cal permite facer relaxacións do estado magnético do cluster cos momentos magnéticos de cada electrón aliñándose libremente en calquera dirección do espacio (magnetismo non colinear), e tamén permite o cálculo da contribución orbital ao momento magnético.

E sen embargo, tras todos estes cálculos, non conseguimos atopar ningún estado fundamental que pudese explicar satisfactoriamente o baixo momento magnético experimental. Tampouco os cálculos non colineares deron resultado, e o cálculo da contribución orbital total ao momento magnético proporcionaba un valor desprezable fronte ao momento magnético total dos clusters. Sentindo que examinaramos exhaustivamente todos os escenarios posibles, ao revisar os datos observamos que había 3 isómeros entre os 21 máis estables que tiñan un momento magnético total de 1 μ_B, polo que serían bos candidatos para formar esa maioría da mostra experimental, pero desafortunadamente, a enerxía destas estruturas era demasiado alta respecto do estado fundamental. Non só iso, había outros 18 isómeros con enerxías mais baixas ca estes 3, así que era altamente improbable que pudesen formar unha fracción significativa sequera da mostra experimental.

¿Existía algún xeito de que estas 3 estruturas de baixo momento magnético pudesen ver favorecida a súa producción no dispositivo experimental? Examinando as estruturas obtidas no resto da serie Bi_nMn_m, chamounos poderosamente a atención que os 3 isómeros de baixo momento magnético tiñan unha xeometría moi semellante á do estado fundamental do Bi_3Mn (un tetrahedro), e poderíanse obter simplemente engadindo un átomo de bismuto adicional ao vértice de manganeso. Se durante a producción de clusters no dispositivo experimental os clusters de Bi_3Mn se formasen moito máis rápido que os Bi_4Mn, logo non sería irrazoable pensar que os de Bi_4Mn se formasen a partir dos de Bi_3Mn. Facendo un cálculo do Bi_3Mn atopamos que ten un momento dipolar de 2.4 D na dirección que conecta o átomo de manganeso co centro do triángulo que forman os tres bismutos, privilexiando ese eixo. Un momento dipolar tan alto faino especialmente estable (polo cal é probable que se formen máis rápido que os Bi_4Mn), e favorecería a incorporación do cuarto átomo de bismuto ao longo dese eixo, en vez de destruir inmediatamente a estrutura tetraédrica para formar un isómero que sería máis estable. Se a vida media de algún destes 3 isómeros de baixo momento magnético, antes de decaer á

estrutura de máis baixa enerxía, é suficientemente longo para perdurar durante o voo dentro do aparello de Stern-Gerlach, sí que podería suceder que formasen unha parte significativa da mostra experimental.

D.5 Caracterización de mostras de nanopartículas de ouro

Os clusters compostos por un número moito maior de átomos denomínanse nanopartículas (NPs), e xa non presentan únicamente as cualidades propias dos clusters. Cando o número de átomos dun cluster metálico empeza a contarse por milleiros en vez de por decenas, as propiedades que ten o metal en medio contínuo empezan a manifestarse, mesturadas coas que son propiamente de clusters: É o dominio da mesoescala.

Esta mestura de propiedades, xunto coa posibilidade de manufacturar os tamaños e formas que se desexen, veñen facendo especialmente atractivas as NPs, para campos diversos como os da catálise, fotónica, electrónica, detección, bioetiquetado e producción de imaxes. Por examplo, o número, localización e intensidade das bandas de plasmón de superficie en nanocristais de ouro e prata amosa unha forte correlación co seu tamaño e forma, o fai que estas NPs sexan un axente terapéutico para a absorción do plasmón de superficie na rexión espectral do infravermello cercano, ou que sexan biosensores cando a absorción acontece na rexión visible. Por outra banda, sábese que a presenza de cuñas e puntas nunha estrutura produce unha potenciación dos campos eléctricos, o que é importante para a súa actividade como sensores, e que os planos cristalográficos poden controlarse para que amosen unha reactividade selectiva, tendo en conta que a morfoloxía da NP, en último caso, determinará como se poden ensamblar.

Por isto, a importancia do control do tamaño e forma na producción de NPs é un punto tecnolóxicamente crucial. Un grupo de física experimental de compañeiros da USC ven investigando distintos métodos para este fin. Pero, unha vez producida a mostra experimental, é preciso caracterizala con precisión. Isto pode facerse mediante unha análise estadística de imaxes tomadas mediante microscopía electrónica, sen embargo pode resultar unha labor longa e difícil. Un método máis directo sería realizar unha análise espectral da mostra experimental e logo comparala coas prediccióǹs teóricas do espectro para distintas composicións en tamaño e forma da mostra. Isto precisamente foi ao que nos dedicamos no último traballo para a presente tese.

Polo seu grande tamaño, é completamente impráctico calcular o espectro destas NPs de ouro mediante TFD ou calquera outra técnica ab initio. Xa que logo foi preciso cambiar a nosa estratexia para este caso, e usar unha modelización denominada Aproximación de Dipolos Discretos (ADD), que consiste en substituír a nanopartícula por unha rede cúbica de dipolos puntuais, cuias propiedades dependen da función dieléctrica relativa entre o metal da NP e o medio. Deste xeito,

usando a ADD fomos capaces de obter un cálculo ben aproximado do espectro de extinción teórico de mostras de bipirámides e nanoplacas triangulares, e os nosos resultados coincidiron en boa medida coas poboacións observadas por microscopía electrónica.

Bibliography

[1] R. G. Parr and W. Yang, *Density-Functional Theory of Atoms and Molecules* (Oxford University Press, New York, 1989).

[2] D. R. Hartree, Proc. Cambridge Philos. Soc. **24**, 89 (1928).

[3] J. C. Slater, Phys. Rev. **35**, 210 (1930).

[4] V. Fock, Z. Phys. **61**, 126 (1930).

[5] C. D. Sherrill and H. F. Schaeffer, Adv. Quantum Chem. **34**, 143 (1999).

[6] L. H. Thomas, Proc. Camb. Phil. Soc **23**, 542 (1926).

[7] P. Hohenberg and W. Kohn, Phys. Rev. **136**, B864 (1964).

[8] W. Kohn and L. J. Sham, Phys. Rev. **140**, A1133 (1965).

[9] J. P. Perdew, J. Tao, and S. Kümmel, *Recent Advances in Electron Correlation Methodology* (ACS Books, Washington, DC, 2004).

[10] J. P. Perdew, K. Burke, and M. Ernzerhof, Phys. Rev. Lett. **77**, 3865 (1996).

[11] J. P. Perdew, Y. Wang, and E. Engel, Phys. Rev. Lett. **66**, 508 (1991).

[12] J. P. Perdew, J. A. Chevary, S. H. Vosko, K. A. Jackson, M. R. Pederson, D. J. Singh, and C. Fiolhais, Phys. Rev. B **48**, 4978 (1993).

[13] J. P. Perdew, Phys. Rev. B **34**, 7406E (1986).

[14] J. Tao, J. P. Perdew, V. N. Staroverov, and G. E. Scuseria, Phys. Rev. Lett. **91**, 146401 (2003).

[15] A. D. Becke, J. Chem. Phys. **98**, 1372 (1993).

[16] J. P. Perdew, M. Ernzerhof, and K. Burke, J. Chem. Phys. **105**, 9982 (1996).

[17] A. St.-Amant and D. R. Salahub, Chem. Phys. Lett. **169**, 387 (1990).

[18] J. C. Slater, Adv. Quantum Chem. **6**, 1 (1972).

[19] H. Sambe and R. H. Felton, J. Chem. Phys. **62**, 1122 (1975).

[20] B. I. Dunlap, J. W. D. Connolly, and J. Sabin, J. Chem. Phys. **71**, 3396 (1979).

[21] S. H. Vosko, L. Wilk, and M. Nusair, Can. J. Phys. **58**, 1200 (1980).

[22] A. D. Becke and K. E. Edgecombe, J. Chem. Phys. **92**, 5397 (1990).

[23] J. P. Perdew, Phys. Rev. B **33**, 8822 (1986).

[24] H. B. Schlegel, *Modern electronic structure theory.* (Word Scientific, Singapore, 1995), chap. 8, p. 459.

[25] C. C. J. Roothaan, Rev. Mod. Phys. **32**, 179 (1960).

[26] M. Pereiro, *PhD Thesis* (Universidade de Santiago de Compostela, 2010).

[27] S. Huzinaga, J. Andzelm, M. Klobukowski, E. Radzio-Andzelm, Y. Sakai, and H. Tatewaki, *Gaussian Basis Sets for Molecular Calculations* (Elsevier, Amsterdam, 1984).

[28] N. Godbout, D. R. Salahub, J. Andzelm, and E. Wimmer, Can. J. Chem **70**, 560 (1992).

[29] A. M. Köster, P. Calaminici, S. Escalante, R. Flores-Moreno, A. Goursot, S. Patchkovski, J. U. Reveles, D. R. Salahub, A. Vela, and T. Heine, *The deMon User's Guide, Version 1.0.3* (2003-2004).

[30] R. W. Erwin, J. Borchers, M. B. Salamon, S. Sinha, J. J. Rhyne, J. E. Cunningham, and C. P. Flynn, Phys. Rev. Lett. **56**, 259 (1986).

[31] J. Grünberg, R. Schreiber, Y. Pang, M. B. Brodsky, and H. Sowers, Phys. Rev. Lett. **57**, 2442 (1986).

[32] H. Sato, P. A. Schroeder, J. M. Slaughter, W. P. P. Jr., and W. A. Razzaq, Superlattice Microst. **4**, 45 (1987).

[33] M. N. Baibich, J. M. Broto, A. Fert, F. N. V. Dau, F. Petroff, P. Etienne, G. Creuzet, A. Friederich, and J. Chazelas, Phys. Rev. Lett. **61**, 2472 (1988).

[34] S. S. P. Parkin, *Ultrathin Magnetic Structures* (Springer-Verlag, Berlin-Heidelberg-New York, 1994), vol. II, p. 148.

[35] C. F. Majkrzak, J. W. Cable, J. Kwo, M. Hong, D. B. McWhan, Y. Yafet, J. V. Waszczak, and C. Vettier, Phys. Rev. Lett. **56**, 2700 (1986).

[36] S. S. P. Parkin, N. More, and K. P. Roche, Phys. Rev. Lett. **64**, 2304 (1990).

[37] M. Büttner, *PhD Thesis* (Universität Basel, 2006).

[38] M. Pereiro and D. Baldomir, Phys. Rev. A **72**, 45201 (2005).

[39] P. Bruno and C. Chappert, Phys. Rev. Lett. **67**, 1602 (1991).

[40] P. Bruno, Phys. Rev. B **52**, 411 (1995).

[41] P. J. H. Bloemen, M. T. Johnson, M. T. H. van de Vorst, R. Coehoorn, J. J. de Vries, R. Jungblut, J. aan de Stegge, A. Reinders, and W. J. M. de Jonge, Phys. Rev. Lett. **72**, 764 (1994).

[42] D. Baldomir, M. Pereiro, M. Iglesias, L. Wojtczak, and P. Młinarsky, Prog. Surf. Sci. **59**, 187 (1998).

[43] K. Warda, L. Wojtczak, D. Baldomir, and M. Pereiro, Surf. Rev. Lett. **8**, 271 (2001).

[44] S. N. Okuno and K. Inomata, Phys. Rev. Lett. **72**, 1553 (1994).

[45] H. Kobayashi, A. St-Amant, D. R. Salahub, and T. Ito, Proc. 10th Int. Congr. Catal. p. 2527 (1993).

[46] H. C. Herper, L. Szunyogh, P. Entel, and P. Weinberger, Phys. Rev. B **68**, 134421 (2003).

[47] M. Pereiro, D. Baldomir, S. V. Man'kovsky, K. Warda, J. E. Arias, L. Wojtczak, and J. Botana, J. Phys.: Condens. Matter. **19**, 106210 (2007).

[48] D. A. Papaconstantopoulos, *Handbook of the Band Structure of Elemental Solids* (Plenum Press, London, 1986), pp. 87–102.

[49] H. H. Wang and G. Y. Guo, J. Magn. Magn. Mater. **209**, 98 (2000).

[50] E. Fawcett, Rev. Mod. Phys. **60**, 209 (1998).

[51] A. M. N. Niklasson, B. Johansson, and J. Nordström, Phys. Rev. Lett. **82**, 4544 (1999).

[52] H. Zabel, J. Phys.:Condens. Mat. **11**, 9303 (1999).

[53] S. Mirbt, A. M. N. Niklasson, B. Johansson, and H. L. Skriver, Phys. Rev. B **54**, 6382 (1996).

[54] H. Hasegawa, Phys. Rev. B **42**, 2368 (1990).

[55] R. S. Fishman, J. Phys.:Condens. Mat. **13**, R235 (2001).

[56] K. Hirai, J. Magn. Magn. Mater. **240**, 238 (2002).

[57] K. Hirai, Phys. Rev. B **59**, R6612 (1999).

[58] H. C. Herper, P. Entel, L. Szunyogh, and P. Weinberger, Phase Trans. **77**, 191 (2004).

[59] A. B. Klautau, S. B. Legoas, R. B. Muniz, and S. Frota-Pessôa, Phys. Rev. B **60**, 3421 (1999).

[60] D. Stoeffler and F. Gautier, Phys. Rev. B **44**, 10389 (1991).

[61] M. Pereiro, D. Baldomir, S. Man'kovsky, and J. E. Arias, Int. J. Quantum Chem. **91**, 245 (2003).

[62] J. Friedel, Philos. Mag. **43**, 153 (1952).

[63] A. H. Ammar, Phys. B **225**, 132 (1996).

[64] P. D. Johnson, K. Garrison, Q. Dong, N. V. Smith, D. Li, J. Mattson, J. Pearson, and S. D. Bader, Phys. Rev. B **50**, R8954 (1994).

[65] S. Sanvito, C. J. Lambert, J. H. Jefferson, and A. M. Bratkovsky, J. Phys.:Condens. Mat. **10**, L691 (1998).

[66] P. Grunberg, D. E. Burgler, R. G. D. Olligs, M. Buchmeier, M. Breidbach, B. Kuanr, and R. Schreiber, J. Phys. D **35**, 2403 (2002).

[67] M. Pereiro, D. Baldomir, S. Man'kovsky, and J. E. Arias, J. Magn. Magn. Mater. **290-291**, 392 (2005).

[68] M. J. Hall, D. B. Jardine, J. E. Evetts, J. A. Leake, and R. E. Somekh, J. Magn. Magn. Mater. **173**, 253 (1997).

[69] R. Q. Hood, L. M. Falicov, and D. R. Penn, Phys. Rev. B **49**, 368 (1994).

[70] P. J. Mohan, A. Datta, S. S. Mallajosyula, and S. K. Pati, J. Phys. Chem. B **110**, 18661 (2006).

[71] S.-Y. Wang, J.-Z. Yu, H. Mizuseki, Q. Sun, C.-Y. Wang, and Y. Kawazoe, Phys. Rev. B **70**, 165413 (2004).

[72] P. de la Presa, T. Rueda, M. del Puerto Morales, F. J. Chichón, R. Arranz, J. M. Valpuesta, and A. Hernando, J. Phys. Chem. B **113**, 3051 (2006).

[73] X. López-Lozano, L. A. Pérez, and I. L. Garzón, Phys. Rev. Lett. **97**, 233401 (2006).

[74] U. Heiz and E. L. Bullock, J. Mater. Chem. **14**, 564 (2004).

[75] M. Haruta, J. New Mat. Electrochem. Syst. **7**, 163 (2004).

[76] S. P. Nolan, Nature **445**, 496 (2007).

[77] C. Majumder, T. Briere, H. Mizuseki, and Y. Kawazoe, J. Chem. Phys. **117**, 7669 (2002).

[78] C. Majumder and S. K. Kulshreshtha, Phys. Rev. B **73**, 155427 (2006).

[79] E. M. Fernández, J. M. Soler, I. L. Garzón, and L. C. Balbás, Phys. Rev. B **70**, 165403 (2004).

[80] H. Grönbeck and P. Broqvist, Phys. Rev. B **71**, 073408 (2005).

[81] F. Furche, R. Ahlrichs, P. W. C. Jacob, S. Gilb, T. Bierweiler, and M. M. Kappes, J. Chem. Phys. **117**, 6982 (2002).

[82] H. Häkkinen and U. Landman, Phys. Rev. B **62**, R2287 (2000).

[83] W. Fa, C. Luo, and J. Dong, Phys. Rev. B **72**, 205428 (2005).

[84] R. M. Olson and M. S. Gordon, J. Chem. Phys. **126**, 214310 (2007).

[85] G. Bravo-Pérez, I. L. Garzón, and O. Novaro, J. Mol. Struc.-Theochem **493**, 225 (1999).

[86] H. Häkkinen, M. Moseler, and U. Landman, Phys. Rev. Lett. **89**, 033401 (2002).

[87] J. Zhao and J. Yang, Phys. Rev. B **67**, 085404 (2003).

[88] M. Pereiro, D. Baldomir, and J. E. Arias, Phys. Rev. A **75**, 063204 (2007).

[89] K. Yabana and G. F. Bertsch, Phys. Rev. A **60**, 3809 (1999).

[90] M. Diefenbach and K. S. Kim, J. Phys. Chem. B **110**, 21639 (2006).

[91] S. Bulusu and X. C. Zeng, J. Chem. Phys. **125**, 154303 (2006).

[92] X. Xing, B. Yoon, U. Landman, and J. H. Parks, Phys. Rev. B **74**, 165423 (2006).

[93] D. Tian, J. Zhao, B. Wang, and R. B. King, J. Phys. Chem. A **111**, 411 (2007).

[94] P. Pyykkö, Chem. Rev. **88**, 563 (1988).

[95] D. J. Wales and J. P. K. Doye, J. Phys. Chem. A **101**, 5111 (1997).

[96] H. W. Ghebriel and A. Kshirsaga, J. Chem. Phys. **126**, 244705 (2007).

[97] M. Okumura, Y. Kitagawa, M. Haruta, and K. Yamaguchi, Chem. Phys. Lett. **346**, 163 (2001).

[98] G. Mills, M. S. Gordon, and H. Metiu, J. Chem. Phys. **118**, 4198 (2003).

[99] Q. Sun, P. Jena, Y. D. Kim, M. Fischer, and G. Gantefr, J. Chem. Phys. **120**, 6510 (2004).

[100] L. M. Molina and B. Hammer, J. Chem. Phys. **123**, 161104 (2005).

[101] J. Wang, G. Wang, and J. Zhao, Chem. Phys. Lett. **380**, 716 (2003).

[102] I. M. L. Billas, A. Châtelain, and W. A. de Heer, Science **265**, 1682 (1994).

[103] J. A. Alonso, Chem. Rev. **100**, 637 (2000).

[104] D. Zitoun, M. Respaud, M.-C. Fromen, M. J. Casanove, P. Lecante, C. Amiens, and B. Chaudret, Phys. Rev. Lett. **89**, 037203 (2002).

[105] E. O. Berlanga-Ramrez, F. Aguilera-Granja, J. M. Montejano-Carrizales, A. Daz-Ortiz, K. Michaelian, and A. Vega, Phys. Rev. B **70**, 014410 (2004).

[106] H. Y. Kim, J. H. R. H. G. Kim, and H. M. Lee, Phys. Rev. B **75**, 212105 (2007).

[107] T. Sondón, J. Guevara, and A. Saúl, Phys. Rev. B **75**, 104426 (2007).

[108] M. Pereiro, D. Baldomir, and J. E. Arias, Phys. Rev. B **80**, 075412 (2009).

[109] T. Hihara, S. Pokrant, and J. A. Becker, Chem. Phys. Lett. **294**, 357 (1998).

[110] S. Pokrant and J. Becker, J. Magn. Magn. Mater. **226-230**, 1921 (2001).

[111] S. Yin, R. Moro, X. Xu, and W. A. de Heer, Phys. Rev. Lett. **98**, 113401 (2007).

[112] S. Yin, X. Xu, R. Moro, and W. A. de Heer, Phys. Rev. B **72**, 174410 (2005).

[113] H. Chen, H. K. Yuan, A. L. Kuang, Y. Miao, P. Chen, and Z. H. Xiong, Phys. Rev. B **77**, 184429 (2008).

[114] R. Flores-Moreno, www.theochem.uni-stuttgart.de/pseudopotentials p. 20.02.03 (2003).

[115] H. Zhang and K. Balasubramanian, J. Chem. Phys. **97**, 3437 (1997).

[116] A. M. Koester, R. Flores-Moreno, G. Geudtner, A. Goursot, T. Heine, J. U. Reveles, A. Vela, and D. R. Salahub, deMon 2003 code (NRC, Canada, 2003) creation (29 - 03 - 96, Andreas M. Koester and Matthias Krack) (2003).

[117] C. Hartwigsen, S. Goedecker, and J. Hutter, Phys. Rev. B **58**, 3641 (1998).

[118] M. A. L. Marques, A. Castro, G. F. Bertsch, and A. Rubio, Comp. Phys. Comm. **151**, 60 (2003).

[119] P. A. M. Dirac, Math. Proc. Cambr. Phil. Soc. **26**, 376 (1930).

[120] J. P. Perdew and A. Zunger, Phys. Rev. B **23**, 5048 (1981).

[121] J. P. Perdew and Y. Wang, Phys. Rev. B **45**, 13244 (1992).

[122] A. D. Becke, Phys. Rev. A **38**, 3098 (1988).

[123] C. Lee, W. Yang, and R. G. Parr, Phys. Rev. B **37**, 785 (1988).

[124] J. P. Perdew and Y. Wang, Phys. Rev. B **33**, 8800 (1986).

[125] B. Zimmermann, *Ph.D. Thesis* (Universitat Hannover, 1999).

[126] R. Moro, S. Yin, X. Xu, and W. A. de Heer, Phys. Rev. Lett. **93**, 086803 (2004).

[127] R. Coehoorn and R. A. de Groot, J. Phys. F Met. Phys. **15**, 2135 (1985).

[128] Y. Xia, Y. Xiong, B. Lim, and S. E. Skrabalak, Angew. Chem. Int. Ed. **48**, 60 (2009).

[129] E. Boisselier and D. Astruc, Chem. Soc. Rev. **38**, 1759 (2009).

[130] M. Grzelczak, J. Pérez-Juste, P. Mulvaney, and L. M. Liz-Marzán, Chem. Soc. Rev. **37**, 1783 (2008).

[131] M. Hu, J. Chen, Z.-Y. Li, L. Au, G. V. Hartland, X. Li, M. Marquez, and Y. Xia, Chem. Soc. Rev. **35**, 1084 (2006).

[132] B. Sepúlveda, P. C. Angelomé, L. M. Lechuga, and L. M. Liz-Marzán, Nano Today **4**, 244 (2009).

[133] K. L. Kelly, E. Coronado, L. L. Zhao, and G. C. Schatz, J. Phys. Chem. B **107**, 668 (2003).

[134] N. Tian, Z.-Y. Zhou, S.-G. Sun, Y. Ding, and Z. L. Wang, Science **316**, 732 (2007).

[135] J.-U. Kim, S.-H. Cha, K. Shin, J. Y. Jho, and J.-C. Lee, Adv. Mater. **16**, 459 (2004).

[136] J. Zhang, Y. Gao, R. A. Alvarez-Puebla, J. M. Buriak, and H. Fenniri, Adv. Mater. **18**, 3233 (2006).

[137] T. K. Sau and C. J. Murphy, J. Am. Chem. Soc. **126**, 8648 (2004).

[138] S. S. Shankar, A. Rai, B. Ankamwar, A. Singh, A. Ahmad, and M. Sastry, Nature Mater. **3**, 482 (2004).

[139] J. Zhang, H. Liu, Z. Wang, and N. Ming, Adv. Funct. Mater. **17**, 3295 (2007).

[140] J. Chen, F. Saeki, B. J. Wiley, H. Cang, M. J. Cobb, Z.-Y. Li, L. Au, H. Zhang, M. B. Kimmey, X. Li, et al., Nano Lett. **5**, 473 (2005).

[141] C. G. Khoury and T. Vo-Dinh, J. Phys. Chem. C **112**, 18849 (2008).

[142] F. Kim, S. Connor, H. Song, T. Kuykendall, and P. Yang, Angew. Chem. Int. Ed. **43**, 3673 (2004).

[143] A. Sánchez-Iglesias, I. Pastoriza-Santos, J. Pérez-Juste, B. Rodríguez-González, F. J. G. de Abajo, and L. M. Liz-Marzán, Adv. Mater. **18**, 2529 (2006).

[144] J. Xu, S. Li, J. Weng, X. Wang, Z. Zhou, K. Yang, M. Liu, X. Chen, Q. Cui, M. Cao, et al., Adv. Funct. Mater. **18**, 2529 (2006).

[145] X. Kou, W. Ni, C.-K. Tsung, K. Chan, H.-Q. Lin, G. D. Stucky, and J. Wang, Small **3**, 2103 (2007).

[146] S. Goy-López, J. Juárez, A. Cambón, J. Botana, M. Pereiro, D. Baldomir, V. Mosquera, and P. Taboada, J. Mater. Chem. **20**, 6808 (2010).

[147] B. T. Draine and P. J. Flatau, J. Opt. Soc. Am. A **11**, 1491 (1994).

[148] B. T. Draine and P. J. Flatau, arXiv:0809.0337v4 [astro-ph] (2008).

[149] P. G. Etchegoin, E. C. L. Ru, and M. Meyer, J. Chem. Phys. **125**, 164705 (2006).

[150] R. R. Dagastine, D. C. Prieve, and L. R. White, J. Colloid Interf. Sci. **231**, 351 (2000).

[151] R. Gulich, M. Köhler, P. Lunkenheimer, and A. Loidl, Radiat. Environ. Bioph. **48**, 107 (2009).

[152] K. Nörtemann, J. Hilland, and U. Kaatze, J. Phys. Chem. A **101**, 6864 (1997).

[153] E. Carbó-Argibay, B. Rodríguez-González, J. Pacifico, I. Pastoriza-Santos, J. Pérez-Juste, and L. M. Liz-Marzán, Angew. Chem. Int. Ed. **46**, 8983 (2007).

[154] M. Kohout and A. Savin, Int. J. Quantum Chem. **60**, 875 (1996).

[155] M. Levy and J. P. Perdew, Phys. Rev. A **32**, 2010 (1985).

[156] P. Fuentealba, J. Phys. B: At. Mol. Opt. Phys. **30**, 2039 (1997).

[157] P. Fuentealba, Int. J. Quantum Chem. **69**, 559 (1998).

[158] H. DeVoe, J. Chem. Phys. **41**, 393 (1964).

[159] H. DeVoe, J. Chem. Phys. **43**, 3199 (1965).

[160] E. M. Purcell and C. R. Pennypacker, Astrophys. J. **186**, 705 (1973).

[161] B. T. Draine, Astrophys. J. **333**, 848 (1988).

[162] B. T. Draine and J. J. Goodman, Astrophys. J. **405**, 685 (1993).

[163] B. T. Draine, *The discrete dipole approximation for light scattering by irregular targets.* (Academic Press, New York, 2000), p. 131.

[164] J. J. Goodman, B. T. Draine, and P. J. Flatau, Opt. Lett. **16**, 1198 (1990).

[165] F. Rouleau and P. G. Martin, Astrophys. J. **414**, 803 (1993).